Magnons in ultrathin Fe/Co multi-layers on W(110) and Ir(111).

Zur Erlangung des akademischen Grades eines
DOKTORS DER NATURWISSENSCHAFTEN (Dr. rer. nat.)

von der KIT-Fakultät für Physik des
Karlsruher Instituts für Technologie (KIT)
genehmigte

DISSERTATION

von

M.Sc. Sergey Tsurkan
aus
Kiew, Ukraine

Tag der mündlichen Prüfung: 18. Dezember 2020

Referent: PD Dr. Khalil Zakeri Lori

Korreferent: Prof. Dr. Wulf Wulfhekel

Department of Physics
Karlsruhe Institute of Technology

Dissertation

in Physics

submitted by

Sergey Vasilyevich Tsurkan

born in Ukraine

December 2020

Magnons in ultrathin Fe/Co multi-layers on W(110) and Ir(111).

This Dissertation has been carried out by Sergey V.Tsurkan
at the
Karlsruhe Institute of Technology
under the supervision of
PD Dr. Khalil Zakeri Lori

Abstract

Probing the fundamental magnetic interactions in layered magnetic structures is essential to the understanding of the properties of these systems. Such physical quantities can be experimentally measured by probing the magnon dispersion relation over the whole Brillouin zone. On this regard, high wavevector magnons in ultrathin Fe and Co multilayers grown on W(110) and Ir(111) are studied using spin polarized high resolution electron energy loss spectroscopy.

In layers of Fe and Co films deposited on W(110) the magnons are probed along the [001] direction in the wavevector range of 0.25 Å$-$1.3 Å^{-1}. Experimental results reveal two magnon modes which exhibit a clear dispersion as expected. The results are described within the Heisenberg model. In the case of 1ML Co/1ML Fe/W(110) structure, the interface Fe intralayer exchange coupling constants are found to be enhanced when compared to 1ML Fe/W(110). The interlayer exchange coupling was found to be weak (4.5 meV) relative to the 2ML Fe deposited on the same substrate (7.6 meV). The antisymmteric Dzyaloshinskii-Moriya interaction (DMI) was observed to be enhanced when compared to the 2ML Fe/W(110) system.

Fe films with the thickness of 2ML and 3ML showed very soft magnons when they were grown on Ir(111). This indicates rather small exchange coupling constants in these systems. For the case of 2ML Co/1ML Fe/Ir(111) two magnon modes were observed. Comparing the experimental results with those of *ab initio* calculations it is observed that the exchange interaction in the Fe layer at the interface is very weak, with a large antiferromagnetic contribution.

The results provide a deeper understanding of the magnetic interactions in layered structures and may help to advance the understanding of the role of symmetric and antisymmetric exchange interaction in low dimensional magnetism.

Contents

"Start by doing what's necessary; then do what's possible; and suddenly you are doing the impossible."
- Francis of Assisi

1. Introduction

Magnetism has been undertaken as a study for a few thousand years. The Greek scholars discussed an iron ore called lodestone which eventually resulted in the development of navigational magnetic compasses. Only around the 13th century the first mention of the magnetic compass was recorded, and in the last two centuries we have seen a rapid progress in the subject [6, 99]. Today magnetism is still an important topic, being at the heart of condensed matter research. Magnetism is a purely quantum mechanical effect as the Bohr-van Leeuwen theorem states, where in the classical description at any finite temperature there should not be any net magnetization observed.

A magnetic solid may be imagined as a latice of spins. The elementary collective magnetic excitations in a such a system are called spin waves and the associated quasiparticles are called magnons. In order to explain magnetic ordering at a finite temperature and the emergence of the critical temperature, T_C called the Curie temperature, to a paramagnetic transition, magnons are of great importance. In the vast range of temperatures, primarily two types of interactions are responsible for magnetic order: dipole and the exchange interaction. While the dipolar interaction may be able to explain some magnetic ordering at temperatures below 1 K, many ferromagnets have their ordering taking place at far higher temperatures such as bulk Fe at 1043 K and therefore cannot explain long range order in these materials. The exchange interaction on the other hand is able to explain long range order at such high temperatures [6]. Investigating these phenomena is essential to have an understanding of magnetic interactions. In that context high wave vector magnons are ideal to investigate the exchange interaction since the length scales of both are on the order of up to a few angstroms. Also, reducing the dimensionality of magnets can produce many exotic states [109]. Investigation of magnetic properties of thin films holds a fundamental importance for the understanding of magnetism and can lead to important technological advancements (e.g. hard disk drive).

A magnetic solid has competing magnetic interactions that will define it's ground state. In particular, there is the symmetric exchange interaction and antisymmetric Dzyaloshinskii-Moriya interaction among others. If the symmetric exchange interaction is dominant, then the system will exhibit either ferromagnetic or antiferromagnetic behavior. This interaction is a consequence of the Coulomb interaction between electrons and the Pauli exclusion principle and is a purely quantum mechanical effect having no classical analogue. In the case where the antisymmetric Dzyaloshinskii-Moriya interaction becomes comparable to the symmetric term and larger than the magnetic anisotoropy , the result is a tendency to have a non-collinear ground state. Here the origin is in the spin-orbit coupling and the absence of inversion symmetry [6, 109]. As a results of these competing interactions, there can arise many exotic states in a magnetic system [35, 42, 86, 104]. Therefore it is important to quantify these magnetic interactions in order to understand properties of

various magnetic systems.
Various experimental techniques can be employed in order to study magnetic interactions in ferromagnetic materials. In inelastic neutron scattering (INS) neutrons are scattered from a bulk material to study the magnetic properties of materials (magnons). However, this technique is very limited when it comes to thin films because neutrons have a large penetration depth into the material and a relatively weak interaction with matter. This makes this technique not sensitive to surfaces. Ferromagnetic resonance (FMR) and Brillouin light scattering (BLS) experiments have been employed to investigate thin films, however studies are done in the limit of small wavevectors. High wavevector magnons on the other hand are governed by the exchange interaction with lifetimes on the order of femtoseconds and interatomic lenghtscales [6, 85]. Therefore, SPEELS has been employed in order to probe high wavevector magnons [109, 110].
Well modeled and interesting systems to study magnetic interactions are ultrathin films. They provides a well defined, high purity system due to the epitaxial thin film growth and nearly a perfect crystal structure in the low coverage regime. Of particular interest is the interface of the ultrathin films and the substrates that they are grown on. The spin polarized high resolution electron energy loss spectroscopy (SPHREELS or SPEELS) technique is a very powerful tool that can probe these interfaces and investigate magnetic interactions in thin films due to its high sensitivity and the ability to probe the magnons up to the surface Brilluoin zone (SBZ) boundary. This technique can also be used to investigate non magnetic excitations such as phonons and plasmons. Experimental results in ferromagnetic thin films would give information on the symmetric Heisenberg exchange, antisymmetric Dzyaloshinskii-Moriya interaction (DMI), lifetime and the dynamic properties of magnons.

The W(110) substrate has been one of the most extensively investigated systems by means of SPEELS, with elemental films of Co and Fe being grown on top [15, 27, 92, 104, 106, 107, 110, 112]. First ever results using SPEELS on the Fe/W(110) system were achieved by Kirschner *et al.*, thus demonstrating the ability and potential of SPEELS to study magnons in thin films [67]. Later, SPEELS was used to study magnons across the SBZ in [27, 92] and quantify the symmetric exchange interaction. Recently, using SPEELS, the antisymmetric DMI has been demonstrated to have a large effect on the magnon dispersion in the 2ML Fe/W(110) system [104].

The Ir(111) substrate has been used to grow various configurations of thin films which exhibited exotic spin states [3, 35]. In particular a system of interest is the 1ML Fe/Ir(111). It was reported that a lattice of exotic magnetic structures called skyrmions was measured in such a structure by spin polarized scanning tunneling microscopy [35]. The SPEELS experiment is potentially able to quantify the exchange coupling constants and the DMI in this system. The magnetic state of the 1ML Fe/Ir(111) is not easily defined and this presents in itself a challenge for SPEELS, because of the complexity of the magnetic system. The Fe interface in this system can still be probed however, this is done by investigating layered ultrathin films where the interface layer is Fe. Such systems were investigated in this work and in particular included 2ML Fe, 3ML Fe and 2ML Co/1ML Fe/Ir(111).

In this work, different thicknesses and alternating layers of Co and Fe monolayers are grown on W(110) and are studied by means of SPEELS. The magnon dispersion is discussed in the framework of the Heisenberg model. The low interlayer coupling of the films is compared to the elemental films on W(110). The large effect of the DMI on the magnon dispersion is compared to the 2ML Fe/W(110) case. The other system that is investigated is the Ir(111) system with films of 2ML Fe, 3ML Fe and up to 17ML Fe thickness. The low exchange coupling constants in all of the investigated systems are derived from *ab initio* calculations and discussed. For the 2ML Co/1ML Fe/Ir(111) system the interfacial DMI is observed.

This thesis is organized in the following way. In chapter 2, the theoretical background of magnetic excitations is presented where magnons are first described in the Heisenberg model as spin waves and later as Stoner excitations in the itinerant electron model. The antisymmetric DMI is introduced and its effect on the magnon dispersion. Spin-polarized electron scattering is discussed in section 2.3. Chapter 3, presents the experimental methods used in this work, the material characterization techniques, the SPEELS spectrometer and the sample preparation. Chapter 4 presents the experimental results of thin films on W(110) in terms of the symmetric Heisenberg exchange interaction and the antisymmetric DMI. Chapter 5 presents the experimental results of thin films on Ir(111) in terms of the symmetric Heisenberg exchange interaction and the antisymmetric DMI. Finally, chapter 6 summarizes and concludes the results which is followed by brief outlook.

2. Theoretical background

In this chapter the theoretical framework for magnetic excitations is introduced along with how this pertains to spin-polarized electron energy loss spectroscopy (SPEELS). In section 2.1 magnetic excitations will be introduced and discussed. There we will look at the mechanisms of spin wave excitation, describing them within the Heisenberg model and the Stoner excitations with their relationship to spin waves in the itinerant electron model. In section 2.2, the antisymmetric Dzyaloshinskii–Moriya interaction (DMI) is introduced and how it affects the spin wave dispersion. The last section 2.3 will look at the principles of electron scattering and SPEELS along with how one would quantify the above said effects.

2.1 Theory of magnetic excitations

Magnetism is a purely quantum mechanical effect. This idea is enshrined in the Bohr-van Leeuwen theorem. Using this theory it can be shown that the partition function Z for N particles with a charge q is not a function of the magnetic field and neither is the free energy of the system. This means that the thermal equilibrium magnetization is zero in classical physics [6]. Such quantities as the electron wave function, spin and orbital angular momentum have to be considered. In 1927 an important result about determining the ground state of a multi-electron system was put forward by Hund [45]. Together these new ideas paved the way to what comes out eventually as the exchange interaction which explains magnetic ordering in solids.

There are various excitations one may access in a solid: vibrational, collective charge density oscillation, and magnetic excitations. These are called, phonons, plasmons and spin waves, respectively. Spin waves are quantized with the quanta of a spin wave called a magnon.
There are two categories into which we can sort magnetic excitations: collective excitations and single particle excitations also known as Stoner excitations. The former can be described in the Heisenberg model which assumes a localized magnetic atomic moment. The latter is within the framework of an itinerant electron model where it is described as an electron-hole pair within the band picture. Between the two approaches, spin waves can be described as a superposition of a number of electron-hole pairs [15]. In this work, we use the term "spin waves" (SW) within the Heisenberg model.
One may use the term "magnon" to refer to magnetic excitations in both the Heisenberg and the itinerant electron model. A magnon has a wave vector Q, an energy E and an angular momentum $1\hbar$. Magnons can be regarded as bosonic quasi-particles and are de-

scribed by the Bose-Einstein statistics.

When thinking of two magnetic moments interacting, it can be thought that they can be coupled together by a dipole interaction since each magnetic moment produces a dipolar field. However this interaction is relatively weak and will come into prominence at low temperatures below 1 K. On the other hand the magnetic anisotropy energy (MAE) is also present but is also relatively weak corresponding to only about 0.1 meV/atom in Fe thin films on the W(110) substrate [79]. However, magnons are observed at much higher temperatures, even higher than room temperature, and therefore another type of interaction between spins is expected.

Heisenberg found that the above mentioned strong interaction is due to the so called exchange interaction where the central ideas are the Pauli exclusion principle and the fact that electrons with the same spin are identical and therefore indistinguishable. This leads to the requirement that the total wave function of a multi electron system should be antisymmetric when two electrons are exchanged. The total wave function can be written as a product of the spatial and spin part. This leads to the symmetry requirement that under exchange, when the spins of two electrons are parallel or antiparallel which corresponds to symmetric or antisymmetric spin wave functions, the spatial wave function has to be symmetric or antisymmetric to keep total wave function antisymmetric. It is then evident that the spin wave function affects the real space one and the electrons being differently spacially distributed will have different electrostatic interactions due to the strong nature of the Coulomb force. Nevertheless, this is a short range interaction since it depends on the overlap of electron wave functions.

Just like for other excitations that have energy dispersion relationships associated with them, magnons also have a characteristic dispersion relationship. Depending on which range of wave vectors one wants to probe, the interaction mechanism is different and therefore the measurement method would be different. For wave vectors $|\mathrm{Q}| > 10^{-2}$ Å^{-1}, magnons are governed by the exchange interaction, while for wave vectors $|\mathrm{Q}| < 10^{-3}$ Å^{-1} the dipole-dipole interaction is dominant. There is an intermediate range between approximately 10^{-3}–10^{-2} Å^{-1}, where both dipole-dipole and the exchange interaction can have comparable effects [19].

In this work the wave vectors studied are between $\pm\ 0.25 - 1.3$ Å^{-1} . It is then appropriate to use the exchange interaction description as a theoretical basis to build on and interpret the measurements. Within this model description two approaches can be used: the Heisenberg model where the localized magnetic moment approximation is used and each atomic magnetic moment is localized on that atom and the itinerant electron model where the magnetic moment is delocalized and is carried by an effective wave function.

2.1.1 Spin waves in the Heisenberg model

First, we look at spin waves in the Heisenberg model. We start with a simple depiction of a localized magnetic moment on each atom. When there is an excitation, the magnetic

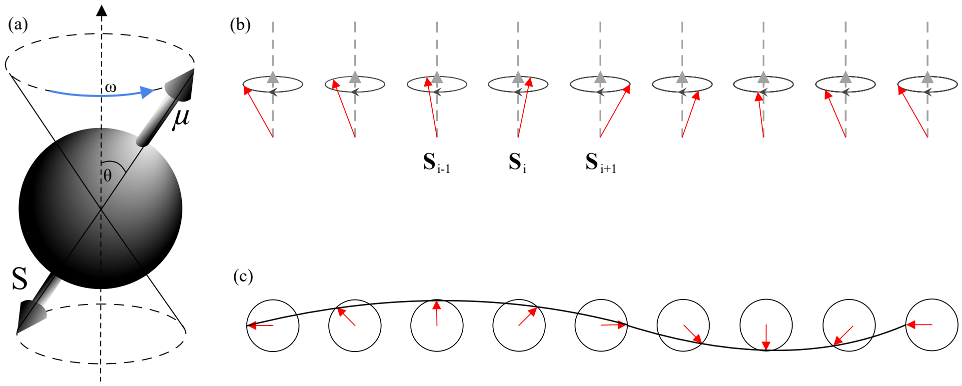

Figure 2.1: (a) An electron with the magnetic moment μ and magnetic angular momentum S, subject to an external magnetic field, precessing around an equilibrium position. (b) Side view of a one dimensional chain (1D) of spins precessing around an equilibrium position with a constant phase difference between each spin neighbor. (c) Top view of a 1D chain of spins. The spin wave of one wavelength is shown.

moment starts precessing around an equilibrium position with a constant phase difference between two neighboring atoms. In a one dimensional chain of magnetic moments depicted in Fig. 2.1, the spin wave is shown having a particular wavelength when there is a change of spin by $1\hbar$. Since the spin waves discussed here are within the exchange interaction picture, we can look at the Hamiltonian which describes the energy due to this interaction:

$$H = -\sum_{ij} J_{ij}\mathbf{S_i}\cdot\mathbf{S_j}, \tag{2.1}$$

where J_{ij} is the exchange constant between two spins $\mathbf{S_i}$ and $\mathbf{S_j}$ and comes from the energy difference between the triplet and singlet state [6]. A positive or a negative J_{ij} indicates ferromagnetic or antiferromagnetic coupling, respectively. Since the exchange interaction has its origin in the Pauli exclusion principle and the Coulomb repulsion, one may expect that the overlap of the involved and localized valence orbitals will decrease drastically between atoms with increasing atomic distances. We will address this later for various systems.

Treating the magnetic spins as classical vectors meaning that the moments are localized on each atom, we can solve the Heisenberg Hamiltonian to obtain the spin wave dispersion relation. Assuming the orbital magnetic moment to be quenched [6], each atom carries an effective magnetic moment of $\boldsymbol{\mu}_{\mathrm{i}} = -\mathrm{g}\mu_{\mathrm{B}}\mathbf{S_i}$. The energy of a magnetic moment $\boldsymbol{\mu}_{\mathrm{i}}$ in a magnetic field $\mathbf{B}$ is given by $-\boldsymbol{\mu}_{\mathrm{i}}\cdot\mathbf{B}$. Then it follows from Eq.(2.1) that given two magnetic moments, the exchange coupling is given as an effective magnetic field

$$\mathbf{B}_i^{\mathrm{eff}} = -\frac{2}{\mathrm{g}\mu_{\mathrm{B}}}\sum_j J_j\mathbf{S_j}, \tag{2.2}$$

with the factor 2 representing the sum over the nearest neighbors twice. In the effective field $\mathbf{B}_i^{\mathrm{eff}}$, the spin $\mathbf{S_i}$ experiences a torque $\boldsymbol{\tau}_{\mathrm{i}} = \boldsymbol{\mu}_{\mathrm{i}} \times \mathbf{B}_i^{\mathrm{eff}}$, and because the magnetic moment is associated with an angular momentum, the spin precesses around the equilibrium position. The time dependence of the angular momentum which is the sum of the torques is then

$$\hbar\frac{\mathrm{d}\mathbf{S_i}}{\mathrm{dt}} = \boldsymbol{\tau}_i = -\mathrm{g}\mu_\mathrm{B}\sum_j \mathbf{S_i}\times\mathbf{B}_i^{\mathrm{eff}} = 2\sum_j J_j(\mathbf{S_i}\times\mathbf{S_j}). \tag{2.3}$$

If the z direction is defined as the spin direction in the ground state or the magnetization direction then one may expand and solve Eq.(2.3) to show

$$\hbar\frac{\mathrm{d}S_i^x}{\mathrm{dt}} = 2\sum_j J_j(S_i^y S_j^z - S_j^y S_i^z) \tag{2.4}$$

and

$$\hbar\frac{\mathrm{d}S_i^y}{\mathrm{dt}} = 2\sum_j J_j(S_j^x S_i^z - S_i^x S_j^z). \tag{2.5}$$

It can be assumed that the deviation from the equilibrium position of the z axis is small and $S_{i,j}^z$ to be the approximately equal to S, the value of the spin moment $\mathbf{S}_i$. Also, S^x and S^y are much smaller than S. The two above equations can be coupled together using the operator $S^+ = S^x + \mathrm{i}S^y$, therefore multiplying Eq.(2.5) by i and adding it to Eq.(2.4), the following is obtained,

$$\mathrm{i}\hbar\frac{\mathrm{d}S_i^+}{\mathrm{dt}} = 2\sum_j J_j(S_i^+ - S_j^+). \tag{2.6}$$

Now, the energy dispersion relation for spin waves can be derived by solving Eq.(2.6) with the ansatz $S^+ = A_i\mathrm{exp}(\mathrm{i}(\mathbf{Q}\cdot\mathbf{R}_i - \omega t))$. A_i is the spin wave amplitude at the position $\mathbf{R}_i$, $\mathbf{Q}$ is the wave vector and ω is the angular frequency of the spin wave. We can insert the expression for S_+ into Eq.(2.6), and after dividing by $\exp(\mathrm{i}(\mathbf{Q}\cdot\mathbf{R}_i - \omega t))$, the following is obtained,

$$\hbar\omega A_i = 2S\sum_j J_j(A_i - A_j\mathrm{e}^{\mathrm{i}(\mathbf{Q}\cdot(\mathbf{R}_j-\mathbf{R}_i))}). \tag{2.7}$$

The above equation is the starting point in the Heisenberg model to derive the spin wave energy dispersion for an arbitrary crystal structure. Since in this work two crystal surface structures were investigated, bcc(110) and fcc(111), we start with deriving the energy dispersion for the bcc(110) case.

W is a bcc metal and the corresponding (110) crystalline structure is shown in Fig. 2.2(a) and (b). One can then extend this to two or more layers and build the spin wave energy dispersion from this. In Fig. 2.2(a), the first two layer stacking is shown with the nearest and next nearest neighboring atoms. We can use Eq.(2.7) to derive the spin wave dispersion in this particular case. The exchange interaction contribution of the nearest and next nearest neighboring atoms to the spin wave amplitude is shown. The subscripts N and NN signify the nearest and next nearest neighbors, respectively, and the propagation direction and contribution $\mathrm{Q}_{\|}$ is inplane. Practically, A_1 and A_2 represent the spin wave

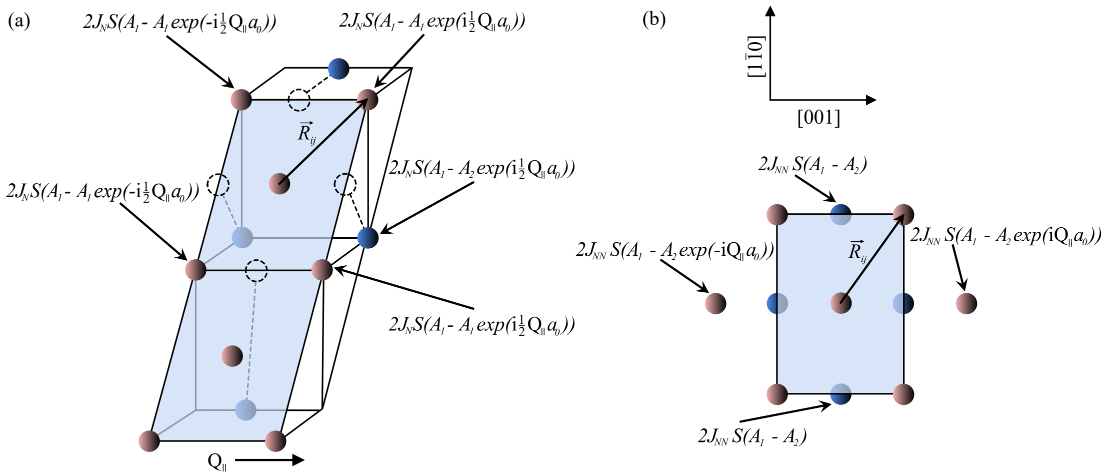

Figure 2.2: (a) An extended bcc(110) surface showing two layers. Each atom in the unit cell has the spin wave amplitude contribution shown for the nearest neighbors. (b) Spin wave amplitude contributions for the next nearest neighbors. The direction of spin wave propagation is shown relative to the crystal.

amplitude in the first and second layer, respectively. Next, we sum up the six terms shown in Fig. 2.2(a) to obtain spin wave amplitude expressions in the nearest neighbor picture in the first layer,

$$\hbar\omega A_1 = 8J_{N\parallel}S[1-\cos(\frac{1}{2}\mathrm{Q}_{\parallel}a_0)]A_1 + 4J_{N\perp}SA_1 - 4J_{N\perp}S\cos(\frac{1}{2}\mathrm{Q}_{\parallel}a_0)A_2. \tag{2.8}$$

For the second atomic layer, we similarly obtain the expression,

$$\hbar\omega A_2 = 8J_{N\parallel}S[1-\cos(\frac{1}{2}\mathrm{Q}_{\parallel}a_0)]A_2 + 4J_{N\perp}SA_2 - 4J_{N\perp}S\cos(\frac{1}{2}\mathrm{Q}_{\parallel}a_0)A_1. \tag{2.9}$$

The variables $J_{N\parallel}$ and $J_{N\perp}$ represent the exchange constants in the plane parallel and perpendicular to spin wave propagation in a specific layer, respectively. Eqs.(2.8) and (2.9) can be rewritten in matrix form

$$\hbar\omega\begin{pmatrix}A_1\\A_2\end{pmatrix} = \begin{pmatrix}8J_{N\parallel}S[1-\cos(\frac{1}{2}\mathrm{Q}_{\parallel}a_0)]+4J_{N\perp}S & -4J_{N\perp}\cos(\frac{1}{2}\mathrm{Q}_{\parallel}a_0)\\ -4J_{N\perp}\cos(\frac{1}{2}\mathrm{Q}_{\parallel}a_0)] & 8J_{N\parallel}S[1-\cos(\frac{1}{2}\mathrm{Q}_{\parallel}a_0)]+4J_{N\perp}S\end{pmatrix}. \tag{2.10}$$

In the above matrix Eq. (2.10), $\hbar\omega$ is the eigenvalue of the matrix on the right side of the equation. We can then obtain analytical solutions for this matrix , assuming that the equation for the wave amplitudes A_1 and A_2 can be solved non-trivially. It then follows,

$$\begin{vmatrix}-\hbar\omega+8J_{N\parallel}S[1-\cos(\frac{1}{2}\mathrm{Q}_{\parallel}a_0)]+4J_{N\perp}S & -4J_{N\perp}\cos(\frac{1}{2}\mathrm{Q}_{\parallel}a_0)\\ -4J_{N\perp}\cos(\frac{1}{2}\mathrm{Q}_{\parallel}a_0) & -\hbar\omega+8J_{N\parallel}S[1-\cos(\frac{1}{2}\mathrm{Q}_{\parallel}a_0)]+4J_{N\perp}S\end{vmatrix} = 0 \tag{2.11}$$

There are two solutions to the above matrix which turn out to be,

$$\hbar\omega = 8J_{N\parallel}S[1-\cos(\frac{1}{2}\mathrm{Q}_{\parallel}a_0)] + 4J_{N\perp}S[1-\cos(\frac{1}{2}\mathrm{Q}_{\parallel}a_0)] \tag{2.12}$$

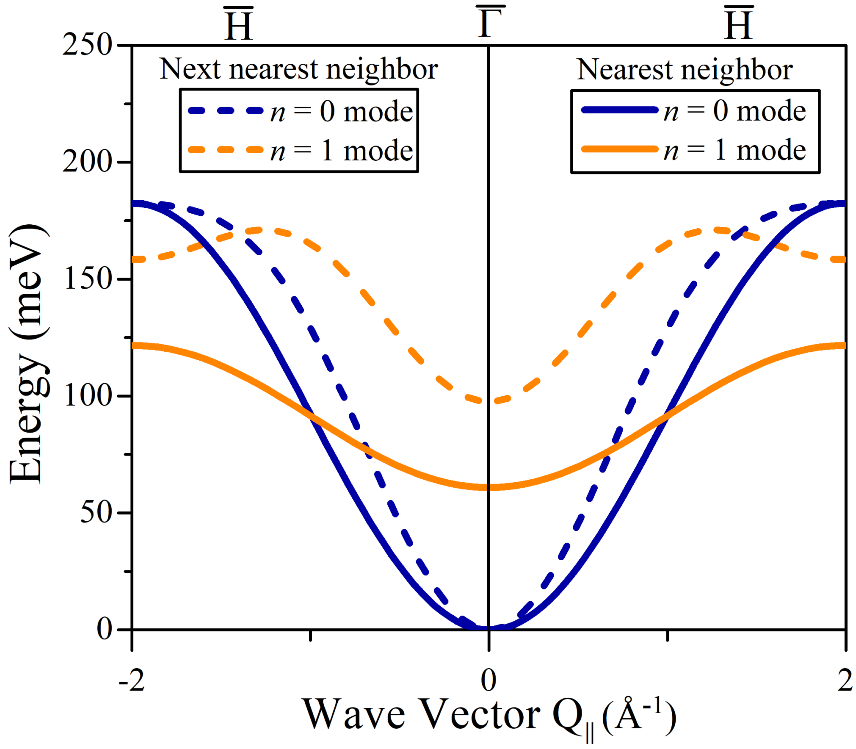

Figure 2.3: Dispersion curves plotted for a two layer infinite slab of bcc(110) crystal. The solid lines plotted from Eq.(2.12) and Eq.(2.13) represent the nearest neighbor Heisenberg (NNH) model. The dashed lines plotted from Eq.(2.16) and Eq.(2.17) represent the next nearest neighbor Heisenberg (NNNH) model. The $n = 0$ mode is represented by the blue color and the $n = 1$ mode is represented by the orange color. The in-plane wave vector $Q_{||}$ is in the [001] direction. For the surface Brillouin zone boundaries, the W(110) surface was assumed.

and

$$\hbar\omega = 8J_{N\|}S[1 - \cos(\frac{1}{2}\mathrm{Q}_{\|}a_0)] + 4J_{N\perp}S[1 + \cos(\frac{1}{2}\mathrm{Q}_{\|}a_0)]. \tag{2.13}$$

The first solution which is Eq.(2.12) is the $n = 0$ mode of the spin waves, this satisfies the Goldstone mode theorem [6, 109]. The second solution, Eq.(2.13), is the $n = 1$ mode and all higher modes are $n \geq 2$. If we substitute Eqs.(2.12) and (2.13) into equations (2.8) and (2.9) then one can see that in the $n = 0$ mode the magnetic spin moments are precessing in phase while in the $n = 1$ mode the precession is out of phase. The two solutions representing the two spin wave modes are plotted in Fig. 2.3.

It was shown in [65] and [110] that in bcc Fe, the next nearest neighbor (NNN) exchange interactions are not negligible and can be as much as 60% of the nearest neighbor (NN) value. Therefore one should consider this and include these interactions into the magnon dispersion calculation. Similar to the NN nearest case, the terms in Fig. 2.2(a) and 2.2(b) are summed up. As a result, the equation for the spin wave amplitude in the first layer is

$$\begin{aligned}\hbar\omega A_1 = {} & 8J_{N\|}S[1-\cos(\frac{1}{2}\mathrm{Q}_{\|}a_0)]A_1 + 4J_{N\perp}SA_1 + \\ & 4J_{NN\|}S[1-\cos(\mathrm{Q}_{\|}a_0)]A_1 + 4J_{NN\perp}SA_1 - \\ & -4J_{N\perp}S(\cos(\frac{1}{2}\mathrm{Q}_{\|}a_0))A_2 - 4J_{NN\perp}SA_2.\end{aligned} \tag{2.14}$$

and similarly for the second layer it is

$$\begin{aligned}\hbar\omega A_2 = {} & 8J_{N\|}S[1-\cos(\frac{1}{2}\mathrm{Q}_{\|}a_0)]A_2 + 4J_{N\perp}SA_2 + \\ & 4J_{NN\|}S[1-\cos(\mathrm{Q}_{\|}a_0)]A_2 + 4J_{NN\perp}SA_2 - \\ & -4J_{N\perp}S(\cos(\frac{1}{2}\mathrm{Q}_{\|}a_0))A_1 - 4J_{NN\perp}SA_1.\end{aligned} \tag{2.15}$$

In this case J_{NN} represents the exchange constant between next nearest neighbors. Because of the added interactions Eqs.(2.14) and (2.15) have more terms than Eqs.(2.8) and (2.9) but they are still linear equations of A_1 and A_2. Similarly as before the dispersion can be calculated to obtain two solutions,

$$\begin{aligned}\hbar\omega = {} & 8J_{N\|}S[1-\cos(\frac{1}{2}\mathrm{Q}_{\|}a_0)] + 4J_{NN\|}S[1-\cos(\mathrm{Q}_{\|}a_0)] \\ & -4J_{N\perp}S\cos(\frac{1}{2}\mathrm{Q}_{\|}a_0) + 4J_{N\perp}S\end{aligned} \tag{2.16}$$

and

$$\begin{aligned}\hbar\omega = {} & 8J_{N\|}S[1-\cos(\frac{1}{2}\mathrm{Q}_{\|}a_0)] + 4J_{NN\|}S[1-\cos(\mathrm{Q}_{\|}a_0)] \\ & +4J_{N\perp}S\cos(\frac{1}{2}\mathrm{Q}_{\|}a_0) + 8J_{NN\perp}S + 4J_{N\perp}S.\end{aligned} \tag{2.17}$$

Eq.(2.16) and Eq.(2.17) represent the $n = 0$ and the $n = 1$ spin wave mode, respectively. The two equations (2.16 and 2.17) are plotted in Fig. 2.3, with the dashed blue and orange curve representing the nearest (NNH) and next nearest neighbor Heisenberg (NNNH) model calculation. The exchange constants $J_{N\|}$ were set equal to $J_{N\perp}$ and $J_{NN\|}$ were set equal to $J_{NN\perp}$. In effect we can write $J_{N\|} = J_{N\perp} = J_N$ and $J_{NN\|} = J_{NN\perp} = J_{NN}$. This means that the inplane exchange constants are equal to the ones perpendicular to the spin wave propagation, from now on referred to as intralayer and interlayer, respectively. Eq.(2.16) and (2.17) will reduce to

$$\hbar\omega = 12J_NS[1-\cos(\frac{1}{2}\mathrm{Q}_{\|}a_0)] + 4J_{NN}S[1-\cos(\mathrm{Q}_{\|}a_0)]. \tag{2.18}$$

and

$$\hbar\omega = J_NS[3-\cos(\frac{1}{2}\mathrm{Q}_{\|}a_0)] + 4J_{NN}S[3-\cos(\mathrm{Q}_{\|}a_0)]. \tag{2.19}$$

The exchange constants used for the plot in Fig. 2.3 that includes the NNNH model were set to $J_N S = 7.6$ meV and $J_{NN} S = 4.6$ meV. The value of $J_{NN} S$ was set to 60% of $J_N S$ which is the ratio of NN and NNN interaction from [65] in bulk Fe. In Figure 2.3, one can notice that the dispersion for the acoustic mode in the NNNH model is stiffer than the one of NNH. This is due to the additional exchange interaction term $4J_{NN}S[1 - \cos(\mathrm{Q}_\| a_0)$ in Eq.(2.16) when compared to Eq.(2.12). For the $n = 1$ mode in the NNNH model, represented by Eq.(2.17), there is shift upward in energy. Comparing Eq.(2.13) and Eq.(2.17) it can be seen that the energy shift upwards is caused by the relative difference of $8J_{NN}S$ along with the term $4J_{NN}S[1 - \cos(\mathrm{Q}_\| a_0)]$. This is due to the NNN interlayer and intralayer exchange interactions whose spins are out of phase and inphase to the central spin from Fig. 2.2.

In the limit of small wave vectors $\mathrm{Q}_\|$ or long wave lengths, the dispersion curve can be approximated by $E = \hbar\omega \propto {\mathrm{Q}_\|}^2 {a_0}^2$ by using the relation $\lim_{x\to 0}\cos(x) = 1 - \frac{1}{2}x^2$. It then follows that Eq.(2.18) can be written as

$$\begin{aligned} \hbar\omega = {} & 12J_N S[1 - 1 + \frac{1}{2}(\frac{1}{2}\mathrm{Q}_\| a_0)^2] + 4J_{NN}S[1 - 1 + \frac{1}{2}(\mathrm{Q}_\| a_0)^2]. \\ & = (\frac{3}{2}J_N + 2J_{NN})S{a_0}^2\mathrm{Q}_\|^2 = D\mathrm{Q}_\|^2. \end{aligned} \tag{2.20}$$

In Eq.(2.20) D is the magnon stiffness coefficient and is valid only in the limit of small Q. An important point is that since spin waves carry a total angular momentum of $1\hbar$, the Bose-Einstein distribution says that as the temperature is reduced, the thermally excited spin waves are mainly the low energy ones from the $n = 0$ mode. Since the reduction of magnetization is the product of excitation of spin waves, the behavior of magnetization as a function of temperature reveals the Bloch $T^{3/2}$ law, assuming a single magnetic domain. This is only valid at low temperatures [6].

For a film thickness of 3 atomic layers, the calculation has been also done analytically in the NNNH model. Starting with Eq.(2.7) and following a similar procedure to the previous cases where one sums each atomic magnetic moment contribution to the spin wave amplitude, we obtain the following equations for the first, second and third layer

$$\begin{aligned} \hbar\omega A_1 = {} & 8J_{N\|}S[1 - \cos(\frac{1}{2}\mathrm{Q}_\| a_0)]A_1 + 4J_{NN\|}S[1 - \cos(\mathrm{Q}_\| a_0)]A_1 \\ & - 4J_{N\perp}S\cos(\frac{1}{2}\mathrm{Q}_\| a_0))A_2 + 4J_{NN\perp}SA_2 + 4J_{N\perp}SA_1 + 4J_{NN\perp}SA_1 \end{aligned} \tag{2.21}$$

$$\begin{aligned} \hbar\omega A_2 = {} & 8J_{N\|}S[1 - \cos(\frac{1}{2}\mathrm{Q}_\| a_0)]A_2 + 4J_{NN\|}S[1 - \cos(\mathrm{Q}_\| a_0)]A_2 \\ & - 2J_{N\perp}S\cos(\frac{1}{2}\mathrm{Q}_\| a_0))A_1 - 2J_{NN\perp}SA_1 + 4J_{NN\perp}SA_2 + 4J_{N\perp}SA_2 \\ & - 2J_{NN\perp}SA_3 - 2J_{N\perp}S\cos(\frac{1}{2}\mathrm{Q}_\| a_0)A_3 \end{aligned} \tag{2.22}$$

$$\begin{aligned}\hbar\omega A_3 = {}& 8J_{N\parallel}S[1-\cos(\frac{1}{2}\mathrm{Q}_{\parallel}a_0)]A_3 + 4J_{NN\parallel}S[1-\cos(\mathrm{Q}_{\parallel}a_0)]A_3 \\ & - 4J_{N\perp}S\cos(\frac{1}{2}\mathrm{Q}_{\parallel}a_0))A_2 + 4J_{NN\perp}SA_3 + 4J_{N\perp}SA_1 + 4J_{NN\perp}SA_3.\end{aligned} \tag{2.23}$$

The solutions to Eqs.(2.21-2.23) are

$$\begin{aligned}\hbar\omega = {}& 8J_{N\parallel}S[1-\cos(\frac{1}{2}\mathrm{Q}_{\parallel}a_0)] + 4J_{NN\parallel}S[1-\cos(\mathrm{Q}_{\parallel}a_0)]+ \\ & 4J_{N\perp}S - 4J_{N\perp}S\cos(\frac{1}{2}\mathrm{Q}_{\parallel}a_0)\end{aligned} \tag{2.24}$$

$$\begin{aligned}\hbar\omega = {}& 8J_{N\parallel}S[1-\cos(\frac{1}{2}\mathrm{Q}_{\parallel}a_0)] + 4J_{NN\parallel}S[1-\cos(\mathrm{Q}_{\parallel}a_0)]+ \\ & 4J_{N\perp}S + 4J_{NN\perp}S\end{aligned} \tag{2.25}$$

$$\begin{aligned}\hbar\omega = {}& 8J_{N\parallel}S[1-\cos(\frac{1}{2}\mathrm{Q}_{\parallel}a_0)] + 4J_{NN\parallel}S[1-\cos(\mathrm{Q}_{\parallel}a_0)]+ \\ & 4J_{N\perp}S + 8J_{NN\perp}S + 4J_{N\perp}S\cos(\frac{1}{2}\mathrm{Q}_{\parallel}a_0)).\end{aligned} \tag{2.26}$$

The solutions represented by Eqs.(2.24−2.26) are plotted in Fig. 2.4. In Fig. 2.4 the exchange constants $J_{N\parallel}$ were set equal to $J_{N\perp}$ = 7.6 meV and $J_{NN\parallel}$ were set equal to $J_{NN\perp}$ = 4.6 meV. Similar as before we can write $J_{N\parallel} = J_{N\perp} = J_N$ and $J_{NN\parallel} = J_{NN\perp} = J_{NN}$.
The other crystallographic surface that was studied in this work was the fcc(111), in our case Ir(111). The crystal structure of an fcc(111) is shown in Fig. 2.5. Starting with Eq.(2.7), the equations with eigenvectors $A_1 \cdots A_N$ can be built up as in previous cases in Eqs.(2.21-2.23) for example, which include the exchange constants up to the third nearest neighbor in the Heisenberg model (NNNNH). The eigenvalue solutions were obtained for a two fcc(111) layer slab of film in the NNNNH model, the solutions are given in Eqs.(2.27) and (2.28),

$$\begin{aligned}\hbar\omega = {}& 4J_NS[4-3\cos(\frac{1}{2}\mathrm{Q}_{\parallel}a_0) - \cos(\mathrm{Q}_{\parallel}a_0)] + 8J_{NN}S[2-\cos(\frac{3}{2}\mathrm{Q}_{\parallel}a_0) - \cos^2(\frac{1}{2}\mathrm{Q}_{\parallel}a_0)] \\ & + 4J_{NNN}S[7-2\cos(\mathrm{Q}_{\parallel}a_0) - \cos(2\mathrm{Q}_{\parallel}a_0) - 2\cos^2(\frac{1}{2}\mathrm{Q}_{\parallel}a_0) - 4\cos^3(\frac{1}{2}\mathrm{Q}_{\parallel}a_0) \\ & + 2\cos(\frac{1}{2}\mathrm{Q}_{\parallel}a_0)]\end{aligned} \tag{2.27}$$

$$\begin{aligned}\hbar\omega = {}& 4J_NS[5-\cos(\mathrm{Q}_{\parallel}a_0) - 2\cos(\frac{1}{2}\mathrm{Q}_{\parallel}a_0) + \cos^2(\frac{1}{2}\mathrm{Q}_{\parallel}a_0)]+ \\ & 4J_{NN}S[3-2\cos(\frac{3}{2}\mathrm{Q}_{\parallel}a_0) + 2\cos^2(\frac{1}{2}\mathrm{Q}_{\parallel}a_0)]+ \\ & + 4J_{NNN}S[5-2\cos(\mathrm{Q}_{\parallel}a_0) - \cos(2\mathrm{Q}_{\parallel}a_0) + 4\cos^3(\frac{1}{2}\mathrm{Q}_{\parallel}a_0)]\end{aligned} \tag{2.28}$$

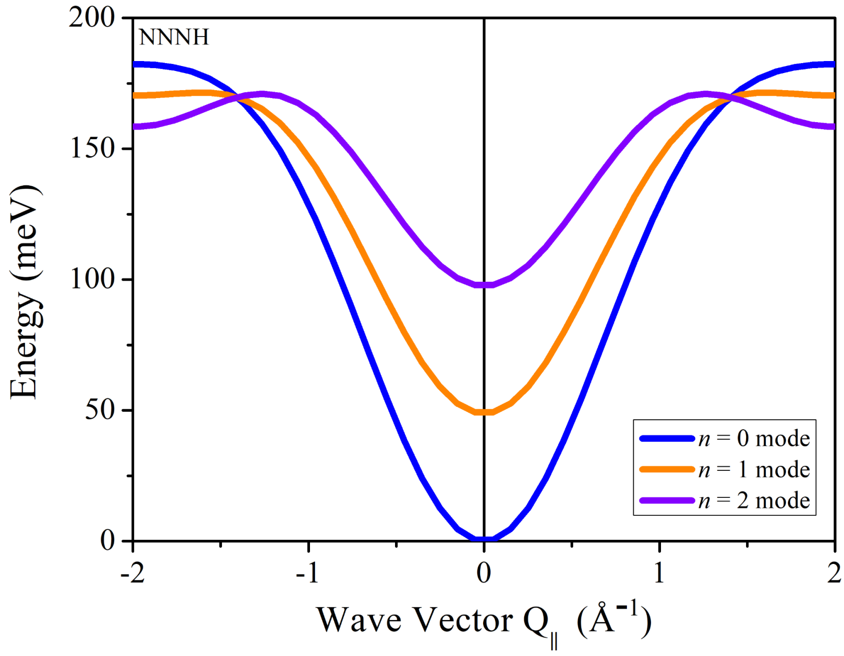

Figure 2.4: Dispersion curves plotted from Eqs.(2.24-2.26) for a three layer infinite slab of bcc(110) crystal. The solid blue, orange and purple line represent the $n = 0$, $n = 1$ and $n = 2$ mode, respectively. The exchange constants values used here are $J_N = 7.6$ meV and $J_{NN} = 4.6$ meV. The in-plane wave vector $\mathrm{Q}_{||}$ is in the [001] direction. W(110) lattice constant $a_0 = 3.16$ Å is taken.

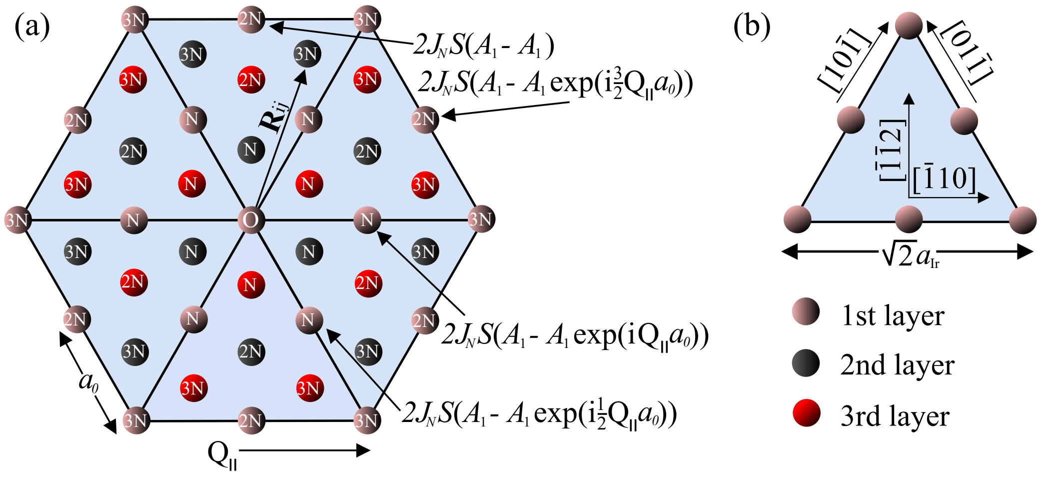

Figure 2.5: (a) An extended fcc(111) surface showing three layers. Each atom in the atomic cell has spin wave amplitude contribution shown for up to 3 nearest neighbors. (b) Crystallographic directions within the fcc(111) surface. The nearest atomic neighbor distance is $a_0 = 2.71$ Å and the Ir lattice constant is $a_{\mathrm{Ir}} = 3.84$ Å. The direction of spin wave propagation is shown relative to the crystal.

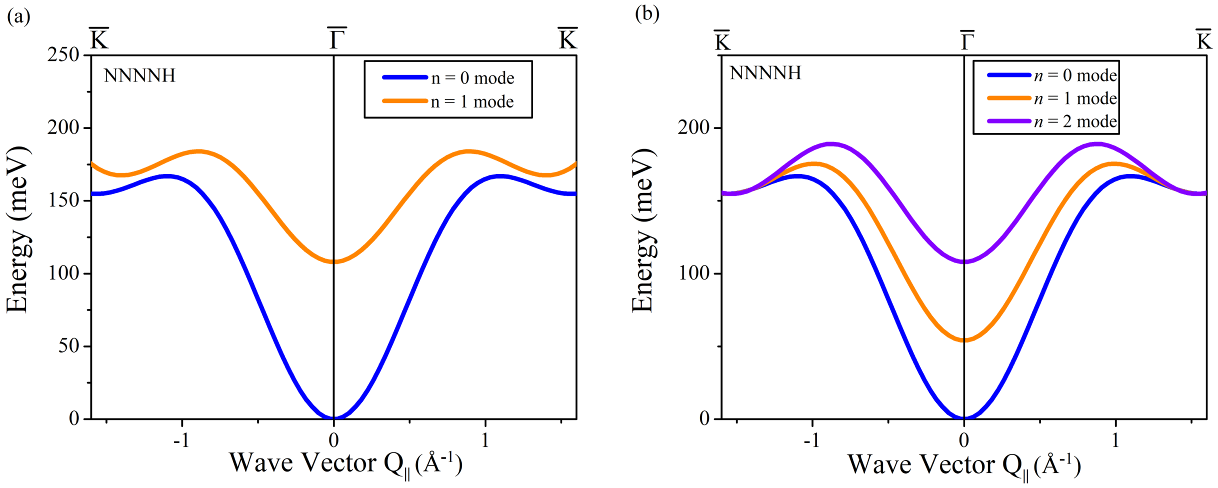

Figure 2.6: (a) Dispersion curves plotted for a two layer infinite slab of fcc(111) crystal. The solid blue and orange curves are represent the $n = 0$ and $n = 1$ spin wave mode, respectively. The exchange constants used are $J_N = 5.6$ meV, $J_{NN} = 3.4$ meV. (b) Dispersion curves plotted for a three layer infinite slab of fcc(111). In layer 1, 2 and 3 the exchange constants used are $J_N = 5.6$ meV, $J_{NN} = 3.4$ meV. All third nearest neighbor exchange constant values have been set to meV for representation purposes only. A nearest atomic neighbor distance of $a_0 = 2.71$ Å is used. J_N exchange coupling constant values taken from [15].

Eq.(2.27) and (2.28) assumes the intraplane and interplane coupling to be equal $J_{N\|} = J_{N\perp}$. Later on in chapter 4 and 5, it will be shown that this assumption has to be changed. The solution given in Eq.(2.27) and Eq.(2.28) are plotted in Fig. 2.6(a).The exchange constants used are $J_N = 5.6$ meV, $J_{NN} = 3.4$ meV and $J_{NNN} = 0$ meV and are taken as a very rough estimate from [15]. The J_{NN} is set to 60% of J_N. The calculation for a 3 ML fcc(111) slab of film are also done in the NNNNH model and plotted in Fig. 2.6(b). The curves in Fig. 2.6 have been plotted including the coupling between first and third layer. The exchange constants used were $J_N = 5$ meV, $J_{NN} = 3$ meV and J_{NNN} for the first layer and second layer. For the third layer the exchange constants that were used are $J_N = 4$ meV $J_{NN} = 2.5$ meV $J_{NNN} = 1$ meV with the coupling between the first and third layer being $J_N = 1$ meV, $J_{NN} = 0.5$ meV and $J_{NNN} = 0$ meV.

When the number of layers is increased above 3 atomic layers, the analytic calculations can get very long and tedious. For the case where the number of layers N is greater than 3, $N > 3$, N number of equations can be established for N number of layers according to Eq.(2.7). For a particular thickness of film N, the spin wave amplitude equations are linear equations $A_1 \cdots A_N$ in layer $1 \cdots N$. These equations can be expressed in similar form to Eq.(2.10) for example to obtain,

$$\hbar\omega \begin{pmatrix} A_1 \\ \cdot \\ \cdot \\ \cdot \\ A_N \end{pmatrix} = \mathbf{M} \begin{pmatrix} A_1 \\ \cdot \\ \cdot \\ \cdot \\ A_N \end{pmatrix}. \tag{2.29}$$

The approach in Eq.(2.29) can be used to derive numerical solutions to N number of layers. In the end there will be an N number of eigenvectors with N eigenvalues obtained. Each eigenvector will consist of spin wave amplitudes $A_1 \cdots A_N$ and shows the precession amplitude of the magnetic moments in each respective layer. Also, Eq.(2.29) implies that for N number of atomic layers, there will be N number of spin wave modes with quantinization numbers $n = 0, 1, ...N - 1$ due to quantum confinement in the direction perpendicular to the film layers [17, 73, 110]. Of these modes, the two lowest energy ones are the surface modes resulting from a lower coordination number of spins at the top and bottom layers of the film. In terms of spin wave amplitudes, the two surfaces modes show high amplitudes in the top and bottom layer and decay exponentially into the bulk of the crystal [28]. If the multilayers are magnetically identical, meaning they are of the same material and surrounding, then it is not possible to separate the contribution of the two surface modes to the layers. However, when the layers become magnetically different, i.e. the exchange constants are different, then the degeneracy of these two surface modes breaks and we may assign a mode to each layer by analyzing the amplitude of the eigenstates A_N in different layers [110].
The Heisenberg model is very powerful in its relative simplicity and the ability to describe experimental results. This approach has had success in describing the experimental data in a number of studies [27, 28, 92]. However, there are shortcomings to the Heisenberg model. For example the spin waves are not damped in this picture and therefore have an infinite lifetime. Therefore another description needs to be given to complement the Heisenberg model and explain experimental data. In the next section we present a brief description of magnetic excitations in the itinerant electron model.

A very important note must be made here. The above derivation of the solutions to the eigenstate equations that were plotted in the bcc(110) and fcc(111) case study, namely in Figs. 2.3, 2.4 and 2.6, are only valid if one assumes that the intra and interlayer exchange coupling constants in all layers are the same. This is because these are analytical solutions and the exchange coupling constants $J_{N,NN..}$ are not distinguished when building up the eigenvector matrix. Therefore their contributions cannot be separated.

2.1.2 Magnetic excitations in the itinerant electron model

Normally, when referring to spin excitations in metallic solids, the term that is assigned is magnons. This refers to the description of spin waves in the itinerant electron model. Therefore the term magnon will henceforth be used to describe excitations in the Heisenberg model and the itinerant model.

In itinerant ferromagnets, magnetism is governed by the itinerant electrons where they interact strongly with each other in momentum space, although it is still possible to imagine that the magnetic moment is partially localized on each atomic site [61, 110]. In reality the electrons have delocalized magnetic moments and are therefore described in the band model of magnetism as was shown by Stoner [88, 89]. When the Stoner criterion is fulfilled then the spin up and down bands in the itinerant electron system spontaneously split by an exchange splitting Δ to save total energy. The net result is more spin states occupation of one direction than the other and the system becomes magnetic. The exchange interaction is responsible for the observed magnetic order in Fe, Co and Ni and not other metallic materials such as Pd and Pt [6].

The excitations that are manifest in the itinerant electron model are the Stoner excitations. These are electron-hole pairs, with electrons and holes in bands of opposite spin sign. Stoner excitations come in two forms, majority spin-hole with minority spin electron state and the minority spin-electron with majority spin hole state. In Fig. 2.7 the majority-hole and minority electron excited state T(Q,E) is shown for a single electronic band of a weak ferromagnet with the exchange splitting U. When the magnon branch enters the Stoner continuum shown in Fig. 2.7(b) then it is strongly damped as there are available Stoner states that the magnon decays into [109]. Analogous to the creation of a spin wave, the Stoner state represented in Fig. 2.7 represents the spin flip of a majority electron, where the exchange splitting U is the energy cost to do so [6]. Contrary to a magnon dispersion relation, the Stoner excitations show a continuum of energies in relation to their wavevector Q. The state T(Q,E) in Fig. 2.7(a) corresponds to the state T(Q,E) in the Stoner continuum represented by an orange circle in Fig. 2.7(b). Due to the weak ferromagnet nature of the band structure in Fig. 2.7 the majority electron band is not completely filled and the minority electron band is nearly empty except for the states near the Brillouin zone (BZ) boundary. This means that some electron-hole states are not available to be produced and therefore in the Stoner continuum there would be a region of lower intensity which is seen as the lighter regions in Fig. 2.7(b). The exchange splitting U is assumed to be constant throughout the BZ and therefore from Fig. 2.7 one can see that the Stoner continuum converges to one point at $Q = 0$. In this case the Stoner state with the minority-electron is exactly vertical relative to the majority-hole shown in Fig. 2.7. At low wave vectors and small energies, single particle Stoner excitations are forbidden and collective excitations or magnons with a particular wave vector Q can be produced [15]. Note, in Fig. 2.7(a) the horizontal axis is the electron wavevector and in Fig. 2.7(b) the horizontal axis is the momentum transfer or in other words the magnon wavevector.

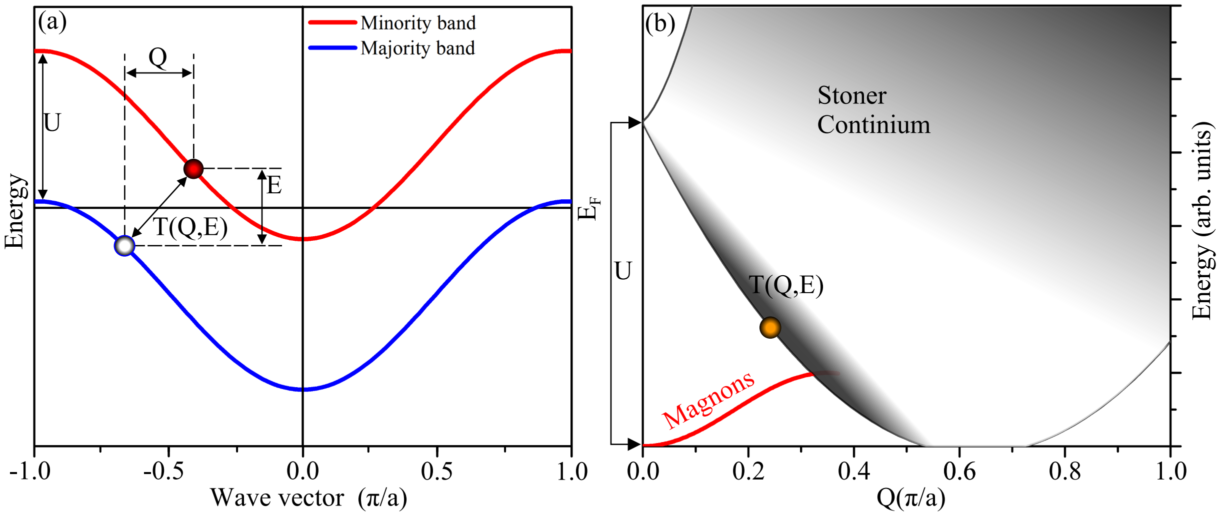

Figure 2.7: (a) A Stoner excitation of a majority-hole with minority-electron character in a weak ferromagnet. The band splitting is denoted by U, the excitation energy T(Q,E) is the state represented by the majority-hole (hollow blue circle) under the Fermi level and the minority-electron (solid red circles) above the Fermi level. (b) A graphical representation of the Stoner continuum of states of the simple electronic band structure from (a). The grayscale represents the density of the Stoner states continuum. The red line represents the single band magnon dispersion which decays strongly into Stoner excitations at the intersection between the magnon band and the Stoner continuum.

While the above discussion is about an idealized scenario, in real world 3d transition metals the electronic band structure is very often much more complicated than the one presented, with multiple bands and non uniform exchange splitting U across the BZ. Accordingly, the Stoner continuum could also be very much different than the one presented in Fig. 2.7(b). In [43, 54] it was found that the Stoner excitations have a broad peak at an energy loss between 2-2.5 eV in an Fe sample. This fit approximately with the average exchange splitting value of Fe. Although the loss peak was rather broad this still enables studies to estimate the band splitting in 3d transition metals [43, 54, 56, 96].

2.1.3 Spin waves and Stoner excitations

So far we have described magnons in the Heisenberg model that assumes localized spins and the Stoner excitations in the itinerant electron model that assumes no correlation between the electron-hole pair. Therefore the Stoner model does not predict any low lying energy bound magnon states. As a result the Stoner model does not give accurate predictions on the Curie temperature but overestimates this value. In 1937 Slater stated that discrete energy level bands can be found under the bands of the Stoner continuum [87]. These discrete bands are correlated electorn-hole excitations that can be interpreted in the Heisenberg model as a magnon. Later on, Herring and Kittel developed the model for magnon states in metals further where they built on the connection between collective excitations and the itinerant electron picture since the latter failed to predict the low energy lying spin wave states. These collective excitations are identical to spin waves in the Heisenberg model, in the limit of small wave vectors [33, 38]. In 1962 Edwards described spin waves as exciton like excitations where an electron of minority spin is bound to a hole of majority spin [24]. Therefore spin wave states may be described as linear superposition of a number of electorn-hole pairs [15]. Magnons that posses any energy can decay into Stoner excitations, which would give the magnons a finite lifetime [37]. As pointed out in Sec. 2.1.2 the decay of magnons is greatly intensified when they enter the Stoner continuum as seen in Fig. 2.7.

One of the most common ways of treating magnons theoretically is to use the so called adiabatic approach. Here, there are effective atomic spin magnetic moments which are coupled by the Heisenberg exchange interaction [109], and the Hamiltonian used is the one introduced in Eq.(2.1). In this approach it is assumed that the precession of magnetic moments is much slower than the electron motion in the system and therefore these two quantities can be effectively decoupled. In the limit of small wave vectors and energy this approach works well to calculate the magnon energies, but since it does not take into account the Stoner excitations and therefore provides no information about the lifetime, it is not accurate at high wave vectors where the magnons decay strongly into Stoner states. Nevertheless it is a useful method to not only obtain approximations to magnon dispersions but also obtain the magnon band stiffness D [65].

Another approach to calculate the magnon energy and lifetime is to calculate the dynamical transverse susceptibility which depends on the magnon wave vector and energy. This can be though of as the magnetic response of the system to a transverse applied magnetic field [18, 109]. In this model the magnons which are of collective nature and Stoner excitations are both taken into account. From the imaginary part of the dynamical susceptibility calculation the spectral density function $\mathrm{S}(\mathrm{Q}_{\parallel},\Omega)$ can be obtained which contains the energy and linewidth of the magnons that in turn gives their lifetime [18, 112].

Finally, it is important to mention that in real ultrathin film systems the magnon damping will depend also on the substrate that the films are grown on. As discussed earlier in this section and in Sec. 2.1.2, the Stoner continuum may be very different in ferromagnets such as 3d transition metals than the one presented in Fig. 2.7. On top of that if one has a low-dimensional system such as an ultrathin metallic film grown on top a non magnetic substrate, there can be strong hybridization of the film and substrate states. This can in principle create Stoner states near the Fermi level and introduce an additional decay channel of magnons into single particle excitations at high wave vectors. This effect can be understood in terms of the complex electronic states being created in the interface between the film and substrate [8, 9].

2.2 Antisymmetric exchange interaction (Dzyaloshinskii-Moriya interaction)

When we introduced the Heisenberg symmetric exchange in section 2.1.1 that is responsible for ferromagnetic order, we used a spin Hamiltonian for a system of spins shown in Eq.(2.1). In most ferromagnetic systems when describing the magnon dispersion the symmetric exchange term will be the dominant energy term and describe the energy of the system fairly well [73, 74]. However, in other cases there are terms in the spin Hamiltonian present that can be significant.

One such term is the antisymmetric exchange interaction or the Dzyaloshinskii-Moriya interaction (DMI) who's Hamiltonian is given by

$$H = -\sum_{ij} \boldsymbol{D}_{ij} \cdot \mathbf{S_i} \times \mathbf{S_j}. \tag{2.30}$$

Here $\boldsymbol{D}_{ij}$ is the Dzyaloshinskii-Moriya vector (DM vector). The question is then what would this type of interaction lead to.

In a simple picture of a hydrogen like atom the relativistic transformations of the electric and magnetic fields experienced by the electron from the nucleus lead to an electronic term in the Hamiltonian of that system of the form

$$H_{SO} = \frac{e\hbar^2}{2m_e c^2 r}\frac{\mathrm{d}V(r)}{\mathrm{d}r}\boldsymbol{S} \cdot \boldsymbol{L}, \tag{2.31}$$

where the spin of the electron interacts with the magnetic field, the subscript SOC stands for spin orbit coupling, e is the charge of the electron and m is the mass of the electron, $V(r)$ is the potential energy, $\boldsymbol{S}$ is the magnetic spin moment and $\boldsymbol{L}$ is the magnetic orbital angular momentum. The energy splitting due to the SOC is then given by

$$E_{SO} = \frac{Z^4 e^2 \hbar^2 \langle \boldsymbol{S} \cdot \boldsymbol{L} \rangle}{4\pi\epsilon_0 a_0^3 n^3 l(l+\frac{1}{2})(l+1)}. \tag{2.32}$$

As evident from the above equation, the spin orbit coupling is proportional to the atomic number Z, therefore one would expect a stronger interaction for heavy atoms with higher Z numbers. This is a highly oversimplified picture and will be true for elements that have the same number of nuclear screening electrons [36]. This can be followed by simply looking at each row of the periodic table.

In 1957 Dzyaloshinskii first proposed the Hamiltonian of the form given in Eq.(2.30) purely from symmetry arguments. There it was shown that this favors a state of canted spins rather than a purely antiferromagnetic state and therefore weak ferromagnetism was present [23]. However, no information about how to derive the DM vectors or how the interaction arises was given. Around the same time it was shown by Moriya that this term can be derived by considering the SOC in the Hamiltonian of the electronic system [62]. More recently, it has been found that for a system with large SOC and broken inversion symmetry, exotic ground states appear [7, 29, 110]. In thin films grown on heavy metallic substrates the inversion and translational symmetry is broken at the interfaces of film and substrate which leads to a large DMI.

2.2.1 Exotic spin textures

Exotic spin textures in ultrathin films grown on heavy metallic substrates have been observed, among which are skyrmions [35, 39], antiskyrmions [42] and spin spirals [7]. In such systems, the DMI is large where the substrates exhibit a large SOC. These spin textures are topologically protected non-collinear magnetic spin structures that may be commensurate to the underlying lattice or be observed in isolated forms [35, 39]. In Fig. 2.8, different spin structures are represented. Each spin structure can be characterized by the topological index number S which is defined as

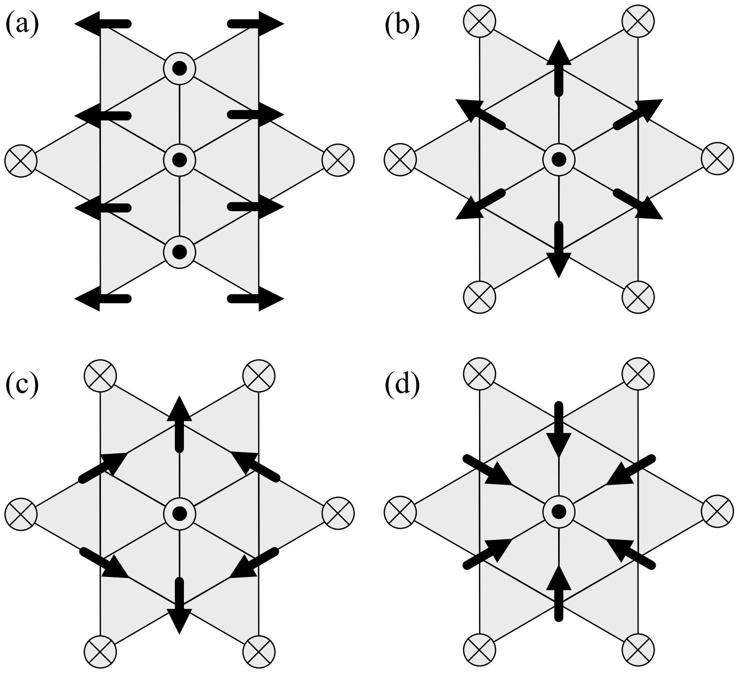

Figure 2.8: Spin structures with the indicated rotational sense of the magnetic moments and their topological index number S. (a) spin spiral, S = 0 (b) clockwise skyrmion, S = +1 (c) antiskyrmionm S = -1 (d) anticlockwise skyrmion, S = +1. Figure taken after [35].

$$S = \frac{1}{4\pi} \int \boldsymbol{n} \cdot \left(\frac{\partial \boldsymbol{n}}{\partial x} \times \frac{\partial \boldsymbol{n}}{\partial y}\right), \tag{2.33}$$

where $\boldsymbol{n}$ is the unit vector of the local magnetic moment and the integral is over a two dimensional space that the spin structure occupies. The topological number S defines the number of times magnetic spins wind around a unit sphere mapped in 3D. For a ferromagnetic or antiferromagnetic state $S = 0$. Different spin structure configurations with their S number are shown in Fig. 2.8. These exotic spin states have been predicted and observed in ferromagnetic thin films grown on non magnetic substrates with a large SOC [31, 110]. In such systems there are interesting cases where antiskyrmions have been predicted [42]. There it is argued that if the underlying crystal structure has C_{2v} symmetry shown in Fig. 2.9(a), then this allows for the formation of antiskyrmions, while C_{3v} Fig. 2.9(b) symmetry favors skyrmions. An example of C_{2v} crystal symmetry would be the bcc(110) surface and an example of C_{3v} symmetry would be the fcc(111) surface.

In order to stabilize exotic spin textures and be able to engineer their size and shape, the ability to control the magnitude and direction of the DM vectors introduced in Eq.(2.30) is key. Such approaches have been realized in [73, 93, 104, 110]. In order to find out the direction of the DM vectors the Levy-Fert model is used and adopted for surfaces [20, 30]. According to this model, the DM vector $\boldsymbol{D}_{ij}$ between two neighboring spins being meditated by a nonmagnetic atom with a large SOC is given by

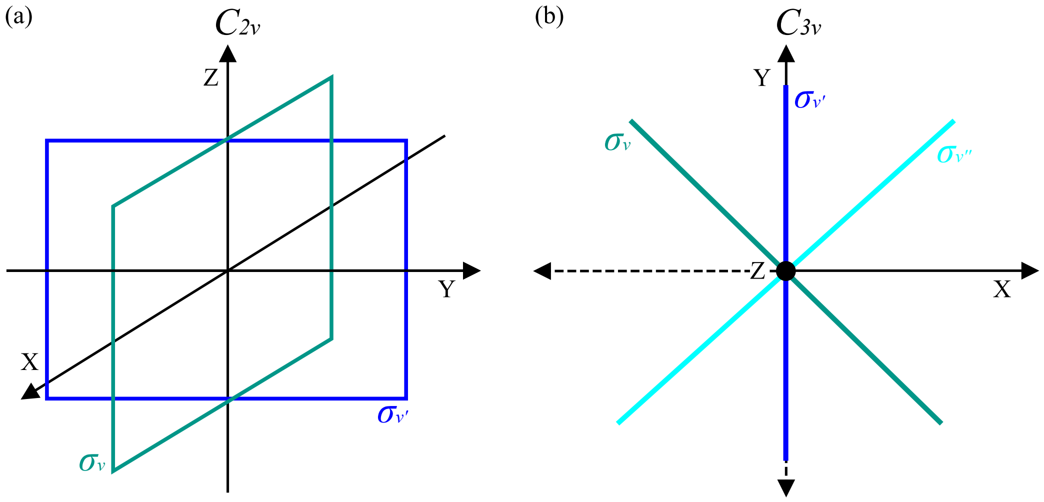

Figure 2.9: (a) C_{2v} symmetry that includes a twofold rotational axis C_2 going through two mirror planes σ_v and $\sigma_v^{'}$, hence C_{2v}. (b) C_{3v} symmetry with a 3 fold rotational axis and 3 mirror planes σ_v, $\sigma_v^{'}$ and $\sigma_v^{''}$.

$$\boldsymbol{D}_{ij} = \frac{D_0}{R_{ij}} \sum_n \frac{\mathbf{R}_{in} \cdot \mathbf{R_{jn}}(\mathbf{R}_{in} \times \mathbf{R_{jn}})}{(R_{in}R_{jn})^3}, \tag{2.34}$$

where the $\mathbf{R_{in}}(\mathbf{R_{jn}})$ is the vector joining the magnetic spin at site $i(j)$ to the nonmagnetic site n. D_0 is a constant proportional to SOC and is a measure of the strength of the interaction between magnetic sites i and j.

Until recently, having a quantitative analysis of DM vectors $\boldsymbol{D}_{ij}$ has not been achieved. In 2009 Udvardi showed that in an Fe monolayer on W(110) the magnon dispersion that is normally degenerate in the mirror momentum space plane i.e. E(Q) = E(−Q) is no longer degenerate in the presence of DMI i.e. E(Q) ≠ E(−Q) [94]. This energy splitting between two opposite but crystallographically equal directions can be quantified according to

$$\Delta \mathrm{E} = \mathrm{E}_{\mathrm{DM}}(\mathrm{Q}) - \mathrm{E}_{\mathrm{DM}}(-\mathrm{Q}) = 2c\sin^2(\theta)\sum_{i\neq j}\boldsymbol{D}_{ij}\cdot\hat{e}\sin[\mathrm{Q}\cdot(\mathbf{R}_i-\mathbf{R}_j)], \tag{2.35}$$

where Q is the magnon wave vector, c is the chirality index, $\hat{e}$ is the unit vector of the magnetization, θ is the relative angle between magnetic moments and $\hat{e}$ and $\mathbf{R}_i(\mathbf{R}_j)$ is the position vector at site $i(j)$. The energy splitting due to DMI for a two monolayer bcc(110) and fcc(111) crystal is shown in Fig. 2.10, where it is clear that based on the crystal surface and the value of the DM vectors the maximum energy splitting will appear at a different wave vector Q.

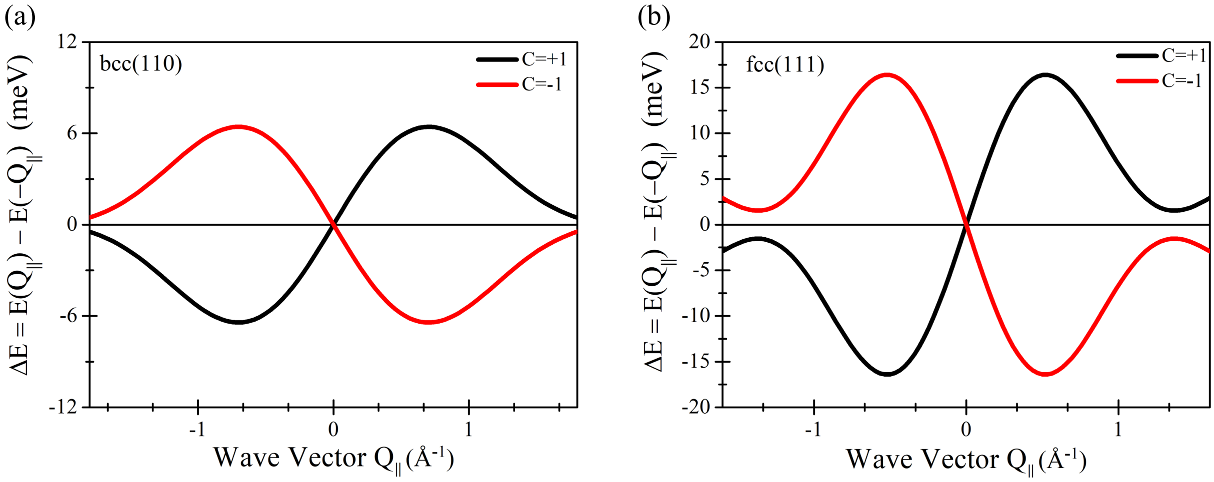

Figure 2.10: (a)$\Delta\mathrm{E} = E_{\mathrm{DM}}(\mathrm{Q}_{\|}) - \mathrm{E}_{\mathrm{DM}}(-\mathrm{Q}_{\|})$ energy splitting due to DMI for a 2ML bcc(110) crystal. The black curve is for chirality +1 and the red curve is for chirality -1. The D_{ij} values used are $D_{1\|} = 0.45$ meV, $D_{2\|} = 0.5$ meV and $D_{1\perp} = 0.45$ meV, where $D_{1\|}$, $D_{2\|}$ and $D_{1\perp}$ represents the DM vectors inplane for the nearest neighbor with the $1\|$ subscript, inplane next nearest neighbor with the $2\|$ subscript and out of plane nearest neighbor with the $1\perp$ subscript, respectively. (b)$\Delta\mathrm{E} = \mathrm{E}_{\mathrm{DM}}(\mathrm{Q}_{\|}) - \mathrm{E}_{\mathrm{DM}}(-\mathrm{Q}_{\|})$ energy splitting due to DMI for a 2ML fcc(111) crystal. The black curve is for chirality +1 and the red curve is for chirality -1. The D_{ij} values used are $D_{1\|} = 0.35$ meV, $D_{2\|} = 0.4$ meV, $D_{1\perp} = 0.35$ meV and $D_{2\perp} = 0.3$ meV, where $D_{1\|}$, $D_{2\|}$ and $D_{1\perp}$ represents the DM vectors inplane for the nearest neighbor with the $1\|$ subscript, inplane next nearest neighbor with the $2\|$ subscript and out of plane nearest neighbor with the $1\perp$ subscript, respectively.

An important note is that the values used for DM vectors in Fig. 2.10(a) and (b) are representative, they are to show that different crystal surfaces as well as the sign of DM vectors will have a large effect on the DMI energy dispersion. From Fig. 2.10 it is clear that the magnon dispersion will not be degenerate along two equal but opposite crystal directions, i.e. $\mathrm{E}(\mathrm{Q}) \neq \mathrm{E}(-\mathrm{Q})$. If we include the energy asymmetry term into the dispersion calculation then this can be seen first hand, the dispersion will be asymmetric.

Fig. 2.11 represents two cases where the energy asymmetry term is included into the magnon dispersion calculation, one for the bcc(110) case and one for the fcc(111) case. The dispersion asymmetry can be best seen if compared to the case where only the symmetric Heisenberg exchange terms are included in the calculation, Fig. 2.3 and Fig. 2.6.

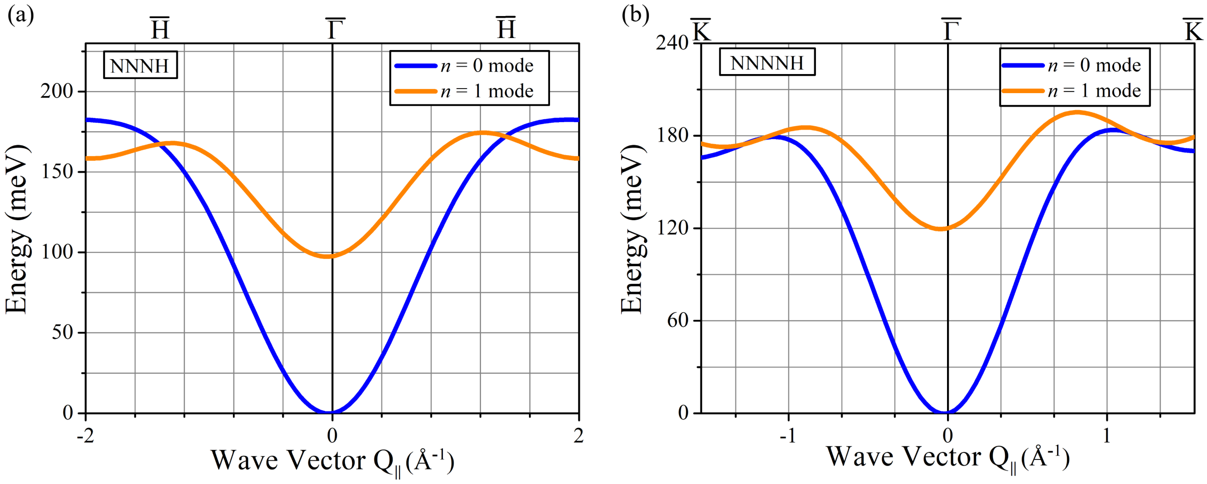

Figure 2.11: (a) Magnon dispersion relation for an infinite two layer slab of a bcc(110) crystal. (b) Magnon dispersion relation for an infinite two layer slab of a fcc(111) crystal. The energy asymmetry terms were included in the calculation according to [94] and values used in Fig. 2.10.

In 2010, in a breakthrough experiment using spin polarized electron energy loss spectroscopy, Zakeri measured the influence of DMI in an Fe bilayer on W(110) and quantified the DM vectors [104]. This novel experiment showed that spin polarized electron energy loss spectroscopy is an appropriate tool to quantify the DMI.

2.3 Spin-polarized electron scattering

Here we give a brief introduction on the principles of spin polarized electron energy loss spectroscopy. This is an experimental technique that investigates spin dependent excitations, in this work the incident electron energies are up to 8 eV. The systems that are investigated are metallic ultrathin films grown on metallic substrates. This technique is surface sensitive due to the small inelastic mean free path of low energy electrons [77]. Electrons scattered from surfaces interact very strongly with the solid in the form of excitations such as magnons, plasmons and phonons which is why they have been used for extensive surface science studies [75]. Using low energy electron energy loss spectroscopy, magnon, phonon and vibrational modes of adsorbates excitations have been studied [46]. In this work we use spin polarized electron energy loss spectroscopy to study inelastically scattered electrons by analyzing their energy loss spectrum.

By analyzing the inelastically scattered electrons in terms of their angular distribution, different loss mechanisms can be identified. Near the specular reflection condition where the electrons have small momentum transfer, the dipolar cone is found. These electrons are scattered due to the long range dipolar fields which are caused by charge density fluctuation [112]. The dipolar fields will scatter electrons well before they reach the surface of the target and therefore a macroscopic dielectric theory can be used to explain the results [58]. Another type of scattering besides dipolar scattering can also be identified, which is the impact scattering. Electrons participating in this type of scattering have larger momentum transfer away from the specular condition. Impact scattering is caused by short range interactions such as the exhange interaction and requires that the electrons enter the solid before any excitation, or in other words energy loss, occurs. The excitations produced here would be mainly electron-hole pairs introduced in section 2.1.2. The theory necessary to have a description of impact scattering is lengthy in derivation and complicated [112] and the reader is referred to the following references for more information [53, 55, 75]. We will assume a simplified picture presented in Fig. 2.12. An electron with a defined spin and energy E_i is incident onto a ferromagnetic surface and the scattered electrons are analyzed in terms of their spin and energy. This is shown in Fig. 2.12 where spin down electrons with an energy E_i are incident onto a surface and electrons with an energy E_i - E are scattered out having either their spin down (non flip process (a)-(c)) or spin up (flip process (d)) relative to the incident electron. In (a) and (c) the incident spin down electron transfer its energy to an spin down (spin up) electron below the Fermi level. The latter electron is then excited to a state above the Fermi level and scattered out. Both (a) and (c) are processes that do not involve exchange interaction. In (b) and (d), the incident spin down electron occupies a state above the Fermi level and transfers its energy to an electron below the Fermi level, the excited electron occupies a state above the Fermi level and is scattered out with its spin parallel (antiparallel) to the incident electron. Both processes in (b) and (d) are exchange processes, however in the later case we can clearly talk about the exchange process where the spin orientation of the scattered out electron is antiparallel (up) to that of the incident electron (up). This we call a spin $flip$ process, although no spin reversal actually takes place, this is a purely exchange process [54]. In such a process the resulting electron-hole pair that is created is correlated and this we call a magnon with its energy and momentum given by the energy and momentum difference between the electron and hole pair.

In this work we employ the spin polarized high-resolution electron energy loss spectroscopy (SPHREELS). We can again refer to Fig. 2.12(d). A spin polarized beam of electrons with a well defined energy is incident onto a ferromagnetic surface that has been magnetized and left in a remanent magnetized state. When the electron enters the solid, it occupies an unoccupied state above the vacuum level. The electron occupies a state above the Fermi level where the density of states of minority and majority electrons is different due to spin band splitting. Since this is a ferromagnet, naturally the empty density of states of minority spins is higher than the majority one. Then, with a certain probability the

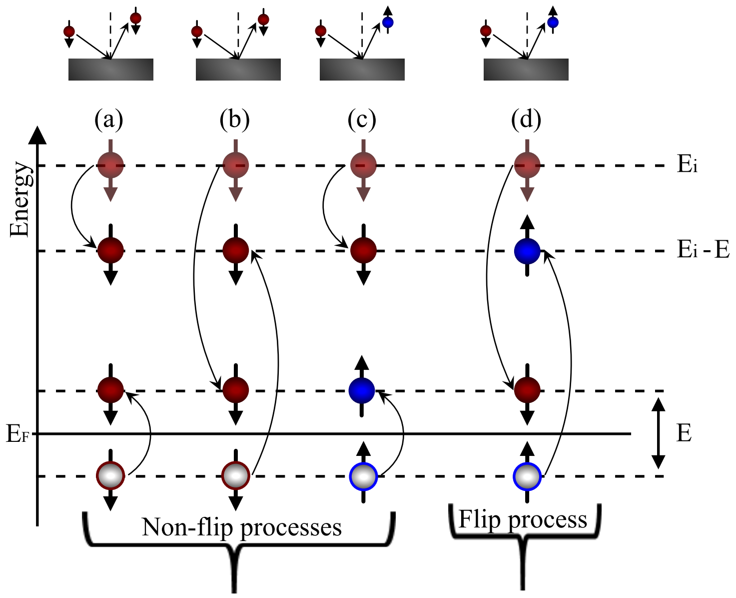

Figure 2.12: A schematic representation of possible scattering processes associated with electron-hole pair generation with an incident spin down electron. The solid arrow balls represent spin down (red) and spin up electrons (blue). Open arrow circles are the holes left behind after the scattering process. E_i is the incident electron energy, E_F is the Fermi level energy and E is the energy loss of the electrons during the scattering process. (a) shows the incident spin down electrons scattering to the same spin orientation without exchange (b) with exchange. (c) and (d) show the spin up electrons scattered out without and with exchange, respectively. The spin of the incident and scattered electrons is the same in (a), (b) and (c), therefore this is called a *non-flip process*. In (d) the spin of the incident electron is flipped compared to the scattered electron, this process we call a *flip process*. An electron of minority character is incident and transfers energy to an electron below the Fermi level and occupies an unoccupied state above the Fermi level. The electron from below the Fermi level of majority character is scattered out with an energy $E = E_i$ - E leaving behind a hole. Figure inspired from [109, 112].

energy of the first electron is transferred to an electron in an occupied spin state of the majority band below the Fermi level. This electron is then excited above the Fermi level and above the vacuum level where it leaves the crystal at an energy E_i - E and is collected by the detector. In the end we are left with an electron-hole pair, with the electron above and the hole below the Fermi level. This process of "spin reversal" is of purely Coulombic nature and happes without any energy dissipation [15].

The experimental procedure of the the above process will be discussed in details in section 3.2, therefore the idea will be very briefly introduced here. During a scattering event where spin polarized electrons with a well defined energy E_i are incident on a ferromagnetic surface, the scattered events are recorded with a channeltron. We assume one scattering event per incident electron. The excitations that happen in the material can be studied by analyzing the energy difference between the incident electron and scattered electron $E = E_i - E_F$ as a function of momentum transfer. This can be selected by varying the geometry of the experiment. Our investigations are restricted to the first Brillouin zone. When a magnon is created in a ferromagnetic solid the angular momentum of the system is reduced by $1\hbar$. Due to the conservation of angular momentum during the scattering process, the spin angular momentum of the outgoing electron must be increased by $1\hbar$ relative to the incident electron. This is only possible if the incident electron is of spin down (minority character) orientation with the spin flip process taking place from down to up. This situation is shown in Fig. 2.12. Since the majority electrons have the spin angular momentum $+1/2\hbar$ and therefore cannot increase this, the creation of a magnon is only possible with a spin down incident electron. Assuming a perfectly polarized beam and ideally magnetized sample, in SPEELS spectra we would observe a 100% spin polarized loss peak. Thermally excited magnons can be annihilated by spin up electrons (majority character) [109].

3. Experimental methods

In this chapter the experimental details are presented. In Section 3.2, the experimental setup including most importantly the SPEELS spectrometer and the principles thereof is discussed. In Section 3.3, the use and preparation of the strained GaAs photocathode is presented. Section 3.4 deals with the growth and characterization of the metallic thin films.

3.1 Experimental setup and operation

The ultra high vacuum chamber is equipped with a SPEELS chamber, an analysis chamber, a sample load lock and a cathode preparation chamber. The analysis chamber contains material sources for sample growth using molecular beam epitaxy (MBE). Sample characterization can be performed in the same chamber by making use of Auger electron spectroscopy (AES), magneto optical Kerr effect (MOKE) and low energy electron diffraction (LEED). The experiments were done under ultra-high vacuum, in the 10^{-11} mbar range. The SPEELS chamber is where the electron scattering experiments are performed. The layout schematic of the experimental setup is shown in Figure 3.1. Various samples and substrates can be loaded through the loadlock chamber and placed on the main manipulator head for investigation. For metallic systems in this work, also the growth of the sample can be performed in situ using molecular beam epitaxy (MBE). This can be done very precisely to sub monolayer thicknesses and will be discussed in Section 3.4. In the SPEELS chamber the pressure is often better than 2.5×10^{-11} mbar. In the following, the working principles of each technique mentioned above are briefly discussed.

3.1.1 Magneto optical Kerr effect

In order to investigate the magnetic properties of magnetic materials, we use our in situ MOKE setup. This technique is very sensitive and therefore can be used for ultra-thin films with thicknesses down to submonolayer.

When polarized light is reflected from a magnetic surface, the polarization plane of the scattered beam is rotated. The amount of this rotation produces a magnetic signal and under some assumptions is proportional to the magnetization component of the film which comes from the geometry of the setup. Three possible configurations are possible for the MOKE experiment: longitudinal, polar and transverse. The in-plane and out of plane magnetization component of the film is measured depending whether one uses the longitudinal or polar setup, respectively. The different geometries are depicted in Figure 3.2. The MOKE setup used in this work can be used as a secondary way to check the

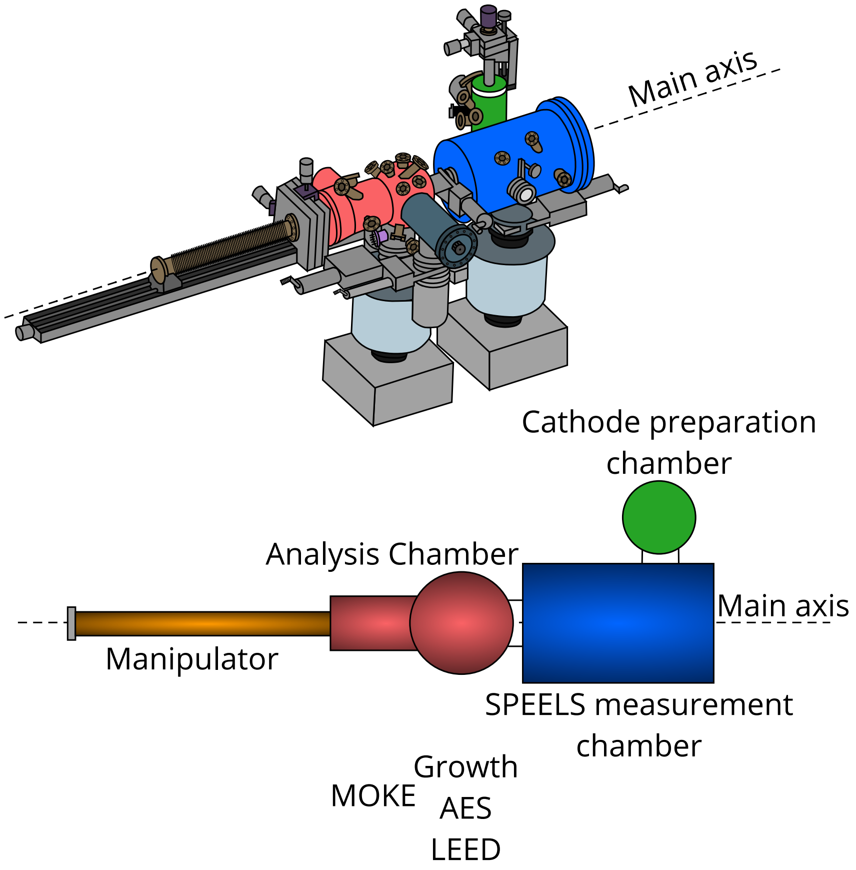

Figure 3.1: 3D drawing of the experimental setup with each corresponding chamber. Top figure shows and actual rendition of the instrument while the bottom figure shows the cross section of the instrument. Adopted from [112].

magnetic film thicknesses calibration. More details on the aspects of the different setups and techniques to measure the magnetic properties of materials using the MOKE are readily available in literature [50, 78, 82, 84, 90].

3.1.2 Auger electron spectroscopy

Surface cleanliness is of utmost importance for studies on ultra thin films. One way to study whether or not the surface of a material is contaminated with unwanted adsorbates or materials is to perform a chemically sensitive technique, Auger Electron Spectroscopy (AES). The general principle of an Auger electron process is shown in Figure 3.3, with two types of transitions shown. In an Auger process, a primary beam of electrons with a defined energy in the range of a few keV is incident on a sample and knocks out a core electron creating a hole, following which both electrons leave the atom. This leads to an excited state of the atom and an electron from a higher level falls to fill the hole as a consequence an electron from a higher energy level is excited and ejected into the vacuum

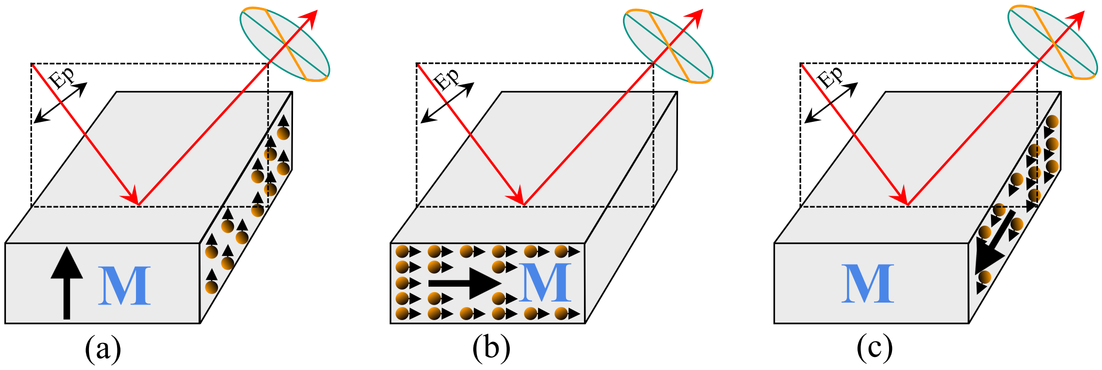

Figure 3.2: Schematic of three different geometries for a MOKE experiment. In part (a), the polar case is shown, where the out of plane component of the magnetization is measured. In part (b), the longitudinal case is shown, where the in-plane component of the magnetization is measured. In part (c), the transverse case is shown, where the component of magnetization is measured that is perpendicular to the plane of incidence and parallel to the surface.

(Auger electron). Since there are three electrons involved in the transition process, in principle every element besides Hydrogen and Helium are available to this technique. As far as notation goes, one may look at the $K_1L_{2,3}$ transition as an example. The first letter $\mathbf{K}_1$ represents the initial core hole that is created by the incident electron. The second letter $\mathbf{L}_{2,3}$ represents the level from which the relaxing electron originates. The third letter $\mathbf{L}_{2,3}$ represents the level from which the Auger electron originates. One of the most common energy analyzers used in the Auger spectroscopy experimental setup is the cylindrical mirror analyzer (CMA) which is the implemented in the setup used in this work. The Auger signal is relatively weak since it is competing against a large background due to secondary electron emissions. Therefore to enhance the Auger signal, it is recorded in the derivative mode using the lock-in technique [63].

It should be noted that the sensitivity of this technique makes it suitable for surface studies since at the energies involved the mean free path of the ejected electrons is rather small (up to about a nanometer) and therefore only the electrons from the upper surface layers give information about the chemical composition.

3.1.3 Low energy electron diffraction

When one wants to find out the surface crystal structure of the sample in question, then LEED is an appropriate technique to use. Experimentally, a beam of collimated electrons with an energy between about 10-400 eV is scattered elastically from the crystal and the diffraction pattern is observed on the fluorescent screen. The rules according to which the diffracted pattern can be observed are stated by the three Laue conditions which can be summarized in vector form as

$$\mathbf{k} - \mathbf{k}_0 = \mathbf{G}_{hkl} \tag{3.1}$$

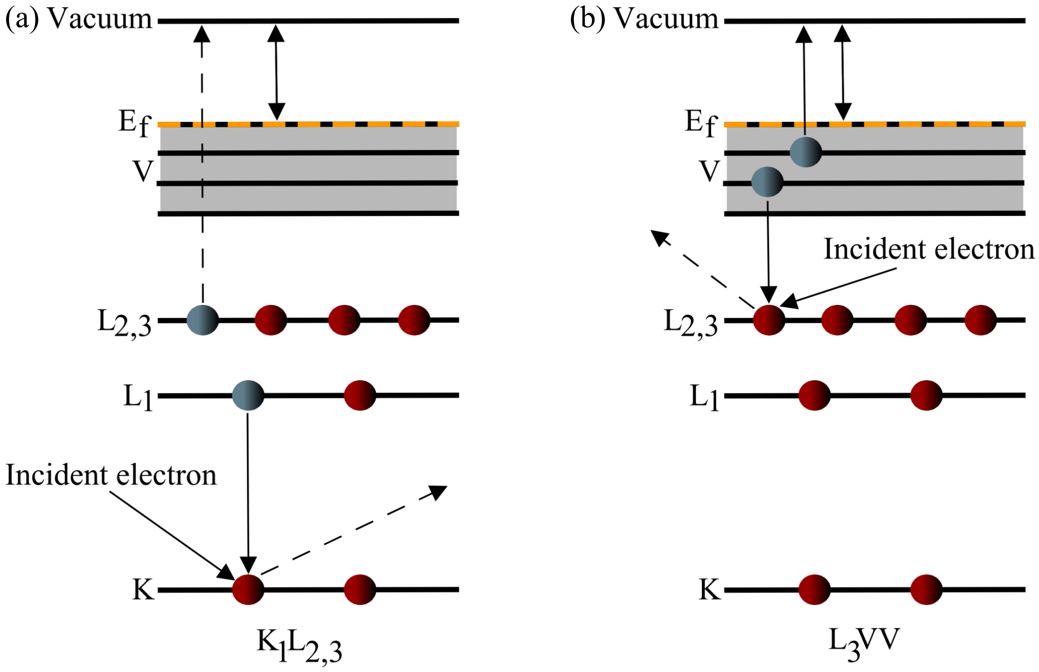

Figure 3.3: Auger electron emission process. Part (a) shows the $K_1L_{2,3}$ and part (b) shows the L_3VV electron emission process. In a solid, when the valence electrons are involved then the L_3VV transition happens for example.

where $\mathbf{k}_0$ is the incident wave vector, $\mathbf{k}$ is the scattered wave vector and $\mathbf{G}_{hkl}$ the reciprocal lattice vector. At the surface the three Laue equations reduce to the two equation case and therefore the wave vectors parallel to the surface are considered and indexed by Miller indices (hk). The penetration depth of the relevant electron energy range is in the range of a few nanometers. Therefore, only the first few layers are probed here and is the reason why there is elastic electron back scattered intensity even where the third Laue condition is not fulfilled [47]. More information about the above LEED experiment in general may be found elsewhere in text [47, 63].

From a qualitative perspective, LEED will give information on the crystal structure. When an adsorbate is present on the crystal surface, then information about the orientation and location of the absorbate relative to the crystal unit cell can be extracted [5]. From a quantitative perspective, the diffracted electrons intensity will produce an IV-LEED spectra which can be used to obtain information on the atomic positions located on the surface. IV-LEED curves are recorded as scattered electron intensity versus incident electron energy and compared to a theoretical curve. The theoretical prediction is then fitted to the experimental data.

For example, one can monitor the intensity of the (00) spot in the LEED patern by rotating the sample. The intensity of this specular beam will have a maximum according to Bragg's law, $2d\cos(\theta) = n\lambda$ where quantized interference n=1,2,3,..., d is the interlayer spacing, λ is the wavelength of the electrons. A more complete analysis of LEED in surface crystallography analysis will require a more complex theoretical approach that takes into account multiple scattering versus the kinematic theory single scattering that has been assumed so far. LEED patterns done in this work will be presented and discussed later on in section 3.4.1 and 3.4.2.

3.2 Spin polarized electron energy loss spectroscopy

In general, in a SPEELS experiment an electron beam with a well defined energy is scattered from a surface being studied. The energy and the in-plane momentum transfer of the scattered electrons are then analyzed for the two different spin orientations. The intensity of the scattered beam is recorded as a function of the energy loss. This would in turn provide information about the inelastic excitations, which could include phonons, plasmons and magnons.

When an electron is scattered from a surface, it either loses energy via an excitation process or gains energy via an annihilation process, then the event is said to be an inelastic scattering event. In the case of one scattering event, the excitation energy is given by $\mathrm{E} = \mathrm{E}_i$-$\mathrm{E}_f$, where E_i and E_f are the initial and final energies of the electrons, respectively. The in-plane component of the electrons is conserved during the scattering process, therefore the inplane wavevector of the excitations can be derived by considering inplane electron momentum transfer $\mathrm{Q}_\| = -\Delta\mathrm{K}_\|$. Starting with the energy for a free electron

$$\mathrm{E}_{i,f} = \frac{\hbar^2 \mathrm{K}_{i,f}^2}{2m}, \tag{3.2}$$

where m is the mass of an electron, an expression for the in plane momentum transfer can be derived

$$\mathrm{Q}_\| = -\Delta\mathrm{K}_\| = \mathrm{K}_{i\|} - \mathrm{K}_{f\|} = \mathrm{K}_i \sin(\theta_i) - \mathrm{K}_f \sin(\theta_0 - \theta_i), \tag{3.3}$$

where $\theta_0 = \theta_i + \theta_f$ is the total scattering angle, the angle of the incident beam K_i and the angle of the scattered beam K_f, respectively. The parallel component of the incident electrons wavevector to the plane of the film is represented by the $\mathrm{K}_{i\|}$ and the scattered ones by $\mathrm{K}_{f\|}$. An illustration of this can be seen in Figure 3.4. The discussion in this thesis is restricted to the first surface Brillouin zone. Therefore the reciprocal lattice vector $\mathbf{G}_\|$ is not considered in the above discussion.

3.2.1 SPEEL spectrometer and experimental procedure

The SPEEL spectrometer consists of two main parts, the monochromator and the electron energy analyzer, both of which are shown in Figure 3.5. The monochromator consists of a pre-monochromator and a main monochromator which have deflection angles of 90° and 180°, respectively. This is shown in Figure 3.5. The analyzer has a deflection angle of 146°, this can be rotated about the main axis. Both the monochromators and the analyzer

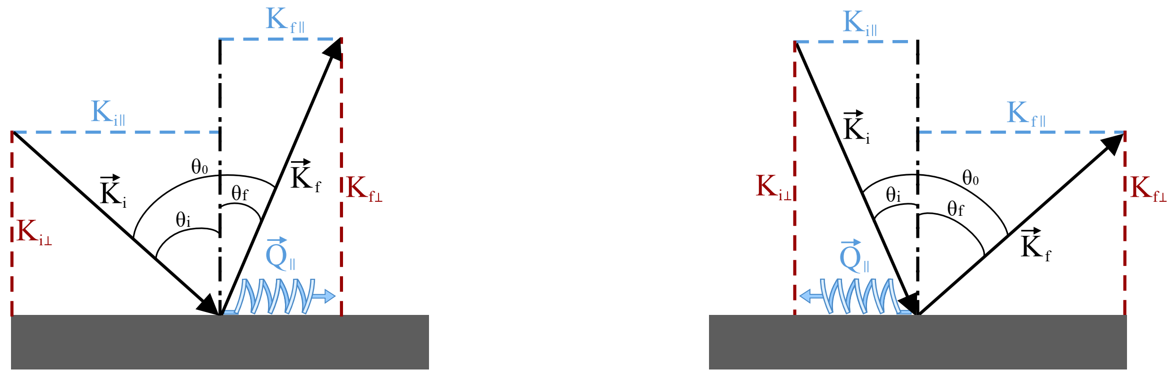

(a) (b)

Figure 3.4: A sketch of the scattering geometry in the SPEELS experiment. The incident wave vector of the electron beam and the scattered one is represented by K_i and K_f, respectively. The parallel component of the incident and scattered wave vector is represented by $K_{i\|}$ and $K_{f\|}$, respectively.

are electrostatic potential deflectors with the aforementioned angles being the angles of deflection. The GaAs photocathode is located in front of the 90° pre-monochromator. It is worth mentioning that the electron beam needs to be highly monochromatic in this experiment with a energy beam width no more than a few millielectronvolts, in order to have a well defined electron beam. Also, since the magnetic excitations investigated in this work are of a magnetic origin, spin -polarized electrons are needed. Due to these reasons, a GaAs photocathode is used as an spin-polarized electron source.

A circularly polarized laser beam with a wavelength of 830 nm is focused on the GaAs photocathode to create the spin-polarized electrons. According to the selection rules the electrons that leave the photocathode are spin-polarized [75], which in this case means having their spins (anti)parallel to the direction of the laser beam depending on the light polarization. In the end to measure surface spin excitations which show spin asymmetry, the spin of the incident electrons should be perpendicular to the scattering plane and transverse to the electron path at the sample. Throughout the path of travel of the electrons, their spin momenta are conserved (along the direction of the laser beam). The spin direction of the electrons can be changed by switching polarization of the laser beam which is done through applying a high potential on the Pockels cell. Here, the electrostatic potentials that the electrons travel throughout the experiment do not affect the spin of the electrons. Therefore, having an odd number of 90° monochromators, electrons will have their spin parallel or antiparallel to the main axis, which happens to be also the sample magnetization axis. The electrons with the proper energy will pass through the monochromators and will be focused on the sample. This is determined by the electrostatic lenses that can be modified.

The analyzer and detector are mounted on the rotatable arm which can be rotated around the main axis in the certain angle θ_0 range between 80° and 280°. Throughout this work θ_0 is kept constant at 80°. Following the analyzer is the channeltron at a high potential

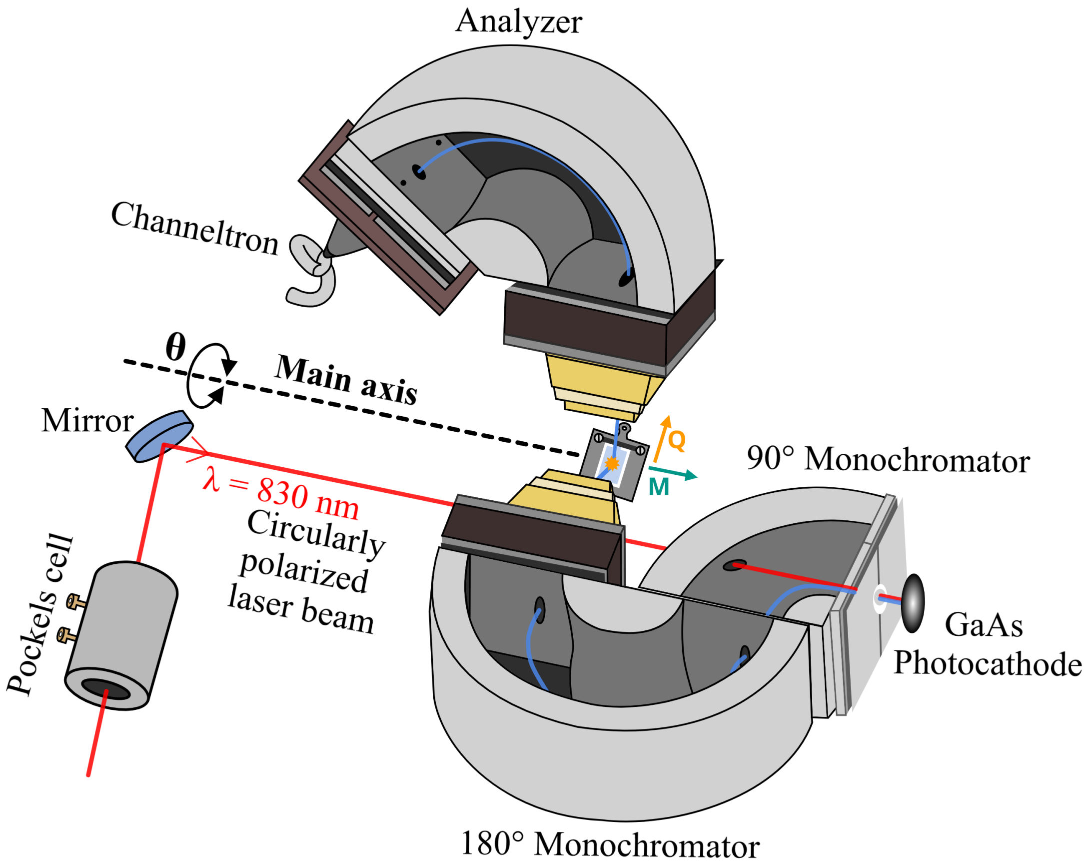

Figure 3.5: A sketch of the SPEEL spectrometer. A circularly polarized laser beam with a wavelength of 830nm is incident on the GaAs photocathode. The emitted electrons move along the path inside the spectrometer indicated by the blue line by electrostatic lenses. The sample can be rotated about the main axis while the angle between the analyzer and the monochromator is fixed at 80°.

of a few kV, which counts the electrons in single counting mode. For a particular spectra, each point of energy loss is set and the number of scattered electrons is counted for both electron beam polarizations, e.g. for each electron spin orientation. After measuring the range of energy loss points desired, the process can be repeated multiple times and averaged to obtain better quality data. In the SPEELS experiment, the energy distribution of the scattered electrons is scanned by the analyzer. The energy resolution of the beam is determined by the kinetic energy of the transmitted electrons which is true for any dispersive element (deflectors in this case). This is called the pass energy. It is highly desireable that the analyzer would have a high resolution since the excitations can have a very narrow linewidth. It is worth mentioning that there is no spin detector after the analyzer. One can then change the the resolution of the electron beam by applying a different potential to the slits. A more in depth description of the SPEEL spectrometer and the general working principles of EELS can be found in [46, 48].

In general, the SPEELS experiment is done in the following way. The substrate is first

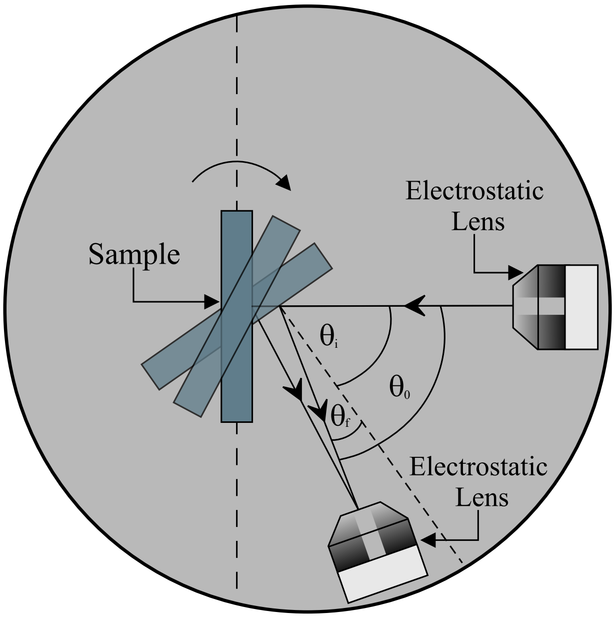

Figure 3.6: The cross section of the measurement chamber int he spectrometer. The wave vector is selected by rotating the sample around the main axis (out of the page). The incident electron beam passes through the electrostatic lenses and is scattered off the sample, following which it is collected into another electrostatic lens and analyzed.

cleaned and the sample that is to be investigated is grown. Then, the sample is magnetized and transferred into the SPEELS measuring chamber (Figure 3.1). The position of the sample is adjusted to be centered as much as possible inside of the scattering cage and thus the scattering process. The electron cathode current that enters first into the 90° pre-monochromator is on the order of μA and by the time that the electron beam travels through the 180° monochromator and scatters off the sample, the beam current drops to about 10 percent of the original value. Most of the incident electrons are conducted away through the sample. The electron beam being scattered from the sample is on the order of nA. This is a way to estimate the intensity of the electron beam incident on the sample, that is one should measure the current being induced in the sample through the electron beam. Since the scattered electrons are only a few percent of the total electron beam, the current induced in the sample can be taken as a rough estimate of the incident beam intensity. After the electron beam is scattered, the electrons are collected and analyzed and the data is sorted into different spectra. In order to probe different sections of the Brillouin zone the wave vector transfer can be adjusted by rotating the sample around the main axis. An example of this is shown in Figure 3.6.

The intensity of the scattered electron beam strongly depends on the geometry of the experiment, where the specular condition (θ_i=θ_f)has the maximum electron beam intensity. The incident electron beam energy is defined by the kinetic energy of the electrons with respect to the vacuum energy level. The primary electron energies used in this work range from 3.2 eV to 8 eV, the higher energies used to probe the higher wave vectors. The resolution of the electron beam can be estimated from the FWHM of the quasi-elastic peak (specularly scattered electrons) which generally ranges between 12-20 meV in this work. An example of a measurement is shown in Figure 3.7, where paritucular wave vector has been measured on a 2ML Fe/W(110) sample. In Fig. 3.7, where the horizontal axis

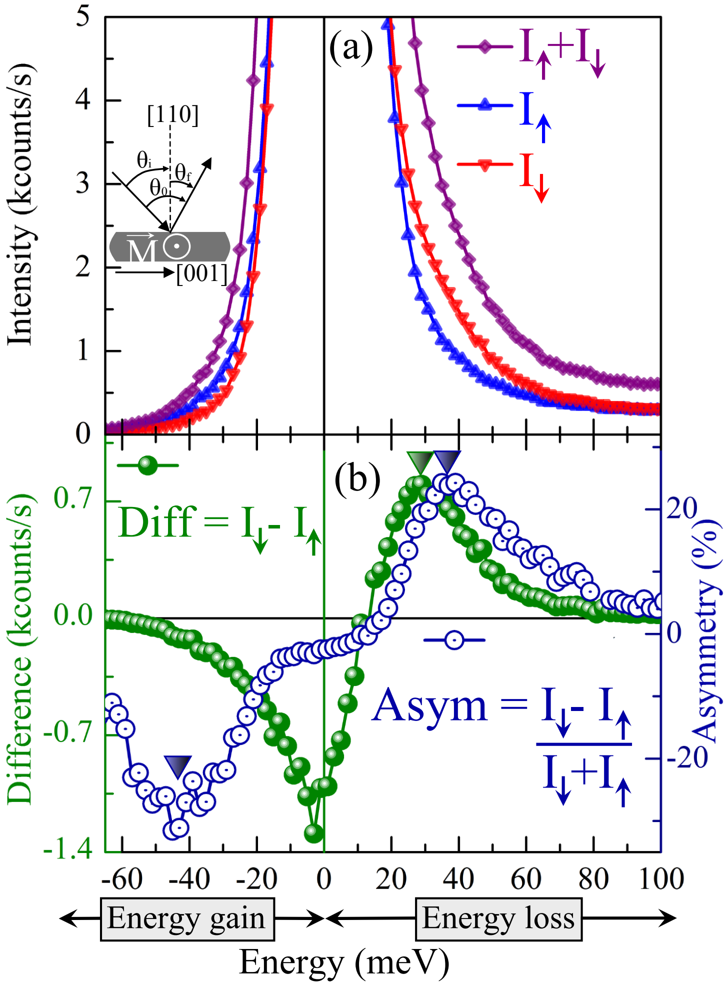

Figure 3.7: (a) SPEEL spectra measured on a 2 ML Fe film, grown epitaxially on W(110) via molecular beam epitaxy. The incident electron beam has an energy of $E_i = 4.2$ eV, with an energy resolution of 18.7 meV. The inset shows the geometry of the experiment, with the electron beam scattered in the [001] crystallographic direction. The measurements are performed in a remanent magnetic state. The total scattering angle $\theta_0 = 80°$ is kept constant at 80°. The in-plane wave vector ($\Delta K_{\|} = K_f \sin(\theta_0 - \theta_i) - K_i \sin(\theta_i)$ was selected to be -0.5 Å^{-1}, where the K_i and K_f are the initial and final momenta of the electrons, respectively. (b) the difference (green) spectra. The large downward triangles show where the spin wave creation and annihilation takes place in the energy loss and gain region, respectively.

has negative values of energy, is the energy gain region. This is where the inelastically scattered electrons gain energy by annihilating thermal excitations (thermally excited spin waves, etc.). The energy loss region in Fig. 3.7, is where the horizontal axis has positive energy values. This is where the inelastically scattered electrons have lost energy due to the excitations created in the sample. In part (a), the up pointing blue triangles represent the intensity of the scattered electrons when the incident electron beam is polarized in a fixed direction, in this case parallel to the spin of the majority electrons. The down pointing red triangles represent the the intensity of the scattered electrons when the incident electron beam is polarized in antiparallel to the spin of the majority electrons and the purple squares signify the total sum of the two scattered electron polarization channels. There is no spin detector present after the scattering events. In part (b), the green full circles represent the difference of the scattered electrons which is defined as Diff $= I_{\downarrow} - I_{\uparrow}$. The blue hollow circles represent the asymmetry of the intensity spectra which is defined as A $= \frac{I_{\downarrow}-I_{\uparrow}}{I_{\downarrow}+I_{\uparrow}}$. These are important quantities to define since they represent the spin dependent excitations. The position of the peaks in the spectra represent the excitation energy and the linewidth of the difference Diff $= I_{\downarrow} - I_{\uparrow}$ gives information on the lifetime of the excitations. One may notice that in the energy loss region the position of the magnon creation peak is different between the difference and asymmetry intensity spectra. The different excitation energy positions of magnons are a purely mathematical effect and have no physical meaning. Because of the definition of the asymmetry, when the quasi-elastic peak is close with respect to the SW, then the spectra is shifted to higher energies. Therefore the difference of the intensity spectra is used for low wave vectors to get information about the SW excitation energy. At higher wave vectors where the weight of the quasi elastic peak is not substantial, then one can use both methods to identify magnon excitation energies. The asymmetry intensity spectra is still useful to get information about the antisymmetric exchange interaction as well as reveal the spin nature of the excitation [109]. In the asymmetry spectra one can also see that the creation and annihilation energies are different, this is due to the antisymmetric Dzyaloshinskii-Moriya interaction (DMI) which was discussed in the chapter 2 section 2.2. Also, the difference spectra does not seem to show a SW annihilation peak in the energy gain region. This is due to the fact that these are thermally excited SWs and the probability of having such an excitation at room temperature, which is given by the Boltzmann factor, is about 0.01-0.1.

Each time in our experiment that an electron is scattered and counted as an event having real values, in the limit of a large number of events it has a normal distribution. This is the Gaussian distribution. The results is an inhomogenous broadening of the spectra. On the other hand, the excitations are of quantum nature and are limited by the Heisenberg uncertainty principle $\Delta E \Delta t \geq \hbar/2$, where the uncertainty in energy of the excitation is ΔE and the lifetime is Δt. This represents the homogeneous broadening of the spectra. From Fermi's Golden rule we know that a quantum excited state will decay exponentially in time [16, 49], and the Fourier transform of that is a Lorentzian distribution of the energy or in other words the frequency domain. The Lorentzian peak can be used to extract the lifetime of the excitation by the following relation

$$\tau = \frac{2\hbar}{\Gamma}, \tag{3.4}$$

where Γ is defined as the linewidth of the Lorentzian peak distribution. The lifetime τ is normally defined as the time that it takes the amplitude or value of the lifetime in this case to drop to e^{-1} of its original value. The Gaussian and Lorentzian functions representing the two broadening mechanisms of spectra can be convoluted to obtain the Voigt function which takes into account both types of broadening. Practically what this means in our experiment is that by fitting our spectra with Voigt functions when appropriate, we can fully describe the excitations present and their lifetimes.

Just by looking at one set of spectra there is a myriad of interesting physics involved. It is then evident that by using SPEELS one can gain a vast amount of information about a particular sample.

3.3 GaAs photocathode

In order to perform a SPEELS experiment, one needs a source of spin polarized electrons. In 1976 D.T. Pierce and collaborators showed that a GaAs photocathode can be used to produce spin polarized electrons [66]. In such a photocathode the *p* bands are split into a four-fold degenerate $p_{\frac{3}{2}}$ levels and two-fold degenerate $p_{\frac{1}{2}}$ at the Γ point, due to the spin-orbit interaction [66]. The net polarization is given by electron excitations via spin selection rules between the valence and the conduction bands using circularly polarized light with a well defined wavelength. However, the maximum degree of polarization that can be obtained is limited to 50 %. This is achieved when the excitation energy is matched to 1.52 eV. The conduction band will then be populated more with electrons having a specific spin direction. The situation is shown in Fig. 3.8. The polarization can be defined as $P = \frac{N_\uparrow - N_\downarrow}{N_\uparrow + N_\downarrow}$, where $N_\uparrow(N_\downarrow)$ is the number of spin-up (spin-down) electrons. From Fig. 3.8, the polarization is then 50 %, when as mentioned above the excitation energy is 1.52 eV.

Spin polarization can be significantly improved if the degeneracy of the upper two valence bands is lifted. This can be done by introducing strain into the epitaxial growth of the GaAs structure [21, 75]. In this work the laser wavelength used to excite the spin polarized photoelectrons from the GaAs cathode was 830 nm, for which maximum a maximum polarization of 80% was achieved [21]. This wavelength also corresponds to the energy gap between the upper valence and the conduction band ($\approx$ 1.49) eV. Since the electron affinity of a strained GaAs photocathode is positive and relative high, alternating cycles of Cs and O_2 can be applied to reduce the electron affinity and even make it negative. In this work this was performed for each cathode, every time the cathode current decayed to an unusable level. An example of this preparation can be seen in Fig. 3.9.

The way to prepare the photocathode is to first clean it by heating it via resistive heating

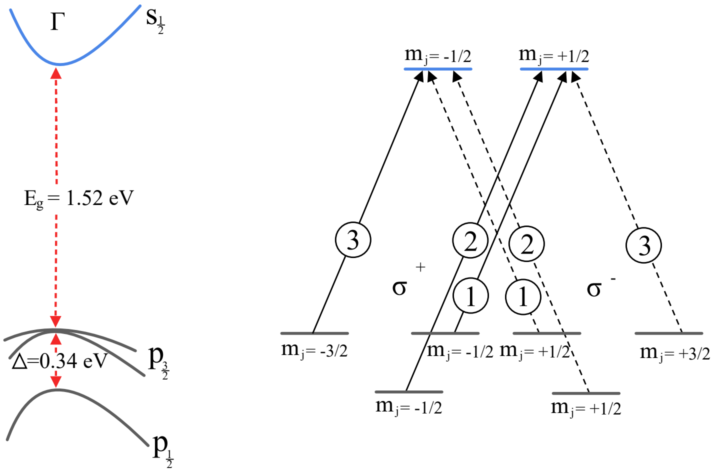

Figure 3.8: Left: Energy vs k diagram showing the energy bands of GaAs near the Γ point ($\Delta k = 0$). The valence bands are split by an energy Δ, due to the spin-orbit interaction. The band gap E_g is a direct one. Right: The degenerate energy levels at the Γ point. Solid (dashed) lines represent the allowed transitions for σ^+ polarized light (σ^- polarized) with the allowed transitions $\Delta m_j = 1$ ($\Delta m_j = -1$). The circles number on the arrows represent the relative transition probabilities as calculated in [66].

by using a tungsten filament. During the first step, the cathode is heated to about 600K and kept at that temperature for about an hour. This is typically done to clean any adsorbates from the cathode which is followed by increasing heating temperature to about 700 K for 10 minutes. After the cathode cools down to 373 K, the Cs is evaporated on the cathode surface where one can observe an increase in the photoelectric current (first blue peak in Fig. 3.9). This is followed by exposing the chamber atmosphere to O_2 through a leak valve, a very strong increase in current is observed (first orange peak in Fig. 3.9). Starting with the first O_2 treatment, after the value of the increased current is maximized, one lets the current decrease to a third of the maximum value. Starting with the second Cs treatment, one would let the photocurrent decrease to half the value of the maximum. In this way, the photoelectric current can be increased by over 3 orders of magnitude. This process is known as the $Yo - Yo$ technique [2]. The amount of Cs and O_2 cycles to be done for each cathode preparation is determined by a few different factors. First, generally one can do more of these cycles and in the end have more photoelectric current as the electron affinity is lowered. Second, the spin polarization of the cathode which is of paramount importance in this work, can be decreased as the excited electrons travel through the Cs_2O layers and there is a higher probability for various scattering processes [66]. Generally, in this work, the amount of cycles varied between 6 and 7 cycles, depending also on which family of GaAs wafers the photocathode came from. The electron current used for a SPEELS experiment was generally 1μA, and when the decay was below the usable limit then the intensity of the infrared laser incident on the cathode was increased. This was done until the maximum intensity was reached and the cathode current decayed

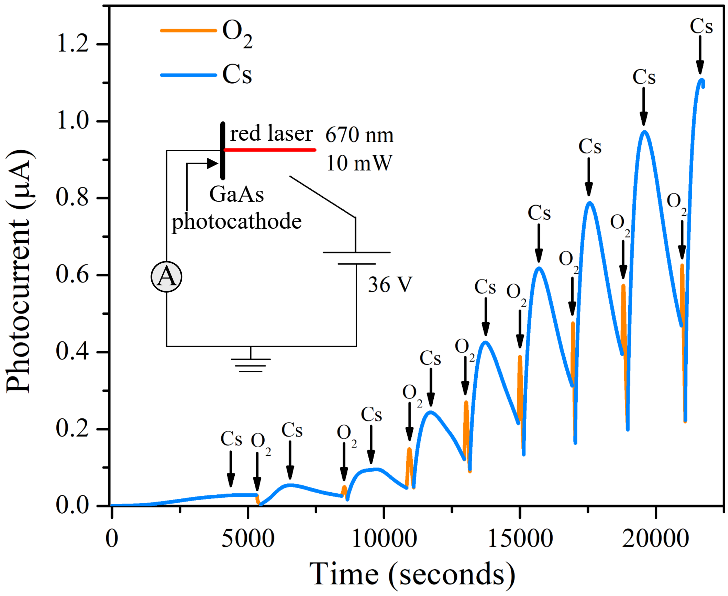

Figure 3.9: Cs and O_2 cycle treatment of strained GaAs photocathode. After heating the cathode via a tungsten filament, the initial Cs treatment is applied (blue curves). This is followed by O_2 treatment (orange curves), subsequent cycles are applied as needed. The photocurrent is produced by a red laser with a wavelength of 670 nm. The block diagram of the circuit is shown as the inset.

beyond a usable level. At that point, the strained GaAs photocathode had to be prepared again (starting with the heat cleaning procedure).

One way to estimate the polarization of the cathode is to measure the spin asymmetry from as nearly a perfect surface as possible. This was done on a clean W(110) surface, where the intensity and the asymmetry of the spin up and down electrons are measured as a function of incident energy E_0 as shown in Fig. 3.10. Since W(110) has a large spin-orbit coupling, a natural consequence is that the intensity spectra of the two spin channels ($I_\downarrow$ and $I_\uparrow$) depends on the incident energy. Also, the difference between the intensity of the scattered spin up and spin down electrons shows a clear asymmetry. The asymmetry is defined as $A = \frac{I_\downarrow - I_\uparrow}{I_\downarrow + I_\uparrow}$, and therefore the highest value of this is found to be at 5.18 eV seen in Fig. 3.10. Practically in the experiment, the asymmetry is defined by the beam polarization P and the ideal polarization factor S whose maximum is 1 and represents the perfectly polarized electron beam. Therefore, one can deduce the lower limit of the electron beam spin polarization at $P = \frac{A}{S} = 68\%$. In previous studies on different W crystallographic surfaces, the degree of spin polarization was not higher than 80% [68, 76, 95]. Therefore this put the higher limit on the polarization.

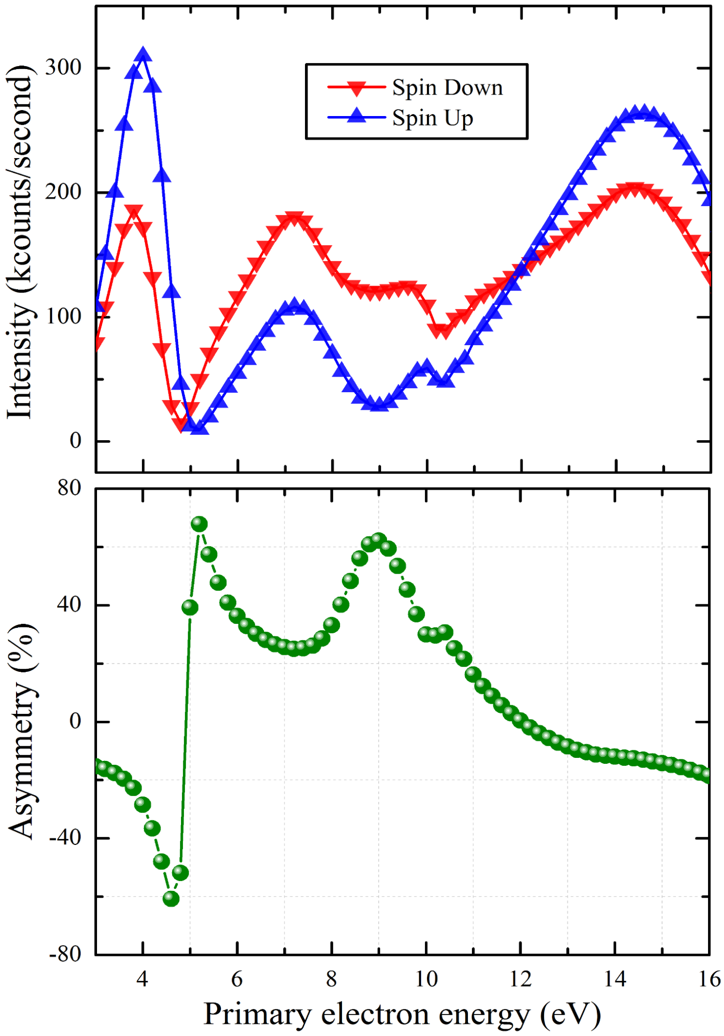

Figure 3.10: Electron scattering from a clean W(110) surface. Top: Intensity of the elastically scattered electron beam for two spin channels (spin up and spin down) as a function of incident energy. The scattered beam is in the [001] direction. Bottom: Asymmetry of the two spin channels, defined by A $= \frac{I_{\downarrow}-I_{\uparrow}}{I_{\downarrow}+I_{\uparrow}}$. The maximum of the asymmetry is 68% at an incident electron energy of 5.18 eV.

3.4 Sample growth and characterization

An important point before performing a thin film scattering experiment is the preparation and characterization of the film as well as the cleaning of the substrate being used.
The substrates are cleaned by treating them in an O_2 atmosphere via intermediate heat pulses referred to as flashes [108]. This technique can be applied to any refractory metal such as Ir and Ru among others. The thin film samples are grown using molecular beam epitaxy (MBE) [63].

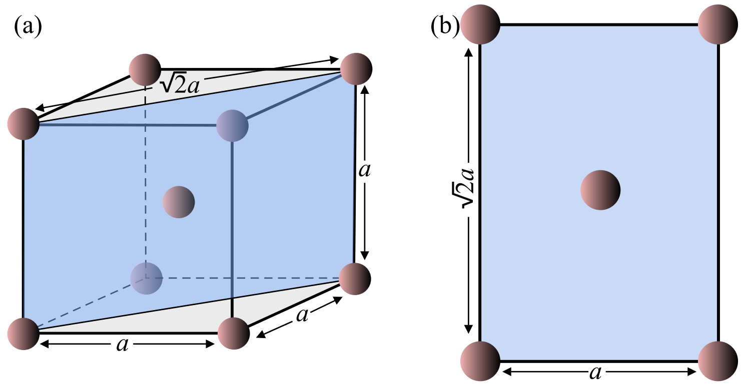

Figure 3.11: (a) Body center cubic unit cell of W, with the (110) surface highlighted in light blue. The lengths are given in terms of the lattice constant $a = 3.16$ Å. (b) The (110) surface with the given lengths.

3.4.1 Co/Fe multilayers on W(110)

The magnetic properties of ferromagnetic metals on tungsten surfaces have been investigated extensively [69, 70, 100–104, 107]. The particular crystallographic surface that was studied in this work is the W(110) surface which is shown in Fig. 3.11. The area of the W(110) surface is 14.12 Å^2 and the surface atomic density is 0.141 atoms/Å^2 which corresponds to 1.41×10^{15} atoms/cm^2. First, before growing any sample on tungsten, one needs to clean it. The most common unwanted contaminations on the tungsten surface are carbon and oxygen [83, 91].

One way to identify if the crystal was effectively cleaned of adsorbates is to perform chemical analysis which can be done using Auger spectroscopy, introduced in Section 3.1.2. Figure 3.12 (a) shows the uncleaned W(110) crystal, where the primary Auger electron energies are color coded, with the unwanted adsorbates clearly shown. It is important to clean the adsorbates not least for the fact that the magnon energies will coincide with the vibrational excitations energies of the adsorbates and therefore wash out the spin excitations. As mentioned above it has been established that an effective way to clean tungsten is to subject it to high power heat flashes in an O_2 rich atmosphere. The procedure was done in the following manner.

Once the tungsten crystal has been degassed as much as possible within a reasonable time, the low power heat flashes were applied in an O_2 atmosphere for 15 seconds each time with a waiting time of 60 seconds between them. The oxygen atmosphere during this step was about 5×10^{-8} mbar. The power of these low power flashes (LPF's) ranged from 35-45 Watts corresponding to about 1200 K and a filament emission current of 30-40 mA at 1.1 kV, depending on the needs. This step is important to remove the oxygen that at this point would have reacted with the carbon at the surface of the tungsten crystal. Following this, the high power flash (HPF) was applied which had a power of about 150-190 Watts

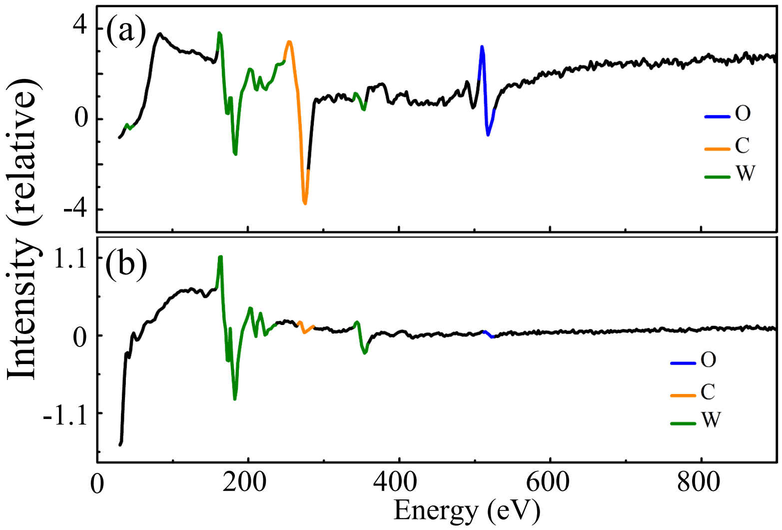

Figure 3.12: Auger electron spectroscopy of (a) before cleaning the W(110) single crystal, (b) after cleaning the W(110) single crystal using heat power flashes in O_2 rich atmosphere, with a subsequent high power flash. Performed at a primary electron energy beam of 3 keV.

with a filament emission current of 150-175 mA at 1.1 kV, in order to remove the oxygen layer remaining at the tungsten surface. Since the melting point of tungsten is 3695 K, the high temperatures involved were appropriate and the structural integrity of the crystal is preserved. The experimental setup for the heat treatment procedure can be viewed in Fig. 3.13 For more information about this cleaning technique, the reader is referred to [108]. After the high temperature treatment in O_2 atmosphere and the subsequent high power flashing, Auger spectra was recorded for the W(110) crystal with the results displayed in Fig. 3.12 (b). As can be seen the crystal is clean and shows no significant adsorbate peaks.

After the tungsten crystal was cleaned, the film growth sources need to be calibrated in order to know the amount of material needed to be deposited for a monolayer equivalent. A monolayer is defined as a unit of film thickness and has the same atomic density as that of the substrate. Iron on the W(110) surface has been well characterized in previous studies in our group by means of medium electron energy diffraction (MEED) as well as by means of torsion oscillation magnetometry in [112] and elsewhere in [98]. Another way to obtain information about the magnetic state of thin films is to use MOKE.

The W single crystal used in this work has the dimensions of 13 mm × 6mm × 0.5mm (length × width × height). The lattice parameter of W is $a_W = 3.165$Å while the lattice parameter of Fe is $a_{Fe} = 2.866$Å. Therefore there is substantial lattice mismatch between the two $\iota = \frac{a_W - a_{Fe}}{a_W} = 9.4\%$. Despite this, Fe will still grow pseudomorphically on W(110) for the first monolayer, with relaxation taking place at 1.2 ML [59, 80]. When the first ML is nearly complete to 90%, the second layer starts growing, this is followed by third layer island coalescence at about 1.8 ML [51]. In our experiments the Fe film thickness

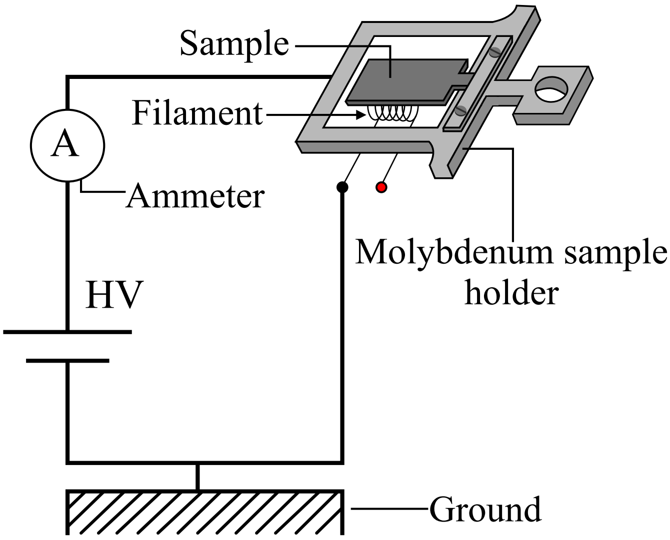

Figure 3.13: Schematic drawing of the high voltage setup for the cleaning procedure of the refractory crystals.

calibration on W(110) has been checked against previous studies by means of MOKE, which was discussed in section 3.1.1. Figure 3.14 shows the Kerr ellipticity signal as a function of amount of material deposited which in turn corresponds film thickness. If one monitors the MOKE ellipticity as a function of film thickness (deposition time), then a ferromagnetic signal would be observed at a certain film thickness which develops with the film thickness. This behavior is due to two fats: dimensionality effects and the finite temperature effect. The Currie temperature of an Fe monolayer is T_c is about 230K [25], and therefore one would not expect to see any Kerr ellipticity signal [70, 71] at that thickness at room temperature. As the thickness of the Fe film is increased, T_c also increases. This behavior is well-known for Fe/W system from several experiments including those performed in our group in the past [112] and [26, 98]. Knowing this qualitative behavior well, we can use our longitudinal MOKE setup to cross check our film thickness calibration. Also in Figure 3.14, in the insets, the magnetic film coercivity is shown for different film thicknesses. We notice that the maximum coercivity of the Fe film is at 3 ML, after which the coercivity decreases. This has been attributed to domain wall pinning at the region boundaries with different film thicknesses as suggested in [81, 112].

In this work, the systems investigated involving the W(110) surface were the following: Co/Fe/W(110), Co/Co/Fe/W(110) and Co/Fe/Fe/W(110). In the case of Co/Fe/W(110), the bilayer structure grows nearly pseudomorphically as seen from the sharp LEED pattern in Fig. 3.16, showing the same crystal structure as that of the W(110) surface. For the trilayer systems one would expect a stronger film relaxation.

Co films grow pseudomorphically up to 0.7 ML after which satellite spots will appear in one direction only and can be observed along with the bcc (110) structure. These satellite spots are a results of lattice strain relief [32]. The Co deposition source was also calibrated

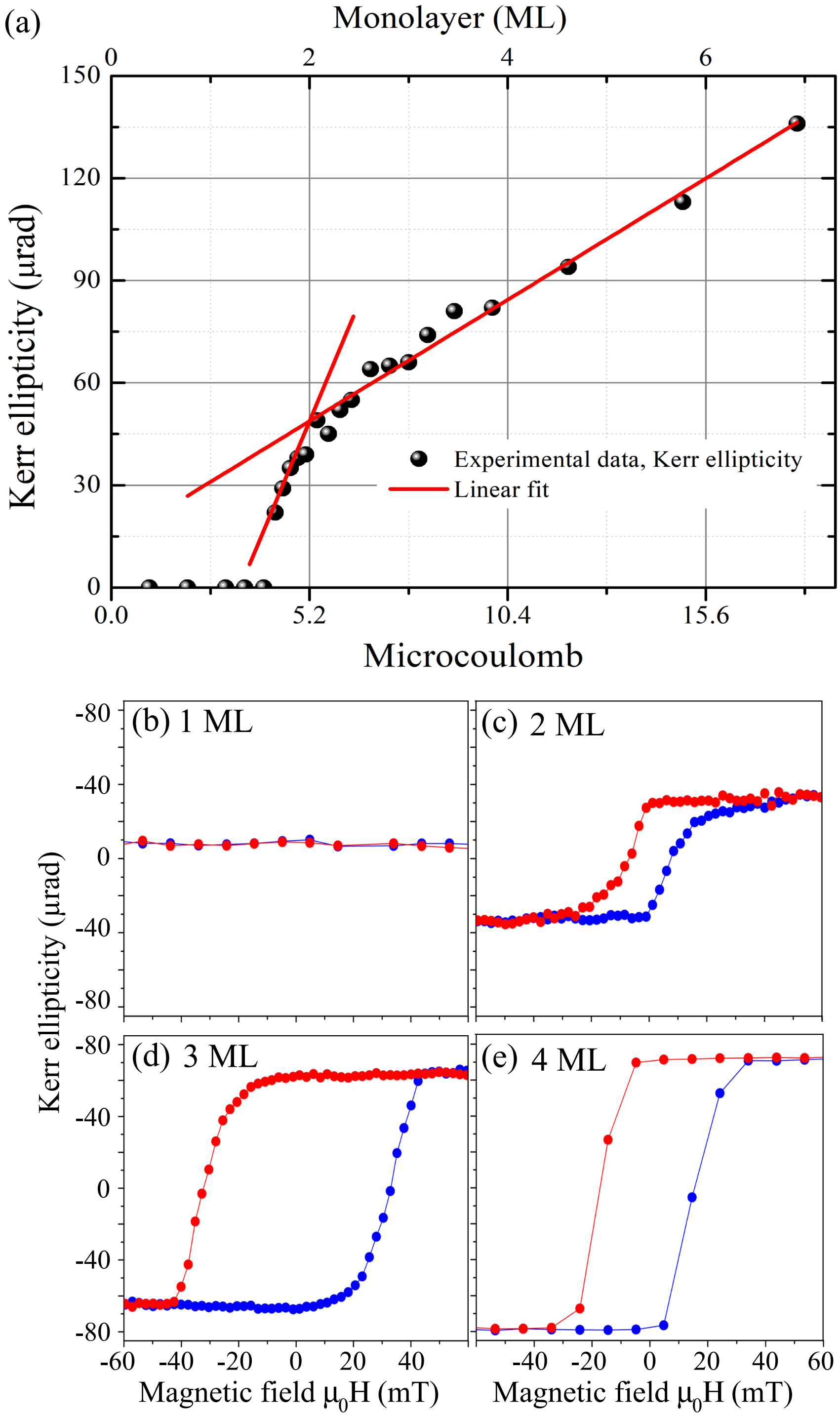

Figure 3.14: (a) Kerr ellipticity versus Fe coverage deposition on the W(110) surface. Light blue dashed line marks the amount of deposited material necessary for a coverage amount of 2 ML. The red lines are linear fits of the curve, crossing at a certain point marking the 2 ML point. (b)-(e) show the MOKE loop for different film thicknesses. More details are presented in the text.

on W(110) in our group in the same manner as the Fe source, however, the behavior is

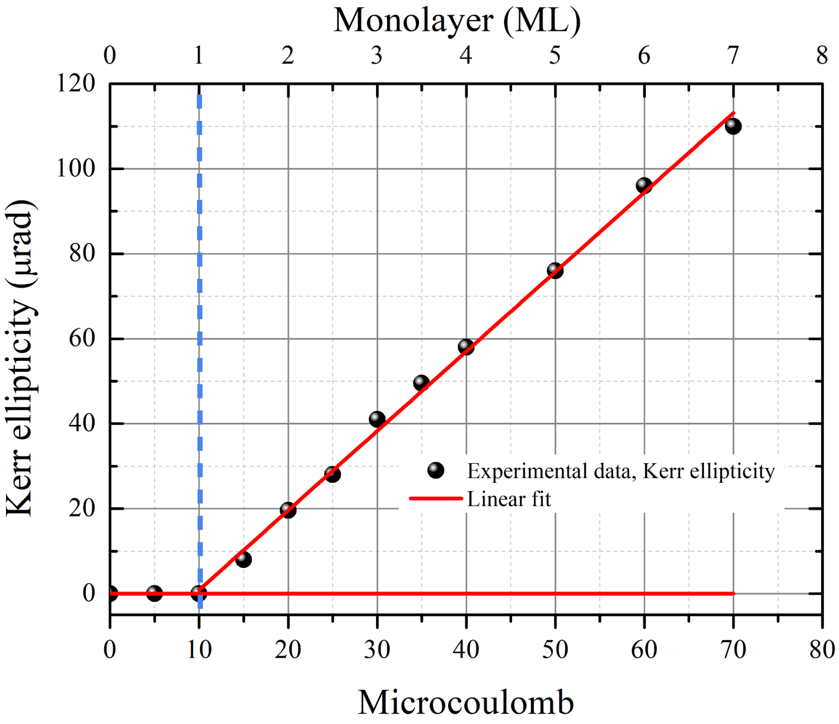

Figure 3.15: Kerr ellipticity versus Co coverage deposition on the W(110) surface. The symbols represent the experimental data. The red lines are the linear fit. The light blue dashed line marks the 1 ML equivalent in terms of micro coulomb.

entirely different. It was shown in [32] where torsion oscillation magnetometery was used, that Co will show a linear magnetic signal response versus the deposited thickness. Extrapolating the data in that work, it is observed that the magnetic response signal starts at just above 1 ML of Co film thickness. In our calibration we have seen the same behavior, the Kerr ellipticity signal versus the amount deposited shows a linear behavior, and the intercept of the curve with the horizontal axis represents the equivalent of 1 ML. The results are shown in Fig. 3.15.

In this work one of the systems investigated was the bilayer structure of Co/Fe/W(110). The Fe monolayer grows pseudomorphically on W(110) as mentioned above. However when the Co ML is added on top pseudomorphic growth is expected up to 0.7 ML after wthich satellites appear in one direction. This was beautifully confirmed in our experiments in the LEED patern taken on Co/Fe/W(110) shown in Fig. 3.16. We observed no satellites in the horizontal direction where one may assume pseudomorphic growth with a strain of about 3.08%. In the vertical direction, satellites were observed. Here the strain can be deduced by looking at the ratio of the superstructure vectors b_1 and b_2. The value of $b_1/b_2 = 0.78$ is obtained, which agrees very well with [32]. By analyzing the LEED pattern further we can also calculate the strain $\varepsilon = [a_{\mathrm{w}} b_1 / a_{\mathrm{Co}} b_2] - 1 = 1.41\%$. These results indicate that the Co film grows in the Nishiyama–Wassermann growth relationship, in agreement with [69]. Performing a MOKE expeirment on a bilayer of Co/Fe/W(110),

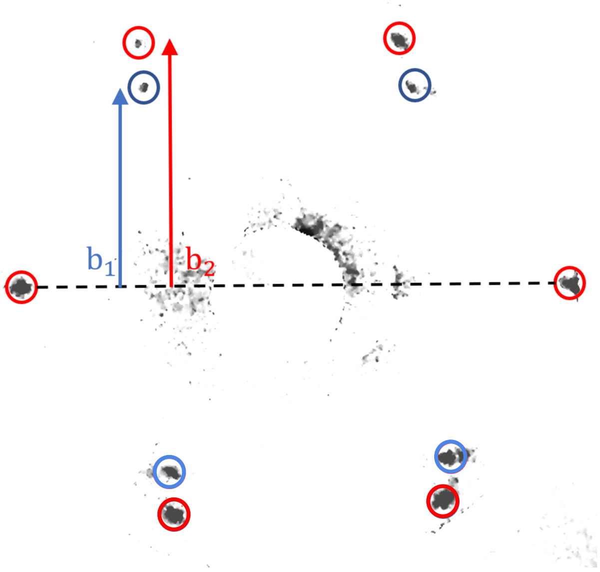

Figure 3.16: LEED pattern of a Co/Fe bilayer grown on W(110) with an incident electron energy of 69.7 eV. The blue circles indicate the diffraction spots due to the pseudomorphic Fe/W(110) film and the red circles represent the Co film superstructure. Vectors b_1 and b_2 represent the observed superstructure.

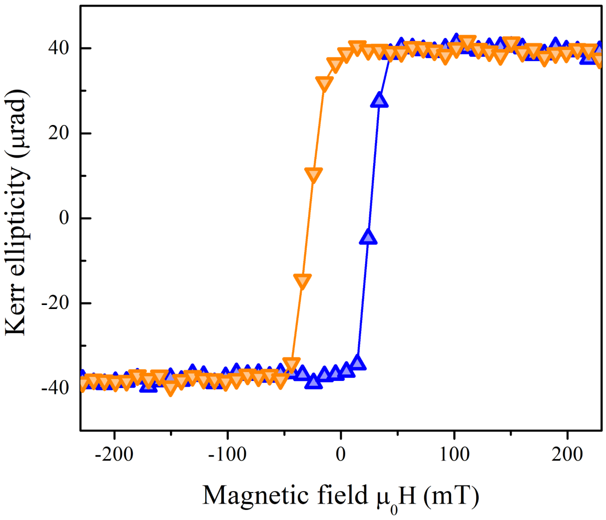

Figure 3.17: A typical MOKE hysteresis loop recorded on a Co/Fe/W(110) between the applied magnetic field of ± 238 mT.

one may expect a ferromagnetic signal, although individually the monolayers of Fe and Co on W(110) do not show a ferromagnetic signal. Indeed it was seen that this is the case as shown in Fig. 3.17. The magnitude of the Kerr ellipticity is roughly the same as of the individual monolayer equivalent taken from Fig. 3.15 and Fig. 3.14.

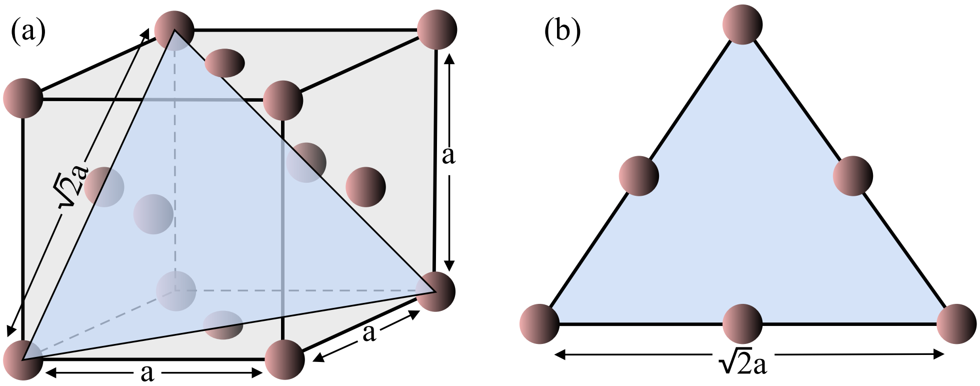

Figure 3.18: (a) Face center cubic unit cell of Ir, with the (111) surface highlighted in light blue. The lengths are given in terms of the lattice constant $a = 3.83$ Å. (b) The Ir(111) surface with the given lengths.

3.4.2 Co/Fe multilayers on Ir(111)

Iridium is another refractory metal that was used in this work. The lattice constant of Ir is $a = 3.83$ Å, with the particular crystal structure shown in Fig. 3.18. The crystal surface under investigation in this work was the Ir(111) surface which has an area of 12.70Å^2. The surface atomic density of the Ir(111) unit cell is 0.157 atoms/Å^2 which corresponds to 1.57×10^{15} atoms/cm^2. Before growing any samples, first the crystal was investigated for cleanliness using AES. Figure 3.19 (a) shows a degassed Ir(111) crystal but not cleaned via O_2 treatment that was described in Section 3.4.1. One can clearly see the adsorbate peaks due to carbon and oxygen at approximately 275 eV and 520 eV, respectively. After cleaning the Ir(111) crystal, the adsorbates were nearly removed and no significant signal from this can be seen, as shown in Fig. 3.19 (b). The parameters used to clean the substrate were the following. For the low power O_2 treatment, the power used was 30-45 Watts with a filament emission current of 30-55 mA at 1.1 kV. The oxygen pressure during this step was $5-9\times10^{-8}$ mbar. For the HPF step, a power of approximately 90-130 Watts was applied, with a filament emission current of 150-160 mA at 0.6-0.8 kV, depending on the needs of the experiment. Since the melting point of iridium is approximately 2739 K, lower power was used to clean this crystal when compared to the tungsten one in order to not damage the crystalline integrity. Accordingly, the cleaning temperatures involved were lower. The iridium crystal has also been cleaned in this work using Ar$^+$ sputtering. In order to remove a film from the Ir(111) substrate, two sputtering cycles were performed at different positions in order to cover the whole crystal evenly. The first sputtering cycle was done at an accelerating energy of 1.5 kV for 50 minutes. After a resting period of 30 minutes, a second sputtering cycle was performed at an accelerating energy of 1.1 kV with a duration of 50 minutes. After these two sputtering cycles, the sample was annealed to make sure that the Ir(111) crystal is atomically smooth. The crystal was checked with AES in order to make sure that the sputtering cycles were sufficient to remove any

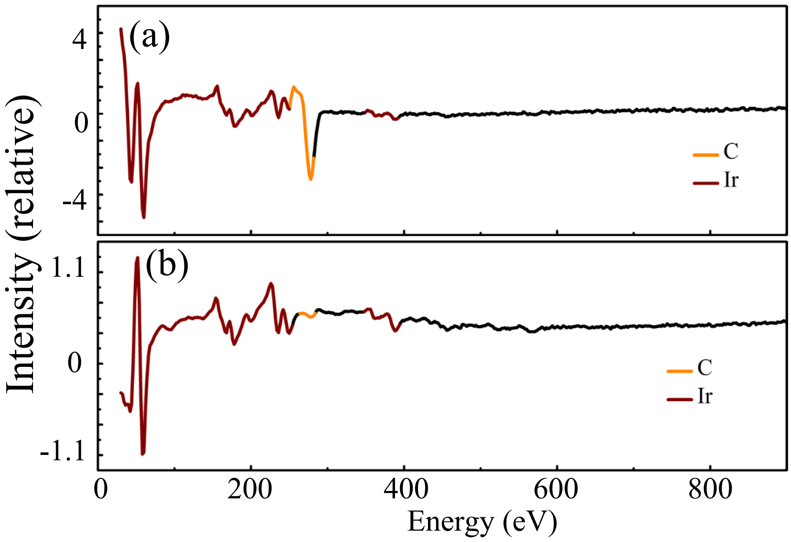

Figure 3.19: a) Uncleaned Ir(111) single crystal. b) Cleaned Ir(111) single crystal using heat power flashes in O_2 rich atmosphere, with a subsequent high power flash.

unwanted adsorbates and films. However, this technique was only used after high power heat treatment was not available at the time. In this case one needs to take extra care not to compromise the surface flatness of the crystal.

When the Ir(111) crystal has been cleaned, the film depositions can be calibrated. Fe will have layer by layer growth up to 3 ML on Ir(111), with relaxation taking place at 2 ML [12]. There are not many studies of film thickness on Fe and Co films (besides perhaps in [10, 12, 41]) deposited on Ir(111). As an auxiliary method to check the film thickness one can look at surface MOKE and AES film to substrate ratio studies [12]. However, these methods would rely heavily on having similar experimental setups. Taking these factors into account, a different approach was taken to calibrate to film thickness of Fe an Co on Ir(111). Since the behavior of Fe and Co on W(110) is well known qualitatively via various studies including MOKE studies as described in Section 3.4.1, by having a calibrated and stable film deposition source one can simply calculate the amount needed to be deposited for a ML equivalent on other surfaces such as Ir(111). The atomic surface density of the W(110) surface is 0.141 atoms/Å^2 and 0.157 atoms/Å^2 for the Ir(111) surface, with both surfaces having 2 atoms per unit cell. Dividing both atomic densities one obtains a ratio which is then weighted against a ML equivalent for the W(110) surface:

$$\frac{\rho_{W(110)} = \frac{0.141 \text{ atoms}}{\text{Å}^2}}{\rho_{Ir(111)} = \frac{0.157 \text{ atoms}}{\text{Å}^2}} \approx 0.9. \tag{3.5}$$

When different samples were grown on Ir(111), nearly all of them showed pseudomorphic growth as confirmed by our LEED experiment shown in Fig. 3.20(a)-(e), the thickness of such samples was up to 3 ML. In the case of thicker samples, i.e. $>$ 3 ML Fe/Ir(111), in agreement with [64], the LEED patern seemed to show broad diffraction spots that point to a deviation from the layer-by-layer pseudomorphic growth. Similar pseudomorphic growth was observed for Co on Ir(111) up to 1.6 ML shown in Figs. 3.20(a) and (b) and for differently layered structures up to 3 ML shown in Fig. 3.22(a). In the case of a layered sample of 2ML Co/1ML Fe/Ir(111) in Fig. 3.22(c) where the Fe interface was annealed, the LEED pattern shows broad diffraction spots. Since the annealed Fe monolayer in Fig. 3.22(a) shows sharp LEED spots, the assumption is that the second Co overlayer undergoes a relaxation and no longer has layer by layer growth. Estimating the film strain from the satellite spots in Fig. 3.22(b),(c) is difficult. The LEED diffraction spots are very broad and therefore deriving the strain ε in the $[\overline{1}\overline{1}2]$ direction for example is difficult. We will address this in more details below, therefore we only comment qualitatively on the growth mode. From the LEED images it is clear that after a trilayer structure of 2ML Co/1ML Fe is grown on top of Ir(111), the Co layers undergo a relaxation and the growth is no longer pseudomorphic. One may assume that this is not even nearly pseudomorphic because the diffraction spots are quite broad.

In summary, we can compare Fe/Ir(111), Co/Ir(111) and Co/Fe/Ir(111) growth in order to get a qualitative idea of the growth mode. From Figs. 3.20(a)-(d) the LEED diffraction spots for the Ir(111) surface and the thin layers of Fe grown are sharp, suggesting pseudomorphic growth. Even for 3ML Fe/Ir(111) in Fig. 3.20(a) this growth seems to be preserved. It is clear that after a 4th Fe layer is deposited, the diffraction spots become broad and weaker in intensity (Fig. 3.20(f)). The annealed case in Fig. 3.20(g) does not improve the diffraction spots in terms of intensity but they are sharper. For the case of Co, the pseudomorphic growth holds until 1.6ML, since the LEED spots appear sharp and no satellites are observed (Fig. 3.21(a)-(c)). However Fig. 3.21(d) starts showing a clear deviation from pseudomorphic growth because one can observe the increased relative size of diffraction spots when compared to the thinner Co films.

For the case of layered films of Co and Fe on Ir(111), pseudomorphic growth is not observed in any of the 4 films grown in Fig. 3.22(a)-(d), In the case of 1ML Fe on Ir(111) the growth of the film was observed to be pseudomorphic, but when 1ML of Co is deposited on top as in Fig. 3.22(a), the diffraction spots are broad and lower in intensity compared to the case of Fe ML in Fig. 3.20(c). Figures 3.22(b)-(d) show a superstructure appearing in the pattern as satellite spots marked by blue circles. Taking Fig. 3.22(c) as an example, we assign two superstructure vectors a_1 and a_2. The value of $\mathrm{a}_1/\mathrm{a}_2 = 0.91$ is obtained. By analyzing the LEED pattern further we can also calculate the strain in the x direction $\varepsilon = [(a_{\mathrm{Ir}}/\sqrt{2})\mathrm{a}_1/a_{\mathrm{Co}}\mathrm{a}_2] - 1 = 2.3\%$. This is much larger than in the previously estimated strain of the Co monolayer film on the pseudomorphically grown Fe/W(110) which was 1.41%. One has to take note of the lattice mismatch between Ir, Fe and Co: ($a_{\mathrm{Ir}} = 3.89$ Å and for the fcc(111) surface the nearest atomic neighbors are 2.71 Å away from each other, $a_{\mathrm{Fe}} = 2.87$ Å, $a_{\mathrm{Co}} = 2.5$ Å in the basal hcp plane).

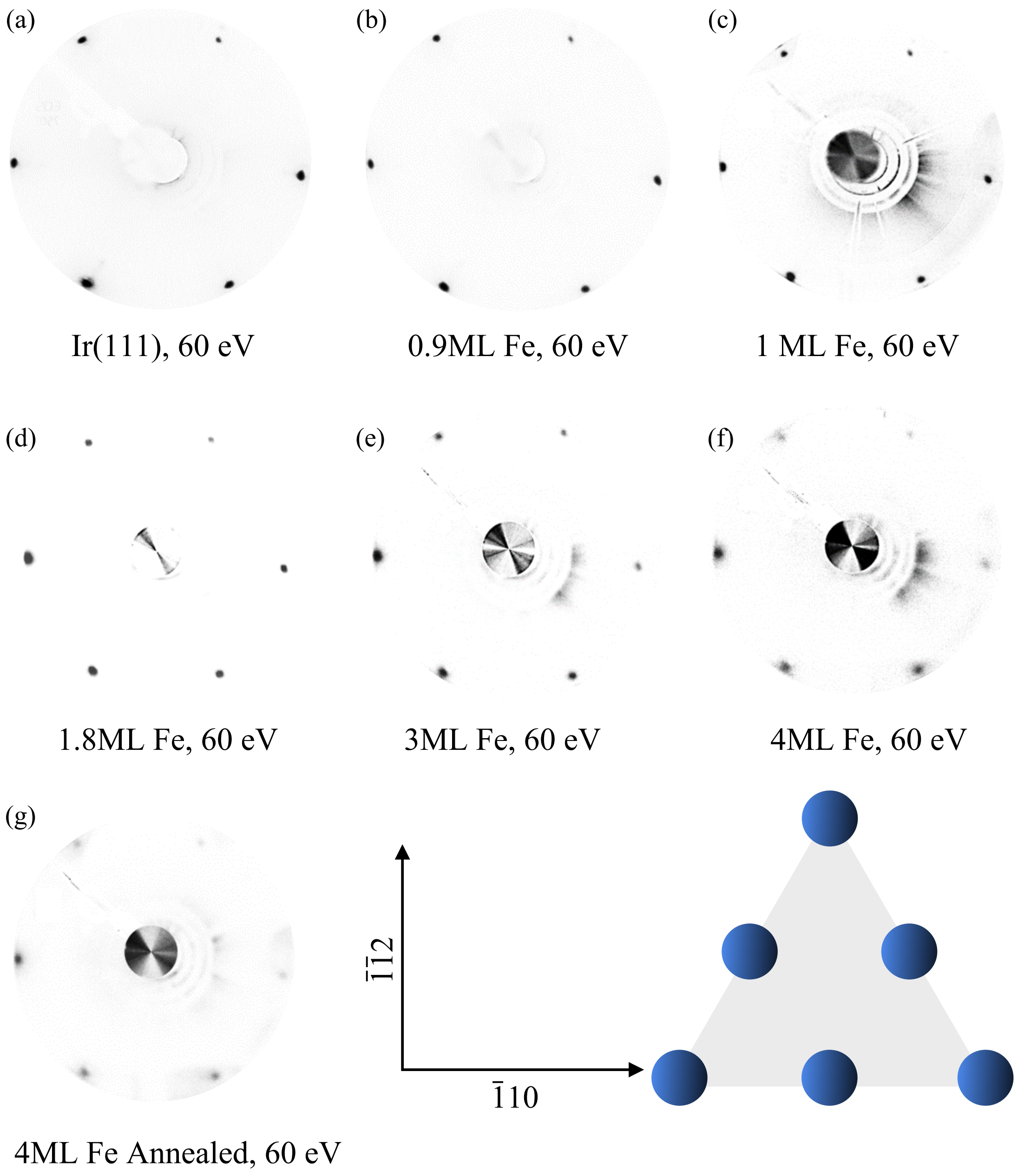

Figure 3.20: Selection of LEED patterns of (a) Clean Ir(111) substrate and (b) 0.9ML (c) 1ML (d) 1.8ML (e) 3ML (f) 4ML (g) annealed 4ML of Fe grown on Ir(111). All images are taken at primary electron energy of 60 eV. Only in (g) the film is annealed. Crystallographic directions and the fcc(111) surface are shown as well.

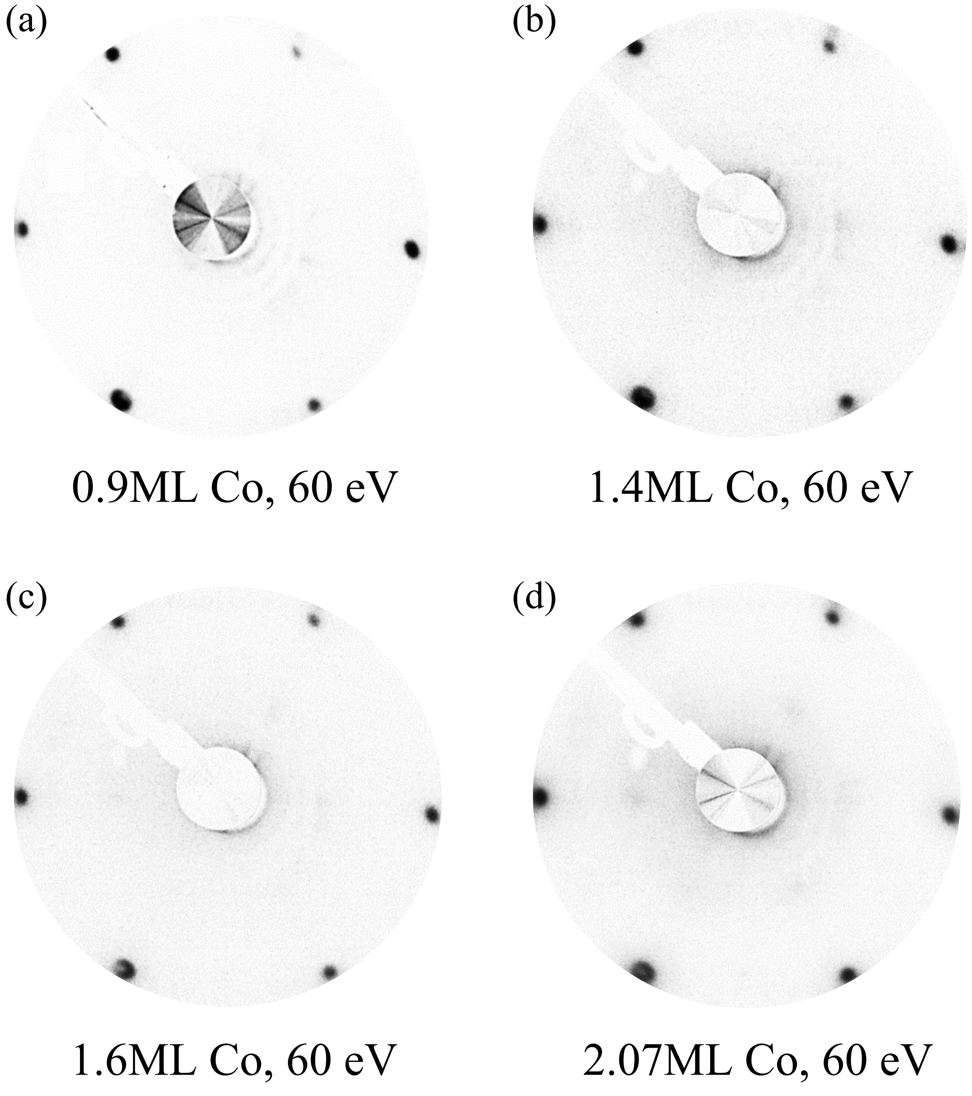

(a) 0.9ML Co, 60 eV

(b) 1.4ML Co, 60 eV

(c) 1.6ML Co, 60 eV

(d) 2.07ML Co, 60 eV

Figure 3.21: Selection of LEED patterns of (a) 0.9ML (b) 1.4 ML (c) 1.6 ML and (d) 2.07 ML of Co films grown on Ir(111). All images are taken at a primary electron energy of 60 eV.

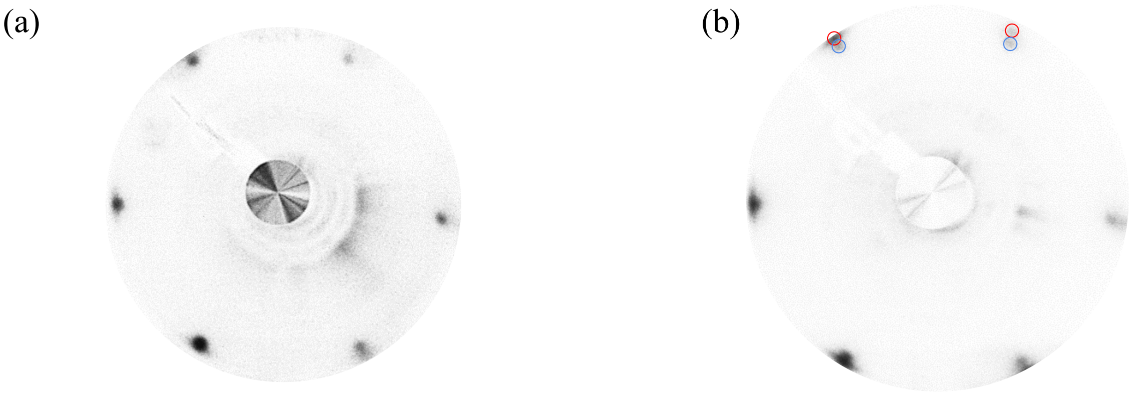

1ML Co/1ML Fe/Ir(111), 60 eV

2ML Co/1ML Fe/Ir(111), 60 eV

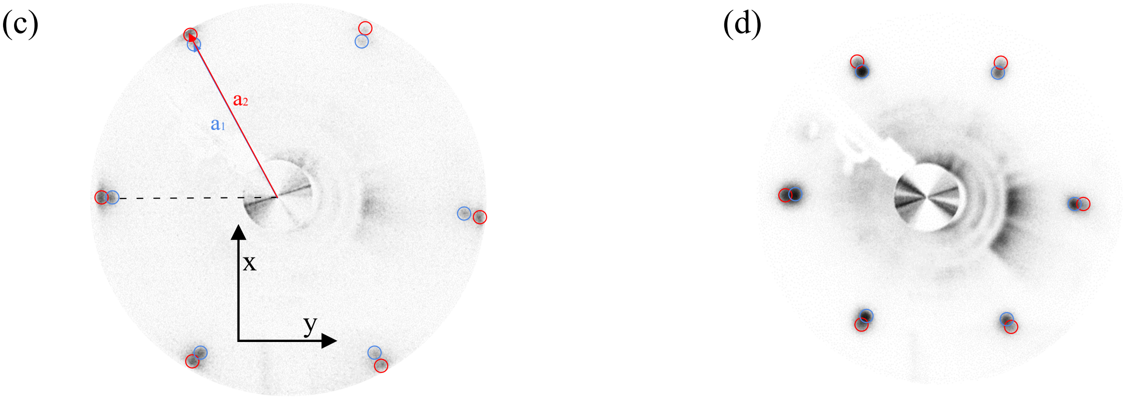

2ML Co/1ML Fe Annealed/Ir(111), 60 eV

2ML Co/1ML Fe Annealed/Ir(111), 86 eV

Figure 3.22: Selection of LEED patterns of (a) 1ML Co/1ML Fe, (b) 2ML Co/1ML Fe, (c) 2ML Co/1ML Fe Annealed/Ir(111) and (d) 2ML Co/1ML Fe Annealed grown on Ir(111). In (c) and (d) the Fe interface layer is annealed. Images (a)-(c) are taken at a primary electron energy of 60 eV and (d) at 86 eV.

4. Co/Fe multilayers on W(110)

In this chapter the results of the measurements performed on multilayer Co/Fe layers are presented and discussed. This chapter is divided into two main parts: symmetric Heisenberg exchange in section 4.1 and antisymmetric exchange (Dzyaloshinskii-Moriya interaction) in section 4.2. The notation used here will be the following: as an example, 2ML Co/1ML Fe/W(110) represents the case where 1ML Fe is grown on the W(110) substrate and 2ML of Co are grown on top.
In section 4.1.1 results obtained on the 1ML Co/1ML Fe/W(110) will be presented. In 2008 Zhang [112] performed measurements on a 2ML Fe/W(110) sample, this will be briefly introduced for comparison with the measurements in this work. In section 4.1.2 the results on 1ML Co/2ML Fe/W(110) system are presented. The probed magnon bands will be analyzed in order to quantify the exchange coupling in the layers. Section 4.2.1 will present the experimental data demonstrating the effect of the Dzyaloshinskii-Moriya interaction (DMI) on the magnon dispersion relation. Section 4.3 will discuss the magnon lifetimes in the 1ML Co/1ML Fe/W(110) system. The last section 4.4, will briefly summarize the results in this chapter.

4.1 Symmetric Heisenberg exchange

Up to now mainly elemental Fe on W(110) and Co on W(110) have been investigated by means of SPEELS [27, 104, 107, 112]. However in single elemental films, very often, only the $n = 0$ magnon mode is clearly visible and unambiguously identifiable in the experimental data. In order to probe the various magnetic interactions in ultrathin layered ferromagnetic films we investigate layered structures consisting of Co and Fe on the W(110) substrate. For example, by changing the top layer of a 2ML Fe/W(110) film to a different species, say Co, we should observe a sizable effect on the magnon dispersion since the intra ($J_{\parallel}$) and interlayer ($J_{\perp}$) exchange constants of the Fe and Co layer are expected to be different compared to those in a 2ML Fe/W(110) sample and therefore different magnon modes may be identified.

4.1.1 1ML Co/1ML Fe/W(110) system

In Fig. 4.1, SPEELS spectra obtained on a bilayer of 1ML Co/1ML Fe/W(110) are shown. The measurement is performed at Q = 0.3 Å^{-1} with a primary electron energy of
E_i = 4.2 eV. Fig. 4.1(a) shows the intensity of the scattered electron beam when the

incident beam consists of spin down polarized electrons (red triangles) and spin up polarized electrons (blue triangles). In the inset one can see the difference between the two

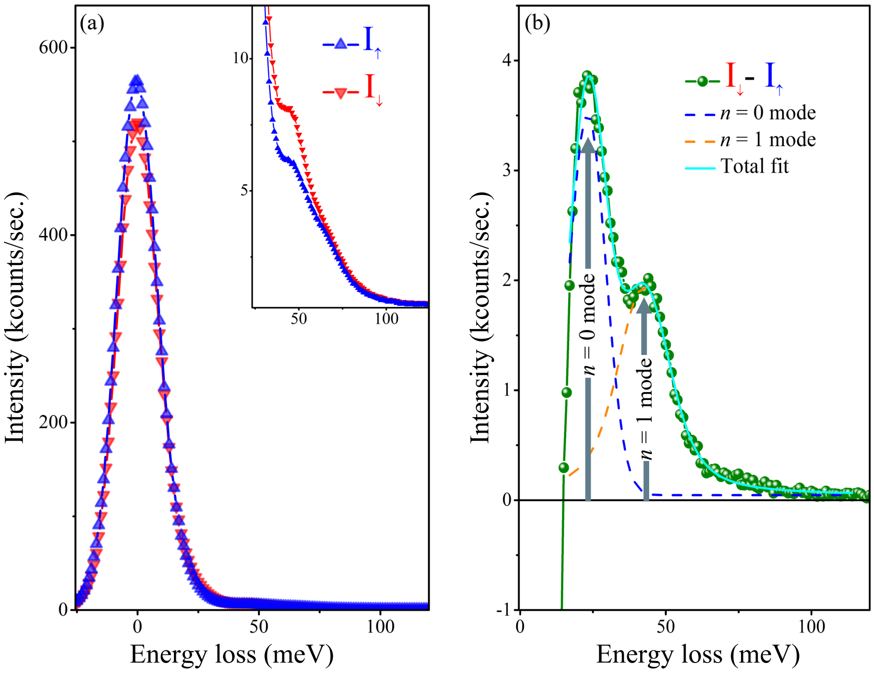

Figure 4.1: SPEEL spectra on a bilayer sample of Co/Fe/W(110) measured at Q = -0.3 Å^{-1}. The primary electron beam energy used was $E_i = 4.2$ eV with a FWHM resolution of 20 meV. (a) The intensity of the scattered electron beam when the incident beam has spin down polarized electrons (red triangles) and spin up polarized electrons (blue triangles). The inset shows a particular region of the intensity spectra where the magnon creation process takes place. (b) Difference (green spheres) of the two polarized beam intensities with two peaks clearly visible. The positions of these peaks correspond to the magnon excitation energies. The first peak is assigned the term $n = 0$ mode and the second peak is assigned to the $n = 1$ mode. The spectra are fitted with Voigt functions, where the $n = 0$ mode is seen as a blue dashed line, $n = 1$ mode is the orange dashed line and the cyan line is the total fit.

intensity spectra. This difference corresponds to a magnon creation and is represented in Fig. 4.1(b) where two peaks are clearly observed. These two peaks can be fitted by a convolution of a Gaussian and Lorentzian function or in other words a Voigt function. In the Voigt fit, the Lorentzian function is the natural line broadening and the Gaussian function represents the instrumental line broadening which was discussed in section 3.2. In the case presented in Fig. 4.1(b) the peak positions can already be unambiguously determined, even without a Voigt fit being performed, they correspond to the energy of the magnon excitation of the $n = 0$ mode and $n = 1$ mode in the magnon dispersion. In Fig. 4.1 it seems that the contribution of the Lorentzian linewidth to the first and second mode is much less than that of the Gaussian, which indicates that the broadening of the peak is mainly determined by the instrumental Gaussian broadening. Therefore qualitatively we can interpret the fit to give the positions of the magnon energy excitation positions but in the presence of multiple magnon modes it is difficult to get physical values from the linewidths. The $n = 0$ and $n = 1$ mode can be assigned to being mainly localized in the interface Fe and surface Co layer, respectively [109, 110]. By measuring the dispersion across the surface Brillouin zone (SBZ), the magnon dispersion can be obtained for both magnon modes. This is presented in Fig. 4.2 which shows experimentally obtained data

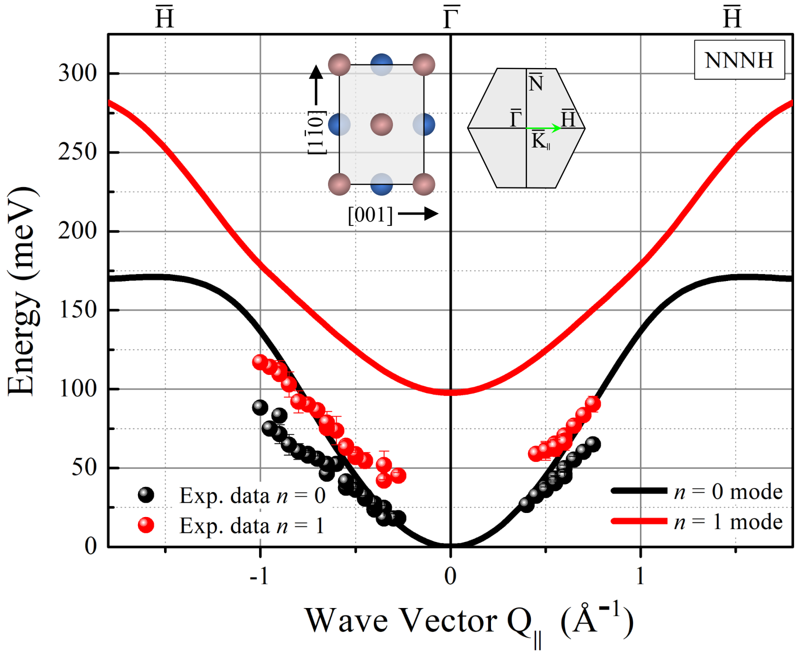

Figure 4.2: Experimentally obtained magnon dispersion on Co/Fe/W(110) bilayer. The black and red spheres represent the experimentally determined $n = 0$ and $n = 1$ mode, respectively. The calculated $n = 0$ and $n = 1$ modes in the Heisenberg model are represented by the black and red curves, respectively. The real space of the 2ML bcc(110) surface is shown along with a SBZ with the magnon propagation direction shown. The exchange coupling constants used for the fit with experimental data are: $J^1_{N\|}$=7.6 meV, $J^1_{NN\|}$=4.6 meV, $J^1_{N\perp}$=7.6 meV, $J^2_{N\|}$=14.8 meV, $J^2_{NN\|}$=0 and $J^2_{N\perp}$=7.6 meV. The subscripts for the exchange constants represent the intraplane exchange coupling $J^1_{N\|}$ and $J^1_{NN\|}$ in the nearest neighbor model (NNH) and the next nearest neighbor model (NNNH) in the interface Fe layer (1st layer). $J^1_{N\perp}$ is the interplane exchange coupling between the Fe interface layer (1st layer) and the Co layer (2nd layer). $J^2_{N\|}$, $J^2_{NN\|}$ and $J^2_{N\perp}$ represent the exchange coupling constants in the second layer. The exchange coupling constant values are taken from [27, 112].

on the 1ML Co/1ML Fe/W(110) bilayer sample measured at various wave vectors across the SBZ. The black spheres are the $n = 0$ mode magnons and the red spheres are the $n = 1$ mode magnons, determined in the same way as that of Fig. 4.1.

The magnon dispersion relation was calculated based on the Heisenberg model. In the first attempt at extracting exchange coupling values from the experimental data we use the following exchange constants: $J^1_{N\|}$=7.6 meV, $J^1_{NN\|}$=4.6 meV, $J^1_{N\perp}$=7.6 meV corresponding to the interface Fe layer (1st layer) and $J^2_{N\|}$=14.8 meV, $J^2_{NN\|}$=0 meV and $J^2_{N\perp}$=7.6 meV corresponding to the surface Co layer. The exchange coupling constants used for the Fe interface layer were taken after [112]. The exchange coupling constants used for the Co surface layer were taken after [27]. It is worth noting that the interlayer exchange coupling constants $J^1_{N\perp}$ and $J^2_{N\perp}$, in a 2 ML system for example, have to be the same value because of the symmetric nature of the Heisenberg exchange interaction, therefore we refer to both values as $J_{N\perp}$. In Fig. 4.2 we see that the discrepancy between the experimental data and the calculated fit is large. This can be attributed to a few different reasons. First, we have assumed so far that the exchange coupling constants $J^1_{N\parallel} = 7.6$ meV and $J^1_{NN\parallel} = 4.6$ meV in the interface Fe layer have the same strength as those in the interface Fe layer from the 2ML Fe/W(110) system. This is likely not true because in this work the top Fe layer has been replaced with the Co monolayer which causes a change in the electronic states in the Fe and Co layer and therefore would alter the exchange constants as well. This can be even more complex due to the fact that Co does not grow pseudomorphically on the 1ML Fe/W(110)(see section 3.4.1) but in the Nishiyama–Wassermann growth (see chapter 3, section 3.4.1, Fig. 3.16). The symmetry of the film remains the same as that of the original C_{2v} group. Given that the interlayer and intralayer atomic distances change due to this top monolayer replacement, one would expect a change in the exchange coupling constants as well [14]. The second reason for the calculated dispersion having a large discrepancy from the experimental data in Fig. 4.2 is due to the assumption that the interlayer coupling $J_{N\perp} = 7.6$ meV between the interface Fe layer and the Co layer is assumed to be the same as the intralayer exchange coupling of the Fe interface layer. The value for this interface Fe exchange coupling has been taken from the works of Zhang [112]. The third reason for the discrepancy is the fact that the exchange coupling $J^2_{N\parallel} = 14.8$ meV in the Co layer is taken from the values obtained on a 2.5-8ML Co/W(110) system [28]. Overall the observation of experimental data points to the fact that the exchange constants cannot be assumed to be the same as they are determined on elemental films. This points to a much more complex state in the system and a change in the electronic states.

We may alternatively start by assuming 1ML Fe/W(110) exchange coupling constants: $J_{N\parallel} = 3.2$ meV and $J_{N\parallel} = 0.6\ J_{NN\parallel}$ found in [70]. The next nearest neighbor constants are fixed relative to the nearest neighbor ones in order to reduce the number of fitting paramters which is the same approach taken in [112] for the 2ML Fe/W(110). Results obtained on the 1MLCo/1ML Fe/W(110) are plotted in Fig. 4.3. The exchange constants for Co thin film used in the previous fit in Fig. 4.2 were kept nearly the same. It is obvious that the calculated dispersion relation (red curve) does not match the experimental data (red spheres) for the $n = 1$ mode. Although the $n = 0$ mode (black curve) shows good agreement with the experimental data (black spheres), one has to look at the interlayer exchange constants that are implied to see that the ML exchange coupling constants cannot describe the experimental data. Since the value of the intralayer exchange constant in the 1ML Fe/W(110) is small, $J_{N\parallel} = 3.2$ eV, the $n = 0$ band is very soft and in order to for the band to describe the experimental data well this implied then a very strong inter-

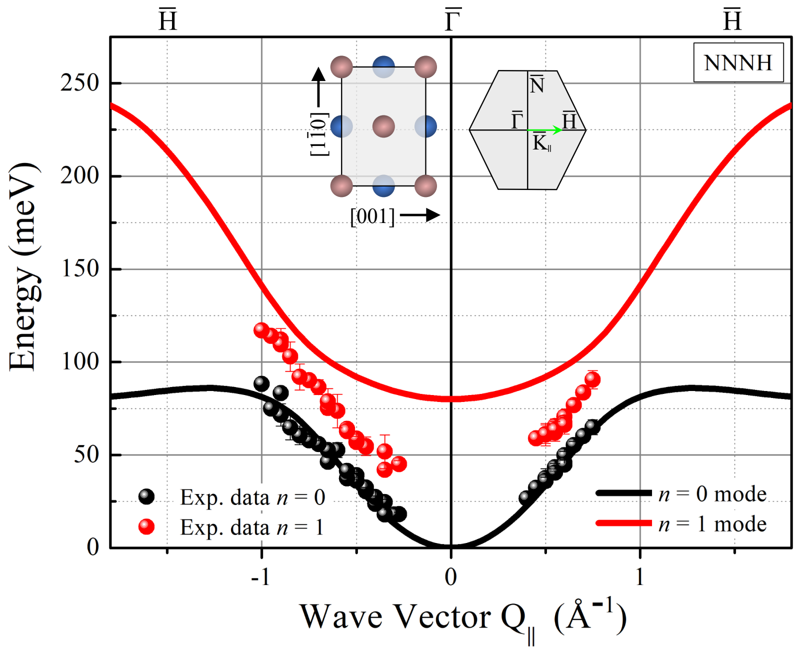

Figure 4.3: Experimentally obtained magnon dispersion in Co/Fe/W(110) bilayer. The black and red spheres represent the experimentally determined $n = 0$ and $n = 1$ mode dispersion, respectively. The calculated $n = 0$ and $n = 1$ modes in the Heisenberg model are represented by the black and red curves, respectively. The real space of the 2ML bcc(110) surface is shown along with a SBZ with the magnon propagation direction shown. The exchange coupling constants used for the fit with experimental data are: $J^1_{N\|}$=3.2 meV, $J^1_{NN\|}$=1.92 meV, $J^1_{N\perp}$=13.5 meV, $J^2_{N\|}$=12 meV, $J^2_{NN\|}$=0.5 and $J^2_{N\perp}$=13.5 meV.The exchange coupling constants are taken from [27, 112].

layer exchange coupling. The value that is used is at least $J_{N\perp} = 11.5$ meV which is very large and is unreasonable since the $n = 1$ band (red) becomes hugely overestimated to the experimental data (red spheres). The statement that these values are overestimated can be applied since the $n = 1$ mode is unambiguously determined from the raw experimental data as shown in Fig. 4.1.

Alternatively, the data presented in Fig. 4.2 and 4.3 has been refitted with different exchange coupling constants in the next nearest neighbor Heisenberg model and presented in Fig. 4.4. Observing the data and the calculated dispersion it is evident that the calculated dispersion relation agrees very well with the experimental findings. The interlayer exchange coupling constants for $n = 0$ mode were $J^1_{N\|} = 5.6$ meV, $J^1_{NN\|} = 3.4$ meV, $J^1_{N\perp} = 4.5$ meV. The intralayer exchange coupling constants for the Co layer corresponding to the $n = 1$ mode were $J^2_{N\|} = 12$ meV, $J^2_{NN\|} = 0.5$ meV and $J^2_{N\perp} = 4.5$ meV. In order to compare and discuss our results in the context of other systems we first introduce the measurements on 2ML Fe/W(110).

In 2008 SPEELS measurements by Zhang [112], experiments were performed on a 2ML Fe/W(110) sample, the magnon dispersion in the 2ML Fe/W(110) is presented in Fig. 4.5 The dispersion curve calculations in Fig. 4.5 were done for a 2ML bcc(110) film. The

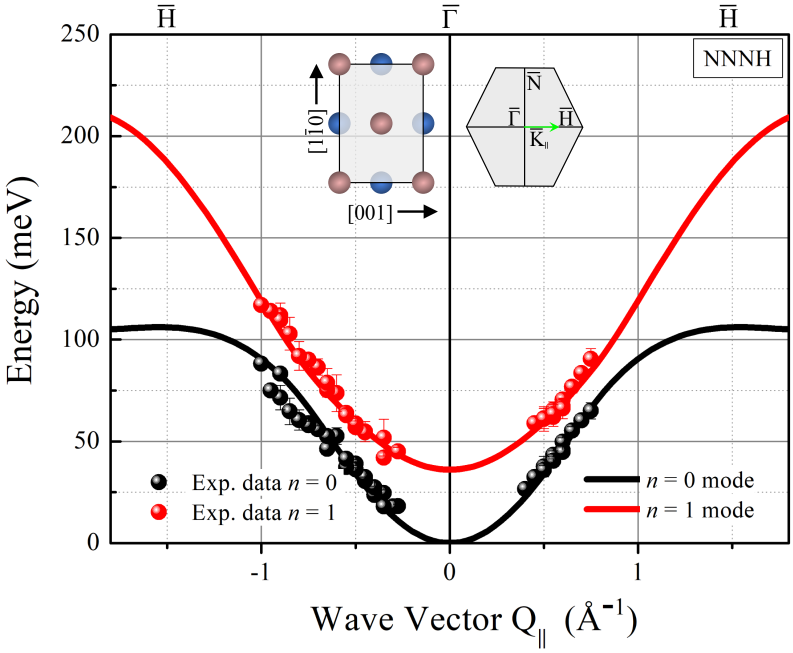

Figure 4.4: Experimentally obtained magnon dispersion in 1ML Co/1ML Fe/W(110) bilayer. The black and red spheres represent the experimentally determined $n = 0$ and $n = 1$ mode, respectively. The calculated $n = 0$ and $n = 1$ modes in the next nearest neighbor Heisenberg model are represented by the black and red curves, respectively. The real space of the 2ML bcc(110) surface is shown along with the SBZ with the magnon propagation direction shown. The exchange coupling constants used for the fit with experimental data are: $J^1_{N\|}$=5.6 meV, $J^1_{NN\|}$=3.4 meV, $J^1_{N\perp}$=4.5 meV, $J^2_{N\|}$=12 meV, $J^2_{NN\|}$=0.5 meV and $J^2_{N\perp}$=4.5 meV.

SPEELS spectra showed one pronounced peak assumed to be mainly the $n = 0$ mode of the magnons. It was found that the experimental data could not be well described by the NNH model since above $\Delta\mathrm{K} = 1.0$ Å^{-1} there is a large discrepancy between the experimental data points and the calculated dispersion relation. It was observed that in order to describe the magnon dispersion well, the NNNH needed to be implemented where the exchange constants used were $J_N S = 7.6$ meV and $J_{NN}S = 0.6(J_N S) = 4.6$ meV. It is pointed out that the Heisenberg model is an estimation only since it is simplified model that assumes a free standing film and does not take into account the substrate. Therefore it is argued based on STM and Monte Carlo simulations that the assumption of the interlayer exchange constants being equivalent to the intralayer exchange constants is not strictly valid. This was later shown to be the case in Ref. [110].

In this context the results obtained on the 1ML Co/1ML Fe/W(110) are surprising in a few different ways. First we notice that the nearest neighbor (NN) exchange coupling constant in the interface Fe layer $J^1_{N\|} = 5.6$ meV is substantially lower than the one obtained in the 2ML Fe/W(110) sample. The reduction in the exchange constant value is 27% and may be attributed to the hybridization not only with the W(110) substrate but also due to the Co topmost layer which as discussed above gives rise to different inter and

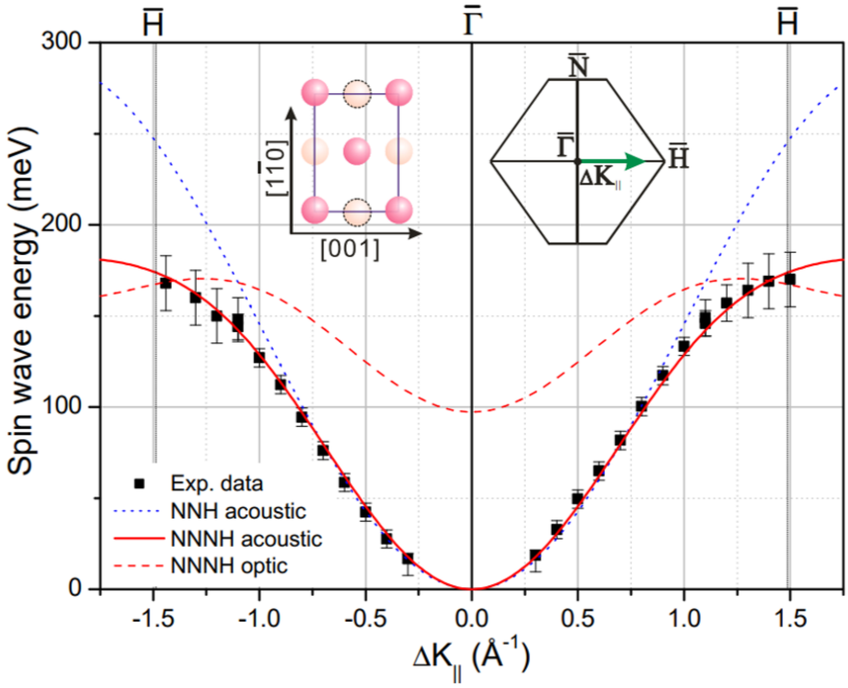

Figure 4.5: Magnon dispersion in a 2ML Fe/W(110). The experimental data is represented by black squares, the blue dotted curve represents the calculated dispersion in the NNH model, the red dashed curve and solid cure is the calculation for the $n = 1$ and $n = 0$ mode dispersion in the NNNH model, respectively. The exchange constant parameters for the $n = 0$ mode in the NNH model (blue dotted curve) are $J_{N\|}S = 12$ meV. The exchange constants fitting parameters for the $n = 0$ and $n = 1$ mode in the NNNH model (red solid and dashed curve) are $J_{N\|}S = 7.6$ meV and $J_{NN\|}S = 4.6$ meV, respectively. The real space lattice structure is shown where the magenta balls are the atoms in the first layer and the yellow balls are the atoms in the second layer. The surface structure in reciprocal space is shown as well. Figure from [112].

intralayer distances when compared to the 2ML Fe/W(110) film. The 3d electronic states of the Fe film can hybridize with those of Co and the W(110) substrate which leads to the lower exchange coupling constants [110]. The next nearest neighbor exchange constant in the interface Fe layer $J^1_{NN\|} = 3.4$ meV was set to 60% of $J^1_{N\|}$. This agrees very well with the experimental data and previous experimental investigations [112] where the next nearest neighbor interactions were not negligible but had a significant role in the magnon dispersion relation. The exchange coupling constants obtained for the second layer, that is Co, were $J^2_{N\|} = 12$ meV and $J^2_{NN\|} = 0.5$ meV. This agrees well with studies in elemental Co films on W(110) where the obtained exchange coupling constants $J^2_{N\|} = 14.8$ meV and $J^2_{NN\|} = 0$ meV. In our 1ML Co/1ML Fe/W(110) system the interface Fe layer has a significant NNNH contribution to the magnon dispersion and the top Co layer has very small or even negligible NNNH contribution to the magnon dispersion. The surprising finding is that the interlayer coupling $J^1_{N\perp}$ and $J^2_{N\perp}$ seems to be very low compared to the values obtained on elemental Fe on W(110) and Co on W(110), henceforth referred to as simply

Table 4.1: The Heisenberg exchange coupling constants obtained from the fitting of experimental data with the Heisenberg model for nearest (N) and next nearest (NN) in the 1ML and 2ML Fe/W(110). Experimentally obtained values are shown for a 1ML Fe/W(110) measured at T=120K and 2ML Fe/W(110) measured at T=300K. The values are given in meV and the spin magnetic moment S is set to 1. Calculations using different approaches are given for comparison.

Method and Sample	J_{Nin}(meV)	J_{Nout}(meV)	J_{NNin}(meV)
Exp. (120K) 1ML Fe/W(110) Ref[112]	3.2±0.6	-	1.9±0.4
Exp. (300K) 2ML Fe/W(110) Ref[112]	12±0.5	12±0.5	-
Exp. (300K) 2ML Fe/W(110) Ref[112]	7.6±0.5	7.6±0.5	4.6±0.3
Exp. (300K) 2ML Fe/W(110) Ref[92]	6.1±1	11±1	3.7±0.6
2ML Fe *ab initio* calculation Ref[14]	7.3	12.7	-
2ML Fe *ab initio* calculation Ref[4]	6.1	6.6	-
Exp. (300K) 1ML Co/1ML Fe/W(110)(Fe^1)	5.6±1	4.5±1	3.4±0.6
Exp. (300K) 1ML Co/1ML Fe/W(110)(Co^1)	12±1	4.5±1	0.5 ±0.2

$J_{N\perp}$. The value obtained in this work is $J_{N\perp} = 4.5$ meV which is 41% lower than the value reported in [112] for 2ML Fe/W(110) and 70% lower than the value reported in [28] for 2.5 ML - 8 ML Co/W(110). This points to a strong renormalization of the electronic states of the Fe-Co interface. In Tab. 4.1, a summary of experimental and theoretical calculation results on Fe ultrathin films on W(110) is given along with the experimentally derived exchange coupling constants for 1ML Co/1ML Fe/W(110). From Tab. 4.1 we can see that the obtained exchange coupling constants for the interface Fe layer in this work on the 1ML Co/1ML Fe/W(110) are between those of the 1ML Fe/W(110) and 2ML Fe/W(110). This points to two conclusions. First, in the 1ML Fe/W(110) case the Fe monolayer hybridizes with the W(110) substrate. In a 2ML Fe/W(110) system, the interface Fe layer hybridizes with the W(110) substrate and with the above Fe layer. Between the 1ML Fe and 2ML Fe on the W(110) system one would expect a reduction in the exchange coupling constants and a lower magnon band stiffness for the 1ML Fe sample having its origin in the reduction of neighbor interactions, possible temperature effects and the DMI [104, 106]. Second, in this work the interface Fe layer in the 1ML Co/1ML Fe/W(110) hybridizes with the W(110) substrate and has its electronic structure modified by the Co layer on top as discussed above. This softens the $n = 0$ mode considerably when compared to the 2ML Fe/W(110) sample and gives the value of exchange coupling constants for the Fe interface $J_{\text{1ML Fe}} < J_{\text{1ML Co/1ML Fe}} < J_{\text{2ML Fe}}$. Third, it is very interesting that the exchange constants of the Co layer giving rise to the $n = 1$ magnon mode have a comparable energy at the zone boundary when compared to the 2ML Fe/W(110) (see Fig. 4.4 and Fig. 4.5. The amplification of the Fe monolayer intralayer exchange constants in the 1ML Co/1ML Fe/W(110) interface compared to the 1ML Fe/W(110) system is due to the added Co layer on top. The increase in the $J_{N\parallel}$ is by a factor of nearly 1.8. This implies that this is a Co mediated exchange enhancement of the interface Fe layer exchange coupling. Interestingly, in SPEELS experiments performed on 3ML Co/Ir(001) in [13], the top Co intralayer exchange couplings have the same value as the ones derived here. In the same paper, the top Co intralayer exchange couplings in 3ML Co/Cu(001) and 3ML Co/Pt(111) were derived to be 18 and 8 meV, respectively. This points to the general trend that the intralayer exchange constants in Co films are higher than in the Fe elemental films [110], which is what is observed in our case as well.

4.1.2 1ML Co/2ML Fe/W(110) system

In order to have a more clear picture of the interfacial exchange constants in the Fe layer next to the W(110) in 1ML Co/1ML Fe/W(110) as well as the interlayer coupling between Fe and Co, measurements were performed on trilayer structures consisting of Co and Fe on W(110). The results shall also help us confirm that the observed small interlayer coupling between Fe and Co layers, discussed in the previous section, is general. We present the case of 1ML Co/2ML Fe/W(110) in Fig. 4.6. The notation in this section that is used also in Fig. 4.6 and Tab. 4.2 is defined as follows. For example, $J^{2}_{N\parallel}$ corresponds to the intralayer nearest neighbor exchange coupling in the second layer, hence the superscript 2. When we write Fe^{2} this corresponds to the Fe layer number 2, counted from the bottom. In the case that $J^{1,2}_{N\perp}$ is written, this means the interlayer coupling between layer 1 and layer 2. In Tab. 4.2 some $J_{\perp}$ exchange constants are written in the $J_{\perp\mathrm{Fe}}/J_{\perp\mathrm{Co}}$ format, this means that the layer under discussion is coupled with a $J_{\perp\mathrm{Fe}}$ value to an Fe layer on one side and to a $J_{\perp\mathrm{Co}}$ on the other side.

From Fig. 4.6 we can immediately realize that the interface Fe layer has substantially higher intralayer nearest neighbor coupling , $J_{N\parallel} = 14.7$ meV. This is an increase by nearly a factor of 2.6 over the interface Fe $J_{N\parallel}$ exchange coupling in the 1ML Co/1ML Fe/W(110) case which we will refer to as the bilayer sample from now on. This observation is somewhat surprising since the immediate environment of the double system was not changed but only a third layer consisting of Co was added on top. This would suggest that the third layer is correlated to the second layer which would in turn affect the interface layer. It is worth pointing out that the value of $J_{N\parallel} = 14.7$ meV for the interface Fe layer is nearly factor of 2 higher than the value of $J_{N\parallel}$ in the 2ML Fe/W(110) reported in [112]. The influence of the next nearest neighbor is enhanced in the interface Fe layer for the trilayer structure, with the ratio of $J_{N\parallel}$ to $J_{NN\parallel}$ being 0.6, which points to the fact that these interactions cannot be ignored in our calculations. This ratio between the nearest and next nearest neighbor in Fe films is the same one used previously in [65, 112]. The $J_{N\perp}$ interlayer coupling of the middle Fe layer to the top Co layer was found to be 4.5 meV which is the same value that is observed for the coupling between the interface Fe and the top Co layer in the 1ML Co/1ML Fe/W(110) system. This is a very weak coupling effect between the Fe and Co layers and is seen to be a common feature in the

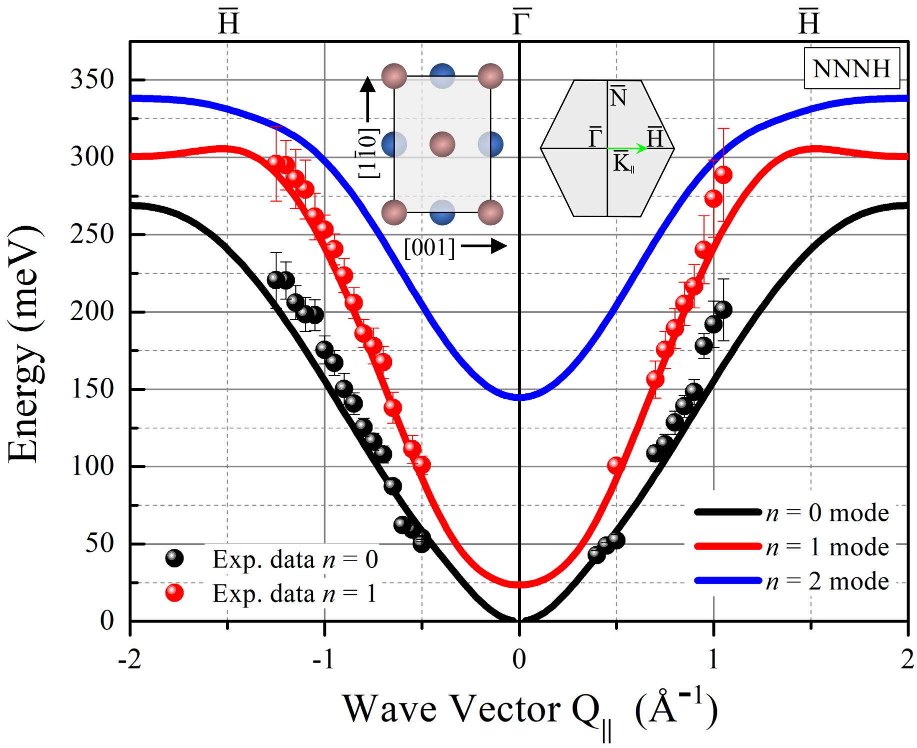

Figure 4.6: Experimentally obtained magnon dispersion in 1ML Co/2ML Fe/W(110). The calculated dispersion curves in the NNNH are represented by the black, red and blue lines corresponding to the $n = 0$, $n = 1$ mode and $n = 2$ mode, respectively. The exchange coupling constants used for the fit with the data are $J^3_{N\|} = 16$ meV, $J^3_{NN\|} = 1.0$ corresponding to the values in the Co top layer which is labeled as layer 3 and appears as a superscript, $J^{3,2}_{N\perp} = 4.5$ meV between the top Co layer and the middle Fe layer. For the $n = 1$ mode for which the exchange coupling constants were taken from the interface Fe layer, the exchange coupling constants are $J^2_{N\|} = 14.7$ meV, $J^2_{NN\|} = 0.6J^2_{N\|}$, $J^{1,2}_{N\perp} = 14.7$, $J^{1,2}_{N\perp} = 0.6J^{1,2}_{NN\perp}$ between Fe$_1$ and Fe$_2$. For the $n = 2$ mode, the exchange coupling constants used are from the middle Fe$_2$ layer, $J^2_{N\|} = 15.5$, $J^2_{N\|} = 0.6J^2_{NN\|}$. The black and red spheres correspond to experimental data for the $n = 0$ and the $n = 1$ mode, respectively.

two systems so far investigated. For the 1ML Co/2ML Fe/W(110), the results indicate that the Co layer on top of Fe meditates the enhancement of the Fe intralayer coupling and couples only weakly to the Fe layers. The next nearest interlayer coupling $J_{NN\perp}$ between Co and Fe layers was neglected, this is in agreement with previous studies on Co films. Another effect that may be taking place is the intermixing of some parts of the films. If patches of Fe and Co were to intermix then the exchange constants between two layers would be similar. This is the case where the Co intralayer $J_{N\|} = 16$ meV and $J_{N\|}$ for the middle Fe layer is 15.5 meV, the other components of the exchange constants however are different. As a result, while there may be some partial intermixing going on but because the exchange constants are in the end different, this is not a significant effect. We should point out that in the case a trilayer, three magnon modes should be observed as discussed in section 2.1.1 however experimentally it is challenging. For example in the case of 1ML Co/2ML Fe/W(110) there should be 3 magnon modes observed. The $n = 2$ mode will be at substantially higher energies and low intensities in the SPEELS spectra due to the short lifetime and therefore broad natural linewidth. These higher magnon modes decay more into Stoner states (for an example see section 2.1.2, Fig. 2.7). Therefore the $n = 2$ magnon mode could not be well resolved.

Interestingly, in this system the $n = 0$ magnon mode was assigned as being mainly originating from the Co layer which is the surface layer. This is due to the fact that the interlayer coupling between the Co and the middle Fe layer is very weak while the interface Fe layer has a large interlayer coupling to the middle Fe layer. Also, the intralayer interface Fe layer coupling is enhanced by both the middle Fe layer and the Co surface layer. This enhancement was observed when adding an Fe monolayer on top of the 1ML Fe/W(110) [110] and when adding a Co monolayer on top of the 1ML Fe/W(110). All of the findings on the 1ML Co/1ML Fe/W(110) and 1ML Fe/2ML Co/W(110) are summarized in Tab. 4.2 in section 4.4, with the notation explained in the table as well as the text. The overall picture of the trilayer structures needs to be completed. Ideally, all three modes would be well resolved in 1ML Co/2ML Fe/W(110) in order to better quantify the exchange interaction in these systems.

4.2 Antisymmetric exchange (Dzyaloshinskii-Moriya interaction)

4.2.1 1ML Co/1ML Fe/W(110) system

In section 2.2 we introduced the antisymmetric Dzyaloshinskii-Moriya exhcnage interaction (DMI). In the same section, it was pointed out that in 2010, for the first time our group quantified the DM vectors (D_{ij}) [104]. In that experiment by means of SPEELS a 2ML Fe/W(110) sample was investigated where the interfacial DMI was observed. There are two ways that one can investigate the interfacial DMI effect in an ultrathin metallic film using SPEELS. The first way involves changing the scattering geometry. This is where a particular wave vector is measured and then the sample is rotated to a scattering geometry that would allow for the measuring of the opposite but equal wave vector. The experiment is performed in a magnetically remanent state. If the DMI is pronounced then there will be a energy splitting $\Delta\mathrm{E}$ as explained in section 2.2.1 i.e. $\mathrm{E}_{\mathbf{M}}(\mathrm{Q}) \neq \mathrm{E}_{\mathbf{M}}(-\mathrm{Q})$. The second way to investigate the DMI effect is to perform a time inversion experiment. This is where a scattering experiment is performed at a particular wave vector while the sample is in a magnetically remanent state following which the magnetization of the sample is flipped to the opposite crystollographic direction and the same wave vector is measured. If the DMI is pronounced then one should again observe an energy splitting $\mathrm{E}_{\mathbf{M}}(\mathrm{Q}) \neq \mathrm{E}_{-\mathbf{M}}(\mathrm{Q})$. Also this would give conclusive proof that the energy splitting is of magnetic origin. Since the SPEELS experiment is highly sensitive to the electron scattering intensity, the time inversion experiment is the most proper way to investigate the DMI in ultrathin films. Zakeri showed in [104] however, that both the scattering geometry and the time inversion experiment give the same result when done carefully. In this work for best results, the time inversion experiment is done.

An Fe double layer on W(110) exhibits a perfect C_{2v} symmetry [93, 111], where the DM vectors D_{ij} can point in any inplane direction making it an excellent candiate for exotic spin structures such as antiskyrmions [42]. DMI in this system is an interfacial effect mediated by the W atoms. The Fe layers are directly exchanged coupled to each other. This exchange coupling is of both symmetric and antisymmetric nature. Hence the effective DMI in such a system is an overall effect of the intralayer DMI, describing the antisymmetric coupling of the Fe atoms in each layer, as well as the direct interlayer DMI, describing the antisymmetric coupling of Fe atoms sitting in different layers. Since the DMI is an interfacial effect here, the pattern of intralayer DMI coupling strength is different in each layer. The effective DMI is an average over all the interactions, which is what is measured in the SPEELS experiment. In this work we replaced the topmost Fe layer with a Co layer which would in principle do two things: modify the DMI coupling strength in each layer and between the two layers. This is a reasonable assumption since as we saw from the above results the Heisenberg exchange constants were strongly modified by the replacement of the Fe layer with that of Co.

In Fig. 4.7, a series of SPEELS spectra obtained on a 1ML Co/1ML Fe/W(110) is presented where a series of wave vectors have been measured in a time reversal experiment, as discussed above. The spectra are fitted with a Voigt function and as apparent from Fig. 4.7, the $n = 0$ magnon mode energy can be unambiguously extracted since the peak in the difference spectra has a narrow linewidth and is therefore well defined. The sensitivity of confined magnon modes depends on the incident electron beam energy E_i, therefore the energy was chosen such that the $n = 0$ mode is most pronounced which would allow for a well defined study of the interfacial DMI. The magnon excitation energy can be extracted and compared for two equal but crystollograpically opposite wave vectors shown in
Fig. 4.7. The energy splitting $\Delta E = E_{\mathbf{M}}(Q) \neq E_{-\mathbf{M}}(Q)$ that is expected can be fitted with the DMI energy dispersion introduced in section 2.2.1 and shown in Fig. 2.10. The results are shown in Fig. 4.8 where they are compared to those obtained on a double layer Fe on W(110) obtained earlier in our group [104].

By looking at Fig. 4.8 we can immediately see that the DMI energies are much larger than those reported in [104]. In this figure, the atoms of the interface and surface layer are represented by blue and light blue color, respectively. For each layer we consider two DMI vectors describing the intralayer coupling. These are nearest and next nearest neighbor DMI vectors and are represented by $D_{1\parallel}$ and $D_{2\parallel}$, respectively. For the coupling between the layers we consider only the nearest neighbor DMI vector $D_{1\perp}$ since the interlayer next nearest neighbor should have no contribution to the DMI energy in the bcc(110) surface. In the interface layer $D_{1\parallel}$ and $D_{2\parallel}$ are shown by dark-blue and black arrows, respectively. In the surface layer these interactions are shown by light-blue and gray arrows, respec-

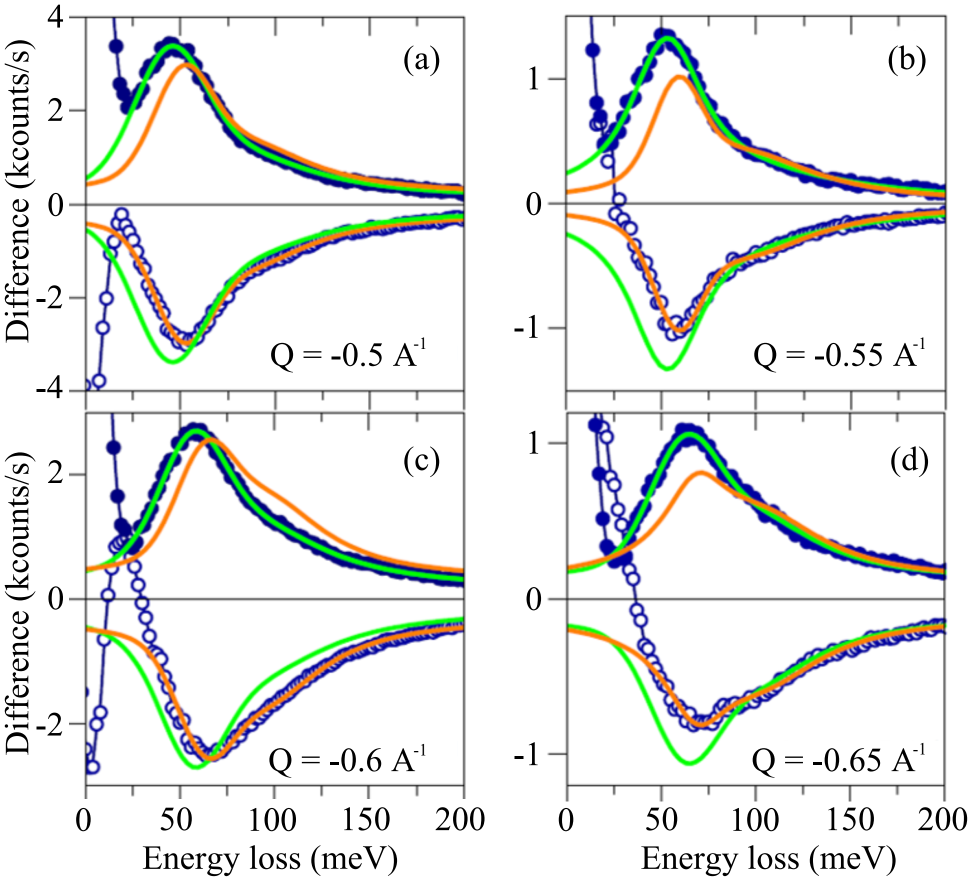

Figure 4.7: Series of difference spectra recorded for different wavevectors on the 1ML Co/1 ML Fe bilayer on W(110). The spectra are recorded for two cases; $\mathbf{M}\|[\bar{1}10]$ (solid circles) and $\mathbf{M}\|[1\bar{1}0]$ (open circles). The solid lines are the fits to the experimental spectra. In order to easily compare the spectra with different magnetization directions, the same fits are shown when they are mirrored with respect to the horizontal axis. Figure courtesy of Zakeri [93].

tively. The green arrows represent the interlayer DMI $D_{1\perp}$. The longitudinal component of the DM vectors is obtained from the SPEELS measurements. Performing analysis on the SPEELS spectra obtained from the Fe double layer grown on W(110) shows the results presented in Fig. 4.8(a) as the solid red line. Considering this system and the geometry arguments from Eq. 2.35, the DMI energy asymmetry for the bcc(110) system can be expressed as

$$\Delta \mathrm{E} = \mathrm{E}_{DM}(\mathrm{Q}_{\|}) - \mathrm{E}_{DM}(-\mathrm{Q}_{\|}) = 4\left[\left(2\mathcal{D}^{x}_{1\|} + \mathcal{D}^{x}_{1\perp}\right)\sin\left(\frac{\mathrm{Q}_{\|}a}{2}\right) + \mathcal{D}^{x}_{2\|}\sin(\mathrm{Q}_{\|}a)\right], \quad (4.1)$$

where $\mathcal{D}^{x}_{1\|} = \frac{1}{2}(D^{x}_{1\|}\lfloor_{layer\,1} + D^{x}_{1\|}\lfloor_{layer\,2})$ and $\mathcal{D}^{x}_{2\|} = \frac{1}{2}(D^{x}_{2\|}\lfloor_{layer\,1} + D^{x}_{2\|}\lfloor_{layer\,2})$ represent the average nearest and next nearest neighbor intralayer DMI of the two layers, Fe in this case, respectively. $\mathcal{D}^{x}_{1\perp} = D^{x}_{1\perp}$ since there is only one interlayer interaction. The superscript x represents the longitudinal component of the DM vectors. This notation is used because for the 2ML Fe/W(110), the individual Fe layers are not uniquely distinguished. The val-

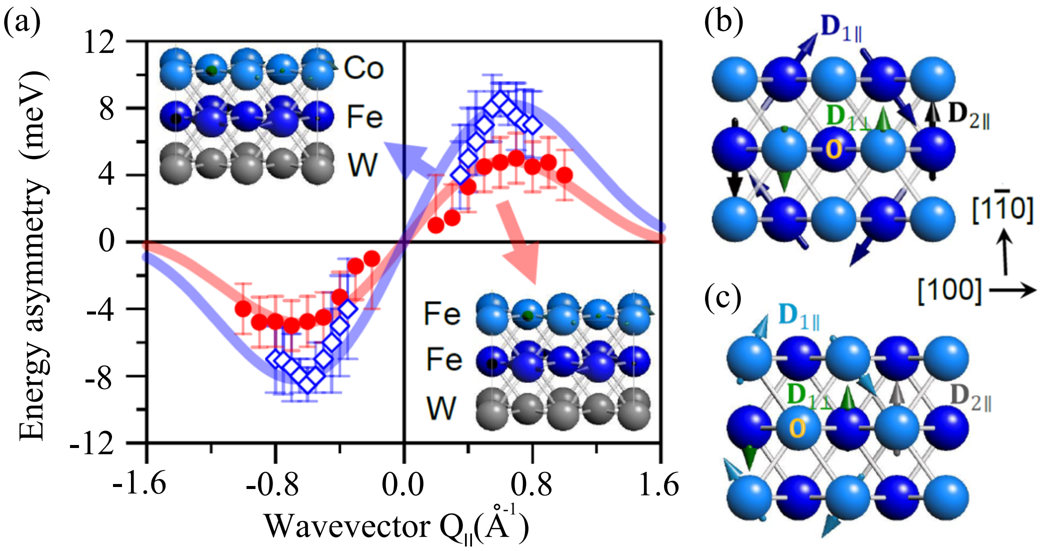

Figure 4.8: (a) The energy asymmetry ΔE(Q) of the $n = 0$ magnon mode measured in 1ML Co/1ML Fe/W(110) and compared to the one of 2ML Fe/W(110) taken from [104]. ΔE(Q) is measured by recording the spectra at a fixed Q and by reversing the direction of M. The side view of the investigated structures is shown as the inset. The atomistic DM vectors D_{ij} in the interface (b) and surface (c) layer, as seen from the top view. The nearest neighbor intralayer interaction in each layer is denoted by $D_{1\parallel}$ and the next nearest neighbor one is shown by $D_{2\parallel}$. The nearest neighbor interlayer DMI is represented by $D_{1\perp}$. The origin site is the one marked with O. In the C_{2v} symmetry the D_{ij} lie in the plane but their direction is not determined. Figure courtesy of Zakeri [93].

ues obtained from the analysis of the 2ML Fe/W(110) data in Fig. 4.8 are $2\mathcal{D}^x_{1\parallel} + \mathcal{D}^x_{1\perp} = 0.9(3)$ meV and $D^x_{2\parallel} = 0.5(3)$ meV [104]. At the time of the work referenced, these were the largest value of atomistic DM vectors D_{DMI} that were reported. In this work we replaced the top Fe layer with a Co layer which would change the electronic structure of the system. Also, the symmetry of the system is lowered due to the fact that Co monolayer grows on the Fe monolayer on W(110) with the Nishiyama-Wassermann growth relationship which would mean that the hexagonal base Co(0001) plane is parallel to W(110), and Co$[11\bar{2}0]$ is the parallel direction to W[001] direction. The atomic arrangement of such a surface is somewhat between the one of a bcc(110) and an hcp(0001) surface [32, 69]. In Fig. 4.8 the results of DMI asymmetry energy ΔE for the 1ML Co/1ML Fe bilayer on W(110) are presented, together with those of the 2ML Fe on the same substrate. The experimental data is fitted with Eq.(4.1), this results in the values of $2\mathcal{D}^x_{1\parallel} + \mathcal{D}^x_{1\perp} = 1.65 \pm 0.3$ meV and $D^x_{2\parallel} = 0.75 \pm 0.3$ meV. Comparing these values to those of the Fe double layer indicates that both the nearest and next nearest neighbor DMI are increased by a factor of about 1.8 and 1.5, respectively. Based on Eq.(2.34), we can imply that the magnitude of D_{ij} should be largest for the interfacial magnetic atoms because of the D_0 term which is proportional to the strength of SOC. This makes sense since in the case of ultrathin films on heavy substrates, the DMI is meditated by the SOC of the substrate atoms. Also, contrary to what was said about the Heisenberg exchange, namely that $J_{ij} = J_{ji}$, this is no longer the case for the antisymmetric exchange where $D_{ij} = -D_{ji}$. Therefore the sign of $D_{1\parallel}$ and $D_{2\parallel}$ in the interface layer is opposite to the sign of $D_{1\parallel}$ and $D_{2\parallel}$ in the surface layer [42]. By comparing the results from the 2ML Fe/W(110) and 1ML Co/1ML Fe/W(110) we can separate the contribution of each layer to $\mathcal{D}^x_{1\parallel}$, $\mathcal{D}^x_{1\perp}$ and $\mathcal{D}^x_{2\parallel}$ since the interface Fe layer remains unchanged. Analyzing the measured values of ΔE one realizes that the value of $\mathcal{D}^x_{2\parallel}$ is largely enhanced. This means that $D_{2\parallel}|_{Interface\,\mathrm{Fe}} + D_{2\parallel}|_{Surface\,\mathrm{Co}} > D_{2\parallel}|_{Interface\,\mathrm{Fe}} + D_{2\parallel}|_{Surface\,\mathrm{Fe}}$. From this it would appear that the norm of $D_{2\parallel}|_{Surface\,\mathrm{Co}}$ is larger than the norm of $D_{2\parallel}|_{Surface\,\mathrm{Fe}}$. However, as we already mentioned the sign of the DMI vectors is opposite in the surface and interface layers. Therefore, an enhancement in the $D_{2\parallel}$ is the result of the fact that the norm of $D_{2\parallel}|_{Surface\,\mathrm{Co}}$, which exhibits an opposite sign, is in fact smaller. This agrees with the finding that generally the strength of DMI vector in Co layers grown on W(110) is much smaller [27]. In summary the cancellation effect of the two layers is suppressed, when the top Fe layer is replaced with a Co layer and $\mathcal{D}^x_{2\parallel} = \frac{1}{2}D^x_{2\parallel}\lfloor_{layer\,1}+D^x_{2\parallel}\lfloor_{layer\,2}$ is larger in value because of the smaller $D_{2\parallel}|_{Surface\,\mathrm{Co}}$ value subtraction.

Similarly, as mentioned above the value of $2\mathcal{D}^x_{1\parallel} + \mathcal{D}^x_{1\perp}$ was enhanced by a factor of 1.8, using the same arguments as for the case of $\mathcal{D}^x_{2\parallel}$ enhancement. Another quantity that has also been modified is the interlayer $D_{1\perp}$. Due to the atomic arrangement in the C_{2v} symmetry $D_{1\perp}$ points along the $[\bar{1}10]$ direction, which is parallel or antiparallel to the magnetization vector $\mathbf{M}$. First-principles calculations have shown that for the Fe double layer $D_{1\perp}$ is much smaller than $D_{1\parallel}$ [42]. Therefore an enhancement of $D_{1\perp}$ is also likely present due to the Co layer of top of the interfacial Fe one.

It is quite fascinating that the findings show that the average DM vectors $\mathcal{D}_{1\parallel}$ and $\mathcal{D}_{2\parallel}$ are mainly governed by the interface DM vectors of the Fe layer $D_{1\parallel}$ and $D_{2\parallel}$. This is also confirmed by a study in our group which found that the DMI in the 2ML Fe/W(110) is an interfacial effect [104]. These results point to a technique where quantum tuning of atomistic DMI is possible. It is noteworthy to mention that SPEELS is the only technique that offers the capability to investigate the interfacial DMI in this way.

4.3 Magnon lifetime

In section 3.2.1 it was pointed out that besides the magnon dispersion, the lifetime of the magnon can also be calculated from the peaks in the difference spectra. As mentioned in section 2.1.3, magnons have a finite lifetime due to their decay into Stoner states. For different systems one would expect a different Stoner continuum and therefore the lifetime of magnon should be different between various samples. However, one has to be careful when extracting the lifetime of the magnon which is essentially given by the Lorentzian linewidth Γ introduced in Eq. 3.4. The difficulty of estimating the magnon lifetimes can present itself when there are multiple magnon modes present in the spectra as well as when the excitation peak is close to the quasi elastic peak. When two magnon modes are well separated in the spectra then the excitation peaks can be fitted accurately. However when the excitation energy of two magnon modes is close enough to where the natural linewidth of one has a large overlap on the other, then it will be difficult to disentangle them. In an example where we have a two layer system such as 1ML Co/1ML Fe/W(110), we observe two magnon modes (see Fig. 4.1) and in an experiment one may choose an incident electron energy E_i such that the $n = 1$ magnon mode is supressed and the $n = 0$ mode is very pronounced which is the case for low values of E_i. This has been done and a sample of results is presented in Fig. 4.9 where a series of SPEELS spectra are shown which were obtained for two wavevectors Q = -0.55 Å^{-1} and Q = -0.65 Å^{-1}. Each wave vector was measured first when the sample was in a remanent magnetization state where $\mathbf{M}\|[1\bar{1}0]$. Then the magnetization was flipped by applying a reverse magnetic field μ_0H = 238 mT and the same vector was measured in a remanent magnetization state.

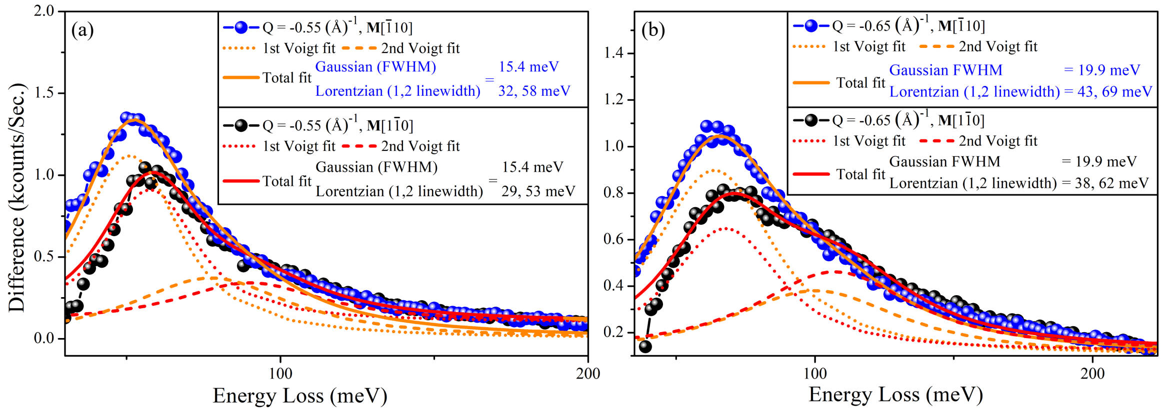

Figure 4.9: SPEELS spectra obtained for two wavevectors (a) Q = -0.55 Å^{-1} (b) Q = -0.65 Å^{-1}. The blue(red) spheres represent experimental spectra recorded in a remanent magntized state of the sample when $\mathbf{M}\|[\bar{1}10]$($\mathbf{M}\|[1\bar{1}0]$). The dotted and dashed orange(red) lines represents the Voigt fit with the Gaussian and Lorentzian linewidth given in the legend. The solid orange(red) curves represent the total fit from both peaks(dotted and dashed).

Experimental results show that the $n = 0$ magnon mode is very pronounced and the $n = 1$ mode is suppressed. The spectra are fitted with a Voigt function which a convolution of a Gaussian and Lorentzian functions. In section 3.2 we mentioned that the Gaussian distribution represents the instrumental broadening and the Lorentzian distribution represents the natural linewidth of the excitation. Therefore, in the Voigt fits the Gaussian full width at half maximum (FWHM) linewidth was given by the resolution of the incident electron beam and the Lorentzian FWHM linewidth was given by the FWHM of the excitation peak in the spectra. Taking these considerations into account, each spectra was fitted by a Voigt function.

Two quantities that can be extracted from the measurements in Fig. 4.9 are the energy splitting $\Delta \mathrm{E} = \mathrm{E}_{\mathbf{M}}(\mathrm{Q}) \neq \mathrm{E}_{-\mathbf{M}}(\mathrm{Q})$ due to the antisymmetric exchange interaction (DMI) and the lifetime τ of the $n = 0$ magnons. We can clearly see in Fig. 4.9 that for a set of two measurements at the same vectors but opposite magnetization directions, the magnon creation peaks do not have the same energy (the position of the magnon energy excitation peak for the two mesurements do not have the same energy $\Delta E \approx 5$ meV), when compared for two opposite sample magnetization directions. This is a clear indication that there is a pronounced DMI present. Since this effect was discussed in the previous results section, the reader is referred to section 4.2.1. In Fig. 4.9(a), at a wave vector of Q = -0.55 Å, the Lorentzian linewidth is different between the two opposite **M** directions. This is also the case in Fig. 4.9(b). One can notice that the $n = 0$ mode can be fitted very well but in the case of the $n = 1$ magnon mode the natural broadening of the peak is large and the intensity of the excitation is low as expected and therefore the associated error with the fitting is also larger. The $n = 1$ mode can actually be seen as a pronounced shoulder in Fig. 4.9(b) for the measurement in the $\mathbf{M}[1\bar{1}0]$ magnetized direction remanent state. Overall, this allows us to extract the lifetime from the $n = 0$ and $n = 1$ mode magnons. In the end one may got a an approximation of the magnon lifetimes in such a system by looking at the $n = 0$ mode. The results for a range of wavevectors is presented in Fig. 4.10, where

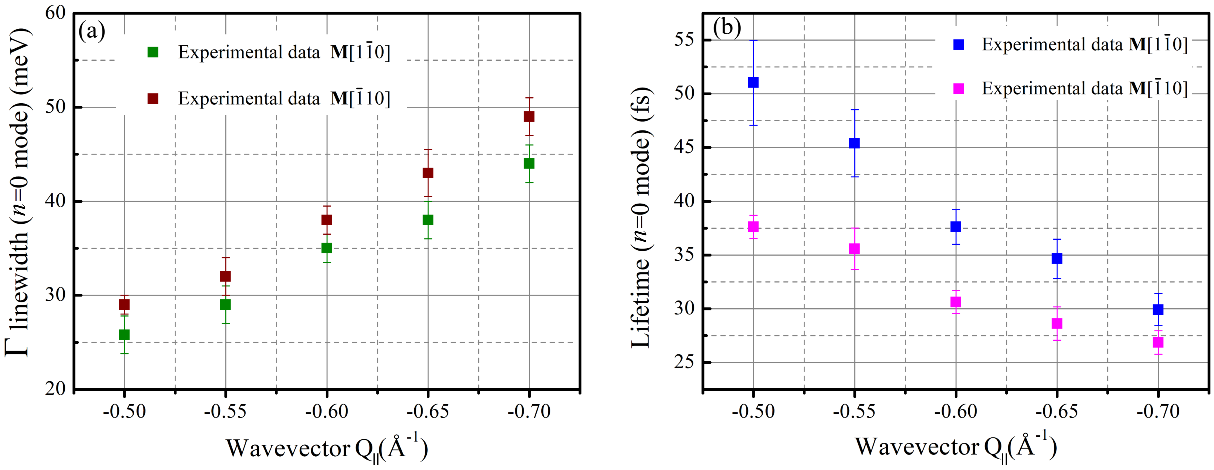

Figure 4.10: (a) Experimentally obtained Γ of the Lorentzian linewidth of the $n = 0$ magnon excitation peak obtained from the SPEELS difference spectra as described in Fig. 4.9. Each experimental spectra peak is fitted with a Voigt function while the Gaussian instrumental broadening is fixed at a constant value. The green squares represent experimental data obtained when the sample was in the magnetized remanent state $\mathbf{M}||[1\bar{1}0]$ and the dark red squares are experimental data when the sample was in the magnetized remanent state $\mathbf{M}||[\bar{1}10]$. (b) Extracted magnon lifetime from the Lorentzian natural linewidth Γ. The blue squares represent experimental data obtained when the sample was in the magnetized remanent state $\mathbf{M}||[1\bar{1}0]$ and the pink squares are experimental data when the sample was in the magnetized remanent state $\mathbf{M}||[\bar{1}10]$. The associated error bars are provided.

the Lorentzian natural linewidth broadening represented by the Γ is shown in part (a) and the calculated lifetime of the magnon is shown in part (b). The lifetime of the magnon can be calculated according to Eq. 3.4 introduced in section 3.2. The uncertainty in the lifetime is given by $\Delta\tau = \Delta\Gamma 2\hbar/\Gamma^2$ which comes from the standard propagation for quotient values. From Fig. 4.10(a) we can see as is expected that as the wave vector is increased the natural linewidth of the magnon $n = 0$ mode also increases. This is due to the fact that at higher energies magnon have a stronger dissipation channel into Stoner states. Therefore the lifetime of the magnon is affected as well since it is inversely proportional to the natural Lorentzian linewidth of the magnon excitation peak. From Fig. 4.10, one can also see the effect of DMI on the magnons in this system. When the same wavevector is measured at two equal but opposite magnetization directions ($\mathbf{M}\|[\bar{1}10]$,$\mathbf{M}\|[1\bar{1}0]$), in effect the magnons are traveling in two opposite directions at the surface of the crystal. In the presence of the antisymmetric DMI exchange interaction we would expect that the lifetimes for these two opposite directions should be different. This is exactly what we observe as is evident form Fig. 4.9 and agrees with findings on a 2ML Fe/W(110) [107]. The direction of the energy splitting of the excitation peaks i.e. ($\mathbf{M}\|[\bar{1}10]$ to lower energies($\mathbf{M}\|[1\bar{1}0]$) to higher energies) is due to the chiral damping effect. This has been observed in a 2ML Fe/W(110) in our group in Ref. [107]. At small wavevectors, especially in the limit of ferromagnetic resonance (Q=0), magnons are damped mainly by spin orbit induced damping. This is where the spin precession of the magnetic moment is coupled to its orbital motion and the lattice. There is also coupling to the surrounding lattice and hence a damping is induced. For high wavevectors, dissipation into Stoner states becomes dominant which is known as Landau type damping. In our case, magnons are subject to a large SOC because of the hybridization with the W(110) substrate. Here, both effects, SOC and Landau damping are at work. Time reversal (reversing magnetization ($\mathbf{M}\|[\bar{1}10]$ to $\mathbf{M}\|[1\bar{1}0]$) inverts the angular and linear momentum, and therefore it inverts the spin-orbit contribution to the magnon lifetime [107]. This is exactly what we observe in our experiment as seen from Fig. 4.9. The linewidth and lifetime of the $n = 1$ magnons can also be extracted from the experimental data. In general the expectation is that the n>0 mode magnons should posses a shorter lifetime and therefore a larger natural linediwth than the $n = 0$ magnons. This is due to the fact that the n>0 magnons precess out of phase [112]. The results for this analysis is given in Fig. 4.11. Indeed, we see that the natural linewidth Γ is larger than in the $n = 0$ magnon case. Therefore the lifetime is shorter for the $n = 1$ mode. However the error for this is also larger since determining the peak positions is not straight forward anymore because of the large natural linewidth. As was mentioned previously, the Voigt fit is a convolution of the Lorenzian and the Gaussian functions, which represent the natural linewidth and the experimental broadening, respectively. It would be of value to look at the broadening of the convoluted peaks to see whether or not the linewidth of the increasing wavevectors also increases. The results in Fig. 4.12 show when both the Gaussian FWHM and the Lorentzian linewidth are taken into account. It is clear that the total broadening of the magnon excitation peak is not affected by the instrumental broadening to such a degree that determining the Lorentzian is ambiguous, i.e. the resolution in the

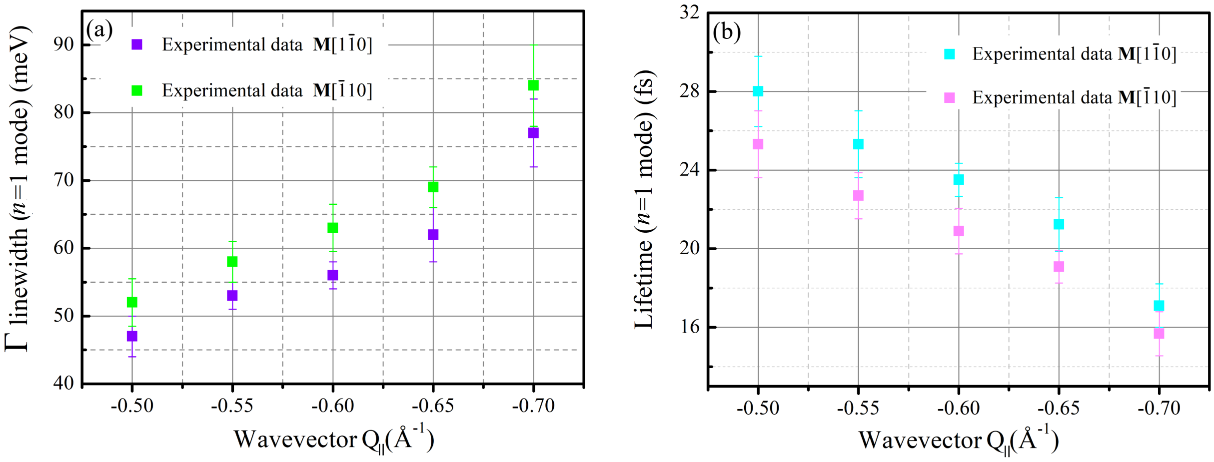

Figure 4.11: (a) Experimentally obtained Γ of the Lorentzian linewidth of the $n = 1$ magnon excitation peak obtained from the SPEELS difference spectra as described in Fig. 4.9. Each experimental spectra peak is fitted with a Voigt function while the Gaussian instrumental broadening is fixed at a constant value. The purple squares represent experimental data obtained when the sample was in the magnetized remanent state $\mathbf{M}||[1\bar{1}0]$ and the neon green squares are experimental data when the sample was in the magnetized remanent state $\mathbf{M}||[\bar{1}10]$. (b) Extracted magnon lifetime from the Lorentzian natural linewidth Γ. The cyan squares represent experimental data obtained when the sample was in the magnetized remanent state $\mathbf{M}||[1\bar{1}0]$ and the pink squares are experimental data when the sample was in the magnetized remanent state $\mathbf{M}||[\bar{1}10]$. The associated error bars are provided.

experiment is very good.

4.4 Summary

In summary, in the 1ML Co/1ML Fe/W(110) two magnon peaks are clearly observed corresponding to the $n = 0$ and $n = 1$ modes. The experimental data was described in the NNNH model and it was found that the interlayer $J_{N\perp}$ coupling between the interface Fe layer and the Co layer is very weak compared to the Fe doublelayer on W(110). The intralayer exchange coupling constant in the Fe doublelayer in the trilayer structure of 1ML Co/2ML Fe/W(110) was found to be enhanced compared to the Fe doublelayer on W(110), and the interlayer exchange coupling between the middle Fe layer and the top Co layer was found to be weak but with the same value as in the 1ML Co/1ML Fe/W(110) system. The exchange coupling constants obtained from the 1ML Co/1ML Fe/W(110) and 1ML Co/2ML Fe/W(110) are given in Tab. 4.2 for comparison. The DMI was found to have a large effect on the magnon dispersion in 1ML Co/1ML Fe/W(110). The components of

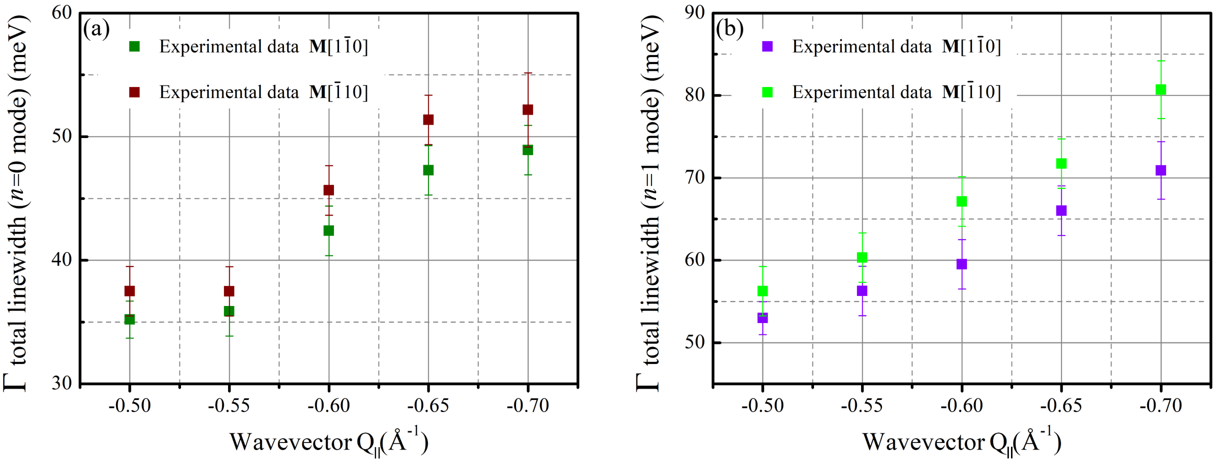

Figure 4.12: Experimentally obtained Γ of the convoluted (a) $n = 0$ and (b) $n = 1$ magnon excitation peak obtained from the SPEELS difference spectra as described in Fig. 4.9. Each experimental spectra peak is fitted with a Voigt function while the Gaussian instrumental broadening is fixed at a constant value. (a) The green squares represent experimental data obtained when the sample was in the magnetized remanent state $\mathbf{M}\|[1\bar{1}0]$ and the dark red squares are experimental data when the sample was in the magnetized remanent state $\mathbf{M}\|[\bar{1}10]$. (b) The purple squares represent experimental data obtained when the sample was in the magnetized remanent state $\mathbf{M}\|[1\bar{1}0]$ and the neon green squares are experimental data when the sample was in the magnetized remanent state $\mathbf{M}\|[\bar{1}10]$. The associated error bars are provided.

Table 4.2: Experimentally determined exchange constants on 1ML Co/1ML Fe/W(110) and 1ML Co/2ML Fe/W(110). The notation is as follow. For example 1ML Co/2ML Fe/W(110) (Co^3) and $J^2_{\mathrm{Fe}}/J^3_{\mathrm{Co}}$ corresponds to the exchange constant coupling in the top Co layer to the Fe layer below and Co layer above, hence the $J^2_{\mathrm{Fe}}/J^3_{\mathrm{Co}}$ notation.

Sample (T=300K)	$J_{N\parallel}$(meV)	$J_{N\perp}$(meV)	$J_{NN\parallel}$(meV)	$J_{NN\perp}$(meV)
1ML Co/1ML Fe/W(110) (Fe^1)	5.6	4.5	3.4	0
1ML Co/1ML Fe/W(110) (Co^2)	12	4.5	0.5	0
1ML Co/2ML Fe/W(110) (Fe^1)	14.7	14.7	8.8	8.8
1ML Co/2ML Fe/W(110) (Fe^2)	15	$14.7_{\mathrm{Fe}}/4.5_{\mathrm{Co}}$	9.3	$8.8_{\mathrm{Fe}}/0_{\mathrm{Co}}$
1ML Co/2ML Fe/W(110) (Co^3)	16	4.5	1	0

the DM vectors $2\mathcal{D}^x_{1\|} + \mathcal{D}^x_{1\perp}$ and $\mathcal{D}^x_{2\|}$ were enhanced by a factor of 1.8 and 1.5, respectively, compared to the 2ML Fe/W(110) system [104].

The magnon lifetime in the 1ML Co/1ML Fe/W(110) was observed to be different due to the DMI as expected. Due to the relatively small value of the Gaussian FWHM, the total broadening of the magnon excitation peak did not impair the measurements.

5. Fe and Co/Fe multilayers on Ir(111)

This chapter contains results on the ultrathin Fe and Fe/Co multilayers on Ir(111). There are two main parts to each results section: the symmetric Heisenberg exchange in section 5.1 and the antisymmetric exchange (Dzyaloshinskii-Moriya Interaction) in section 5.2. Results are presented and discussed in section 5.1.1, where measurements on 2ML Fe/Ir(111) were performed at a temperature of 13 K. Also, the 3 ML, 4 ML Fe/Ir(111) was investigated at room temperature. Section 5.1.2 will show results on a bilayer sample of 1ML Co/1ML Fe/Ir(111) and 2ML Co/1ML Fe/Ir(111). The low exchange coupling constants found for the Ir(111) systems will be discussed. The last section 5.2 will discuss the role of DMI in the samples investigated and its effect on the magnon dispersion.

5.1 Symmetric Heisenberg exchange

In this section we present results on the magnon dispersion obtained from elemental films of Fe grown on the Ir(111) substrate. The results are discussed in terms of the symmetric Heisenberg exchange interaction. Measurements performed on 2ML Fe/Ir(111) were done at T=13K. Measurements on 3ML Fe/Ir(111) were performed at T=300K.

5.1.1 2ML, 3ML Fe/Ir(111) system

From Ref. [12], a ferromagnetic signal appears T=300K in Fe on Ir(111) when the thickness of the film is 3 ML and above. This was also confirmed in our longitudinal MOKE setup introduced in section 3.1.1. SPEELS experiments were performed on a 3 ML Fe/Ir(111) sample at room temperature (RT). To improve surface quality the samples were annealed with a low power of up to 2 Watts after initial growth.

Experimental results of SPEELS measurements performed on 3ML Fe/Ir(111) are presented in Fig. 5.1. There is no available data for the $n = 1$ and $n = 2$ magnon modes since the total magnon signal intensity is far too low and while the $n = 0$ mode shows a well defined magnon excitation peak, the higher magnon modes are too low in intensity to be observed. This may be due to the weak ferromagnetic signal observed since normally a weak ferromagnetic signal would correspond to a weak spin resolved signal in the SPEELS spectra.

At the first step to analyze the experimental results, *ab initio* calculations have been performed by Khalil Zakeri, with the code provided by Arthur Ernst, to obtain the magnon dispersion bands. Initial calculations revealed that the calculated $n = 0$ mode was overestimated. This was surprising since normally experimental data of Fe films on Ir substrates is fairly well described by *ab initio* calculations [105, 110]. The $n = 0$ magnon band was

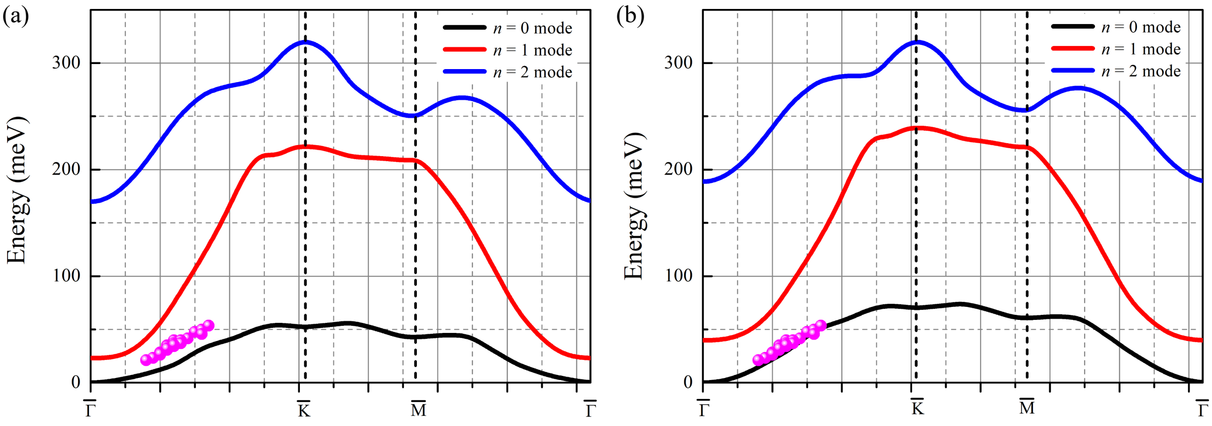

Figure 5.1: (a),(b) Plotted magnon dispersion curves from *ab initio* calculations represent the $n = 0$ mode (black curve), $n = 1$ mode (red curve) and $n = 2$ mode (blue curve). (a) Experimental data for the $n = 0$ mode in 3ML Fe/Ir(111) system represented by magenta spheres. The calculated $n = 0$ mode has been renormalized by the Fe magnetic moment value. (b) Experimental data for the $n = 0$ mode in 3ML Fe/Ir(111) system represented by pink spheres. The calculated $n = 0$ mode curve has been renormalized by the Fe magnetic moment value for the next and next neareast interlayer coupling. The *ab initio* calculations were performed by Khalil Zakeri using the *ab initio* code developed by Arthur Ernst.

recalculated by fixing the exchange coupling constants J_{ij} and renormalizing by the Fe magnetic moment in the interface layer which was $2.7\mu_{\mathrm{B}}$. This was done in order to compensate for the overestimated value of the magnetic moment in the interface Fe layer. The results are shown in Fig. 5.1(a). As is evident the $n = 0$ mode is underestimated. This is due to the fact that in the previous step, the magnetic moment was effectively set to 1, which is an oversimplification. Therefore in the next step magnon calculations were performed once again with the next and next nearest interlayer exchange coupling constants J_{ij} adjusted slightly to observe the value that agrees with the data. This adjustment was taken from the Heisenberg model calculations performed similar to the method introduced in chapter 2, section 2.1.1. The results are shown in Fig. 5.1(b). The calculated $n = 0$ mode curve fits very well to the experimental data. This suggests that the exchange coupling pattern of the underlying Fe film is complex and the interface Fe magnetic moment may be somewhere between the bulk value of $2.2\mu_{\mathrm{B}}$ and $2.7\mu_{\mathrm{B}}$. The exchange coupling constants in the 3ML Fe/Ir(111) is presented in Fig. 5.2 which shows a complex pattern of exchange coupling constants in the atomic layers. The exchange coupling constants between the interface Fe layer and the surface Fe layer have not been included in the picture for clarity, they are -1.9 meV, 1 meV, -0.05 meV for J_N, J_{NN} and J_{NNN}, respectively.

Comparing Figs. 5.1(a) and (b) one can immediately notice that the $n = 0$ magnon branch exchange stiffness D is higher in Fig. 5.1(b). Using a similar approach as to that in Eq. 2.20, the $n = 0$ magnon branch exchange stiffness D can be calculated to give 40 meVÅ^2 ± 5 for Fig. 5.1(a) and 72 meVÅ^2 ± 7 in Fig. 5.1(b). This reveals an extremely

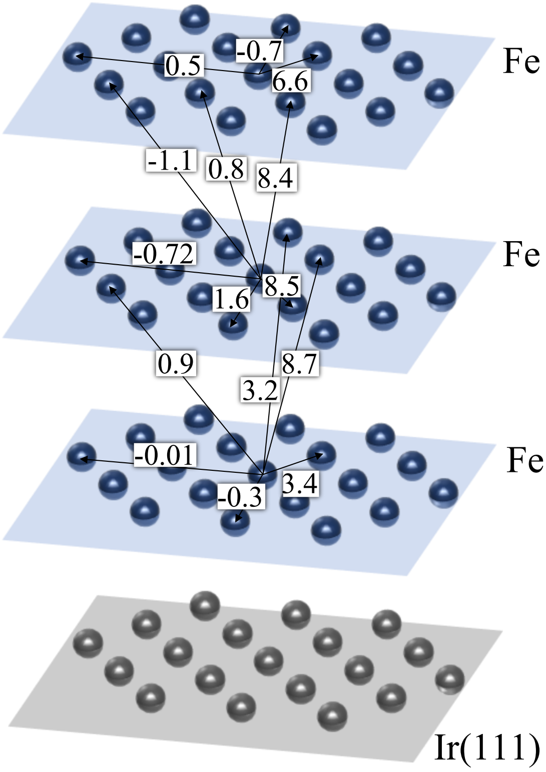

Figure 5.2: 3ML Fe/Ir(111). The calculated interatomic low exchange coupling constants resulting from the *ab initio* calculations. All values are given in meV. The *ab initio* calculations were performed by Khalil Zakeri with the code obtained from Arthur Ernst.

soft magnon branch when compared to 2ML Fe/W(110) for example (see [112]). The implication is then that the overall exchange coupling constants are also reduced as *ab initio* calculations revealed.

Building on the above discussion, an interesting point is to discuss the group velocity v_g of the magnon wave packet. The group velocity is given by

$$v_g = \frac{1}{\hbar}\frac{\partial \varepsilon}{\partial \mathrm{Q}_{\|}} \tag{5.1}$$

When the magnon band dispersion posses a small exchange stiffness D, one would not expect a large group velocity. In Fig. 5.3 the group velocity has been extracted for the case where the *ab initio* calculations are used (black solid curve) and for the case where the experimental data is considered (blue points). It is evident that the $n = 0$ band magnon group velocities values are around the values of the calculated $n = 0$ bands which further suggests the agreement of data with the calculated soft magnon dispersion. The values are much lower than to the ones reported in [109] on 2ML Fe/W(110) (Q $=$ 0.5 Å^{-1} and 24.4 km/s), which is expected since the $n = 0$ mode dispersion in that system is stiffer than in the one studied here. In fact, the group velocity in the $n = 0$ magnon mode from 3ML Fe/Ir(111) has its maximum at around Q=0.75 Å^{-1} which is 2.4 km/s. This is a

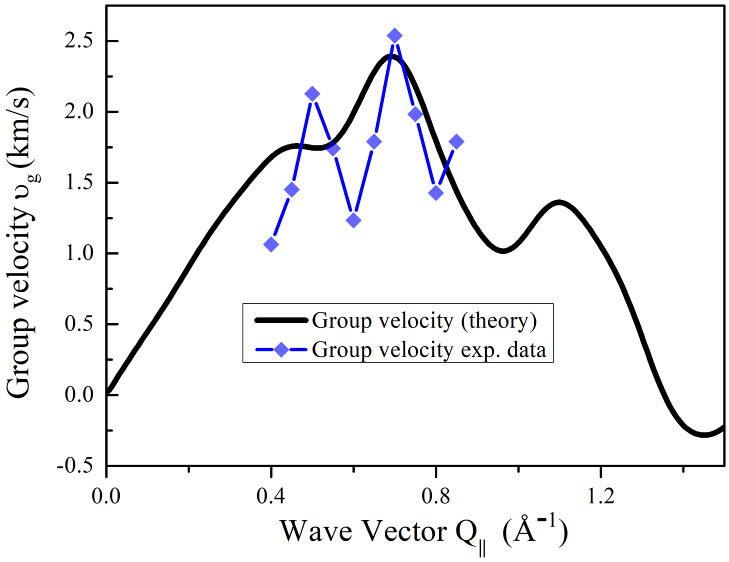

Figure 5.3: Calculated group velocity for the $n = 0$ magnon mode for the renormalized *ab initio* in Fig. 5.1 calculations (black curve) and experimental data (magenta points) from 3ML Fe/Ir(111).

very low value and corresponds to a soft magnon branch.

The sample 2ML Fe/Ir(111) is not ferromagnetic at RT as shown in Ref. [12] and confirmed in our longitudinal MOKE experiments. In the SPEELS experiment, a magnon signal was observed on in this system when measuremens were performed at T = 13 K. In that context results obtained on 2ML Fe/Ir(111) at T = 13K are presented in Fig. 5.4(a), where the calculated dispersion curves are fit to the experimental data in the NNNNH model. The values for the low exchange coupling constants in the calculated dispersion were taken from *ab initio* calculations for the 2ML Fe/Ir(111). The incident electron beam energy used for the experiments was $E_i = 3.2$ eV with a resolution between 12 and 18 meV. Interestingly in this work, the optimal incident electron energy in terms of magnon peak intensity and resolution was 3.2 eV. This fact put a limit on the range of wave vectors that could be measured, since the range of wavevector Q that are available to probe depends on the incident electron energy E_i (see Eq.3.2 and section 3.2). The $n = 0$ magnon mode was very pronounced in the SPEELS spectra while the $n = 1$ mode was supressed, this is in general true since for lower E_i incident energies the $n = 0$ mode is amplified. Therefore we make no comment on the $n = 1$ mode and the exchange coupling constants contained therein.
From previous SPEELS experiments on Fe/Ir(001) one would expect low magnon energies when compared to Fe/W(110) for example [110, 112]. In Fig. 5.4(a), the Heisenberg model is not able to describe the $n = 0$ magnon mode. In Fig. 5.4 (b) the calculated magnon bands from *ab initio* calculations cannot describe the dispersion well, where the $n = 0$ mode is too stiff. Therefore a similar approach to that of the above discussed 3ML

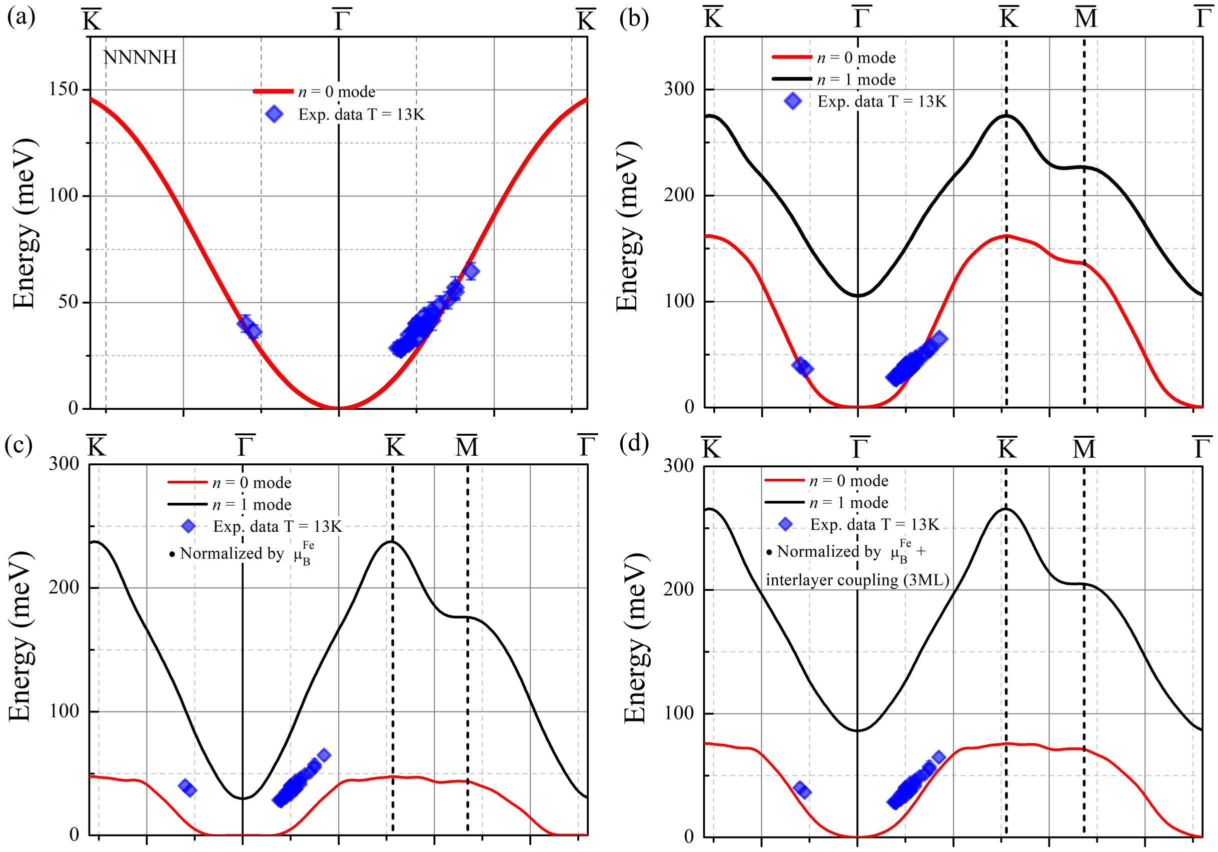

Figure 5.4: Experimental results on 2ML Fe/Ir(111) obtained at T = 13K. The incident electron energy is $\mathrm{E}_i = 3.2$ eV with a resolution between 12 and 18 meV. In (a) The calculated $n = 0$ mode dispersion in the NNNNH model. The exchange coupling constants used for the dispersion are taken from *ab initio* calculations. $J^1_{N\|} = 3.8$ meV, $J^1_{NN\|} =$ -0.3 meV and $J^1_{NNN\|} = 0$ meV. The interlayer low exchange coupling constant between the interface and the surface layer is $J^1_{N\perp} = 11.8$ meV, $J^1_{NN\perp} = 1.1$ meV and $J^1_{NNN\perp} =$ -0.2 meV. In (b)-(c) dispersion curves calculated from *ab initio* calculations. (b) Calculated magnon bands without renormalization. (c) Calculated magnon bands with renormalizing by $\mu_{\mathrm{B}}^{\mathrm{Fe}}$. (d) Calculated magnon bands with renormalizing by $\mu_{\mathrm{B}}^{\mathrm{Fe}}$ and a strong interlayer coupling (taken from 3ML/Ir(111)). Calculations performed by Khalil Zakeri with the code provided by Arthur Ernst.

Fe/Ir(111) was used where the exchange coupling constants were first normalized by the interface magnetic moment of Fe $\mu_{\mathrm{B}}^{\mathrm{Fe}}$, this was done in Fig. 5.4(c). Unsurprisingly, just as in the 3ML Fe/Ir(111) case the slope of the $n = 0$ magnon mode is correct but the energy values are underestimated. Therefore the interlayer coupling was normalized by using values taken from the 3ML Fe/Ir(111) second to the third Fe layer. The results shown in Fig. 5.4(d) show a fairly good agreement with the experimental data. In Fig. 5.4(a) and (b) the $n = 0$ magnon branch energy goes up to 150 and 160 meV at the SBZ boundary, respectively. However this does not describe the experimental data as already mentioned.

In (d), where the calculated dispersion is in good agreement to the experimental data, the $n = 0$ magnon branch does not exceed 75 meV at the SBZ boundary and the experimental value at $\mathrm{Q}_{\parallel} = 0.85$ Å^{-1} is 65 meV. This is significantly lower than the 2ML Fe/W(110) (see Fig. 4.5) system where at $\mathrm{Q}_{\parallel} = 0.85$ Å^{-1} the magnon energies are well above 100 meV and nearly 175 meV at the SBZ boundary in the $\overline{\Gamma}$-$\overline{\mathrm{H}}$. The calculated dispersion in Fig. 5.4(c), where the agreement with the experiment is good, suggests that even at the SBZ boundary the magnon energies will not exceed 75 meV in the $\overline{\Gamma}$-$\overline{\mathrm{K}}$ direction. There is no data available above $\mathrm{Q}_{\parallel} = 0.85$Å^{-1} but it possible to infer from the calculated dispersion trend that the $n = 0$ magnon mode will be nearly flat pointing to a very low group velocity and almost standing wave like behavior closer to the SBZ.

The low exchange coupling constants used in the Heisenberg model revealed that the intralayer coupling in the interface Fe layer remains nearly the same as the ones derived by *ab initio* calculations but the interlayer coupling turned out to be slightly stronger. In the case of the 2ML system, the substrate is next to the interface layer which in turn is next the the surface layer. In the 3ML Fe/Ir(111) system, the interface Fe film has a middle Fe layer which is then adjacent to the surface film. One would then expect a stronger coupling for the 3ML system, both intralayer and interlayer due to higher coordination number. However, surprisingly the trend was opposite. Using *ab initio* calculations, in the 2ML system the Fe-Ir(111) interface $J_{N\parallel} = 3.6$ meV and $J_{N\perp} = 11.89$ meV. In the 3ML Fe/Ir(111) the Fe-Ir(111) interface had $J_{N\parallel} = 3.42$ meV and $J_{N\perp} = 8.7$ meV. The $J_{N\parallel}$ and $J_{N\perp}$ increase for the 2ML system when compared to the 3ML Fe/Ir(111). This clearly shows the complex pattern of exchange coupling constants of the system and the strong interlayer coupling of the interface Fe layer to the surface Fe layer in the 2ML system. This is a feature that appears before and after normalization and suggests that the weaker interfacial layer coupling in the 3ML Fe system has its origins in the electron spin density redistribution to the extra third surface layer. As far as temperature effects, the discussion is limited. In Fe-Ir (001) superlattices, in the low coverage regime of Fe layer, the Currie temperature T_{C} was found be to about 230 K [1]. Since the 3ML sample is weakly ferromagnetic at room temperature, T_{C} is higher than this value. However, we cannot comment conclusively on the temperature effects because the Currie temperature T_{C} is not known for either of the samples on the Ir(111). From SPEELS studies on elemental films of Fe and Co on W(110) temperature effects were found to be negligible [27, 112]. Therefore it is likely that the the main reason behind the exchange coupling constant difference in the 2ML Fe and 3ML Fe/Ir(111) is due to the renormalization of the exchange constant pattern as a result of the different coordination number in the samples and spin density redistribution.

The magnon peak intensities in the spectra were small across the whole range of wavevectors measured. This is due to the fact that the ferromagnetic MOKE signal in the longitudinal geometry for the 2ML Fe/Ir(111) does not appear and at a low temperature of 13K the magnon signal shows up as a very weak spin resolved peak in the SPEELS spectra. In addition, the comparison to the trilayer can be only qualitative since the system is different.

In order to obtain information about the surface magnon mode in thick Fe films, experiments were performed on various thicknesses higher than the ones already presented. Results on films thicker than 3ML Fe/Ir(111) are presented in Fig. 5.5. The 4ML Fe films have a noticeable increase in exchange stiffness D in the magnon dispersion. For all films thicker than 11ML Fe, the effect of the substrates states hybridizing with the electronic states of the films is negligible. This is due to the fact that the penetration depth in the SPEELS experiment is finite and is on the order of 10 Å with the low incident electron energies used. The bulk dispersion of Fe is plotted in dark red spheres in Fig. 5.5 and has a higher exchange stiffness D than the Fe films of all thicknesses presented. The stiffness constant D for bulk Fe is 260 meVÅ^2 which is much larger than the earlier derived D for 3ML Fe/Ir(111) of 72 meVÅ^2 [60]. In a thick film i.e. >10ML the low lying energy magnon mode is the surface mode because of the lowered coordination number, the higher energy magnon modes are the bulk bands. When comparing the thick films in Fig. 5.5 with the bulk Fe magnon dispersion the energies and the exchange stiffness of the bulk is higher than that of the thick films. Therefore this indicates that the surface mode exchange constants $J_{||}$ in the thick films should be lower when compared to the bulk ones.

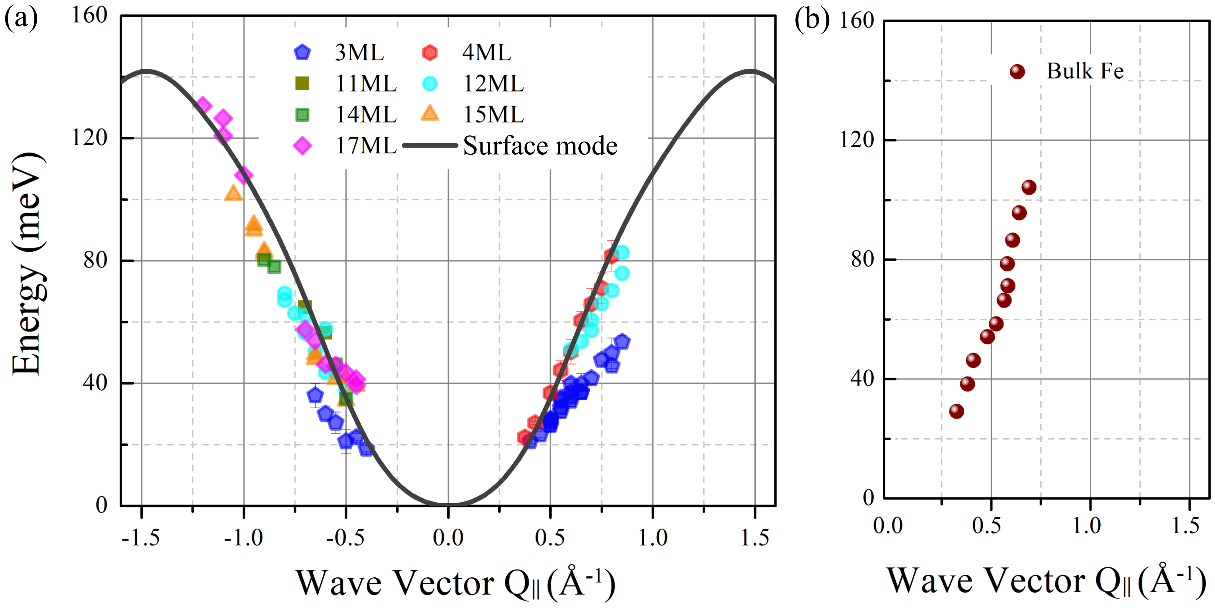

Figure 5.5: (a) The $n = 0$ mode magnon dispersion in Fe films on Ir(111) with thickness up to 17ML. The calculated dispersion was obtained by taking exchange coupling constant values from first principles calculations on a 6ML Fe/Ir(111). (b) Bulk Fe dispersion taken from reference [60] measured via inelastic neutron scattering in the [110] direction.

In order to answer whether or not the surface mode was mesured in thick films and if in the 2ML Fe,3ML Fe /Ir(111) the interface was probed, we start with the assumption of a semi-infinite crystal and calculate the surface mode in a bulk like structure in order to compare the experimental data to it. The starting point is Eq. 2.7 introduced in chapter 2, section 2.1.1. In the surface film of an fcc(111) structure, there are 6 intralyer nearest, next nearest and third next nearest neighbors. For the atomic layer underneath the surface layer there are 3 interlayer nearest, next nearest and third next nearest neighbors. The spin wave amplitude equations in the first layer, and the layers below and above in the NNNNH model including the decay factor is given by Eq. 7.1 and Eq. 7.2 in the Appendix which is chapter 7, section 7.1. Solving the two equations for the surface mode we plot the results in Fig. 5.5(a) as the fitting curve to the experimental data. The exchange coupling constants used as the fitting parameters were taken from *ab initio* calculations on a thick Fe film (6ML) and normalized by the magnetic moment of Fe. The calculated curve clearly agrees well with the experimental data of the thick Fe films, and deviates for a thin film of 3ML Fe. This suggests that indeed the surface mode of the thick Fe films is being measured and the effect of the Ir(111) is not seen by the experiment. Moreover, this shows that when the thinner layers were measured, i.e. 2ML and 3ML systems, the experiment was sensitive to the interface layer. Interestingly, the 4ML Fe data (red hexagons) shows a good agreement with the calculated dispersion up to a $Q_{\|} = 0.8$ Å^{-1}. Here the possibilities are either the experimental data will deviate from the calculated semi-infinite crystal surface mode at $Q_{\|} > 0.8$ Å^{-1} or at a thickness of 4ML the experiment was no longer sensitive to the substrate effects. Without covering more of the SBZ range with our experiment, it is difficult to conclude between the two options.

5.1.2 1ML Co/Fe/Ir(111), 2ML Co/Fe/Ir(111) multilayer system

In light of recent results on multilayer systems [93, 110] another interesting system to investigate is the 2ML Co/ 1ML Fe/Ir(111). The samples were grown by first annealing the Fe interface layer after which the sample was allowed to cool down for a time period of 1-1.5 hours before depositing the Co overlayers. Typical SPEELS spectra recorded on this system is presented in Fig. 5.6(a),(b) along with a series of measured spectra in (c).

In Fig. 5.6(a), the intensity spectra for the two possible spin orientations of the incoming beam at $Q_{\|} = 0.55$ Å^{-1} are presented. The spin down channel denoted by $I_{\downarrow}$ shows two bumps relative to the the spin up channel $I_{\uparrow}$. Taking the difference of the two spin channel intensities gives the results in Fig. 5.6(b) where we can clearly observe two distinct peaks representing two magnon modes ($n = 0$ and $n = 1$). The difference in the two spin channels is clear enough that we may even identify the magnon creation energy from Fig. 5.6(a). The measurements can be done for various wavevectors and multiple magnon modes can be identified belonging to the $n = 0$ and $n = 1$ branch. A series of measured spectra is presented in Fig. 5.6(c), where the dispersion is clearly seen in both identifiable magnon branches. Since this is a 3ML sample, there should be in principle a third magnon branch observed, however this would be at higher energy losses where in our experiment

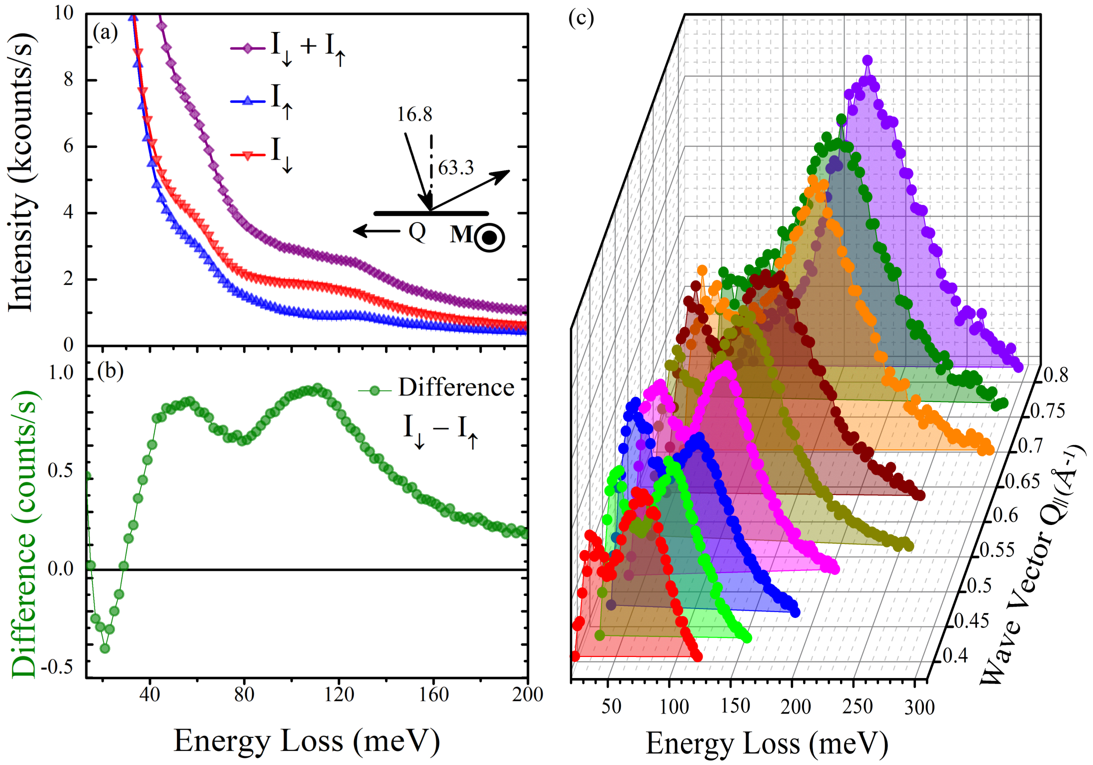

Figure 5.6: An example of SPEELS spectra recorded at a wavevector of $Q_{\|} = 0.55$ Å^{-1} on a 2ML Co/ 1ML Fe bilayer epitaxially grown on Ir(111). The spectra are recorded at the incident energy of 3.2 eV and T = 300K. (a) The red and blue spectra, denoted by $I_{\downarrow}$ and $I_{\uparrow}$, are recorded with the polarization vector of the incident electron beam being parallel and antiparallel to the magnetization **M**, respectively. The total intensity $I_{\downarrow} + I_{\uparrow}$ is shown by the purple squares. The scattering geometry is schematically illustrated as the inset. (b) Difference intensity $I_{\downarrow}$ - $I_{\uparrow}$ spectra are shown by green colored circles.(c) A series of difference SPEELS spectra recorded for various wave vectors ranging from $Q_{\|} = 0.4$ to 0.8 Å^{-1}.

the intensity of the third magnon branch was far too low and could not be observed.
We present in Fig. 5.7 experimental results obtained for a 2ML Co/1ML Fe/Ir(111) for a series of measured wave vectors along two opposite SBZ directions. In Fig. 5.7 the experimental data is plotted alongside *ab initio* calculated magnon bands for 2ML Co/1ML Fe/Ir(111) system in which the agreement of the data with the calculated curves is very good, surprisingly no renormalization of the magnon bands was needed as in the previous case for the 2ML,3ML Fe/Ir(111) since corrections for this were already included in the original *ab initio* calculations. These corrections were the following. It is known that for Co films *ab initio* calculations overestimate the magnon bands [13, 40, 110]. Therefore in order to account for this in our case the exchange splitting between the majority and minority spin split bands was decreased by 0.8 eV and the calculations was performed. The results gave good agreement with the experimental data as seen in Fig. 5.7. One can notice that the $n = 1$ band is still slightly overestimated. Figure 5.9 shows a plot

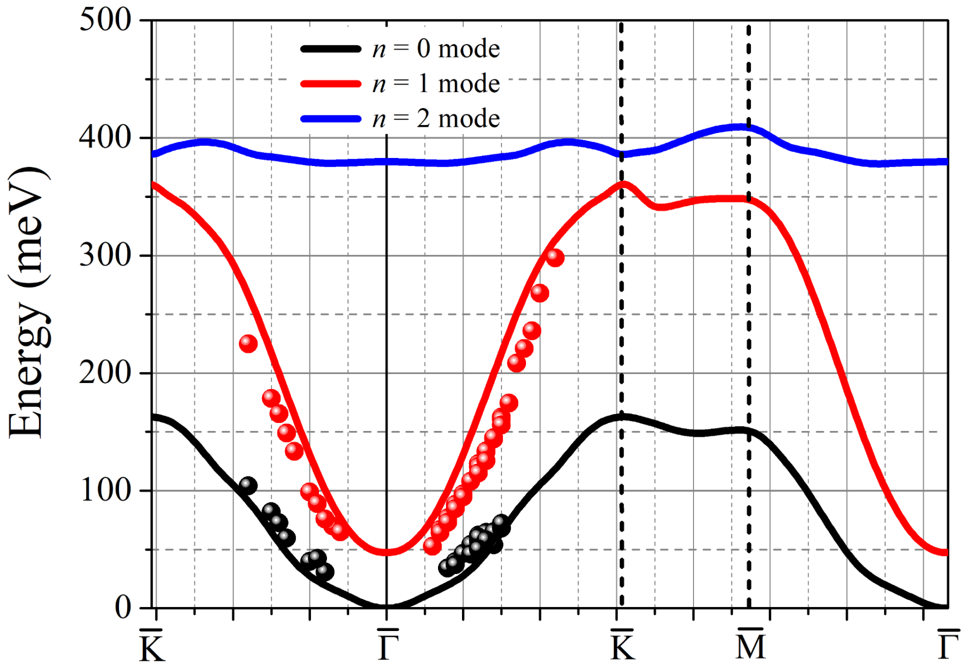

Figure 5.7: Experimental results obtained on 2ML Co/1ML Fe/Ir(111) plotted along with *ab initio* calculations (black, red and blue curves). The *ab initio* calculations were performed by Khalil Zakeri with the code obtained from Arthur Ernst.

of the behavior of exchange coupling constants in the Fe interface layer as a function of the distance from the central atom for intralayer coupling as well as interlayer coupling. One can immediately notice that the *ab initio* calculations show that exchange coupling constants higher than the third order may also be important. The plot also reveals a complicated behavior of the system with both ferromagnetic and antiferromagnetic coupling. An important point is that the interlayer distances play no role in the simple Heisenberg model calculations considered in chapter 2 and section 2.1.1. While this approach in the Heisenberg model is powerful in many respects as discussed in section 2.1.1, in the way it is used there it fails to take into account important assumptions. Since the exchange interaction is based on the Pauli principle and is Coulombic in nature, changing the distance of the atomic layers will have a great effect on the magnon dispersion relation. In the *ab initio* calculations presented in Fig. 5.7(a), the Fe-Fe interlayer distance is taken to be 2.02 Å as reported in [12]. In this case we can safely say that the *ab initio* calculations are the ones to be relied on since they not only take into account hundreds of nearest neighbors but also atomic layer distances and detailed magntic moments.

These results on the exchange coupling constants can be compared to the ones obtained in our group on 2ML Co/1ML Fe/Ir(001) [110]. The intralayer interface Fe exchange coupling constants in 2ML Co/1ML Fe/Ir(001) are considerably smaller and next nearest neighbor exchange coupling constants are positive while in the case of 2ML Co/1ML Fe/Ir(111) they are negative. Also, most noticeable is the fact that the interlayer exchange coupling

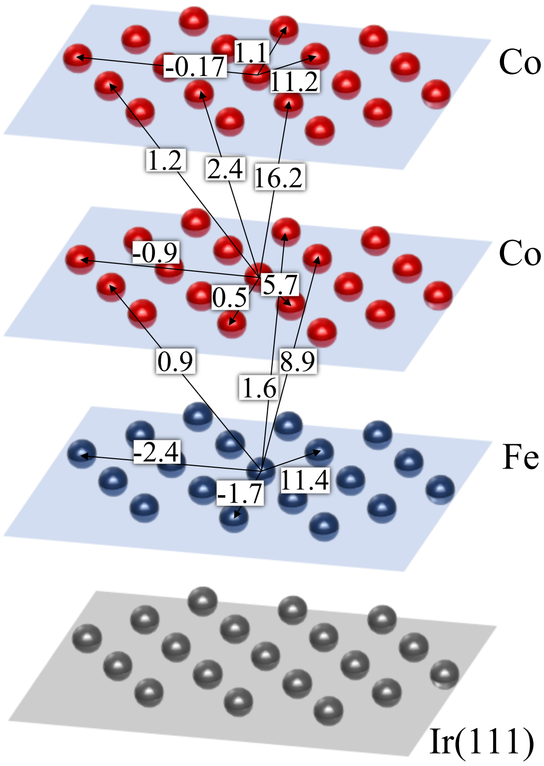

Figure 5.8: (a) 2ML Co/1ML Fe/Ir(111) atomic layers. The calculated interatomic exchange parameters resulting from the *ab initio* calculations. All values are given in meV.

between the interface Fe layer and the top most Co layer is ferromagnetic ($J > 0$) in the case of the 2ML Co/1ML Fe/Ir(001) and antiferromagnetic ($J < 0$) in the case of 2ML Co/1ML Fe/Ir(111) up to three next nearest neighbors. In the case of the Ir(001) surface there is 4 nearest neighbors, while in the Ir(111) there are 6. The distance between the nearest atomic neighbors in the Ir(001) case is the same to that of the Ir(111) surface, both are 2.71 Å. These facts combine to give an overall lower magnon dispersion energy across the SBZ in the case of 2ML Co/1ML Fe/Ir(001) where at the high symmetry point the energy of the $n = 0$ mode does not exceed about 125 meV [110]. In the case of 2ML Co/1ML Fe/Ir(111) the expectation is that at the high symmetry point $\overline{\mathrm{K}}$, the $n = 0$ magnon energy will exceed 175 meV. Surprisingly the interlayer coupling between the Co layers is weaker in the 2ML Co/1ML Fe/Ir(111) system. It can be said for certain that the low exchange coupling constants are very complicated in this system as shown in Fig. 5.8. The effect of the Ir(111) is very important as the interface Fe layer hydridizes with the substrate.

At this point it is important to mention that the interface Fe layer was always annealed in the experiment. One has to be careful not to exceed a temperature of about 800K. This is because Fe can interlace with the Ir substrate at higher temperatures and shows a stable $\mathrm{Fe}_{0.5}/\mathrm{Ir}_{0.5}(111)$ alloy [52]. If for example, the interlacing did happen then the Fe interface layer would be much closer to the Ir atoms and therefore the effect of hybridization would

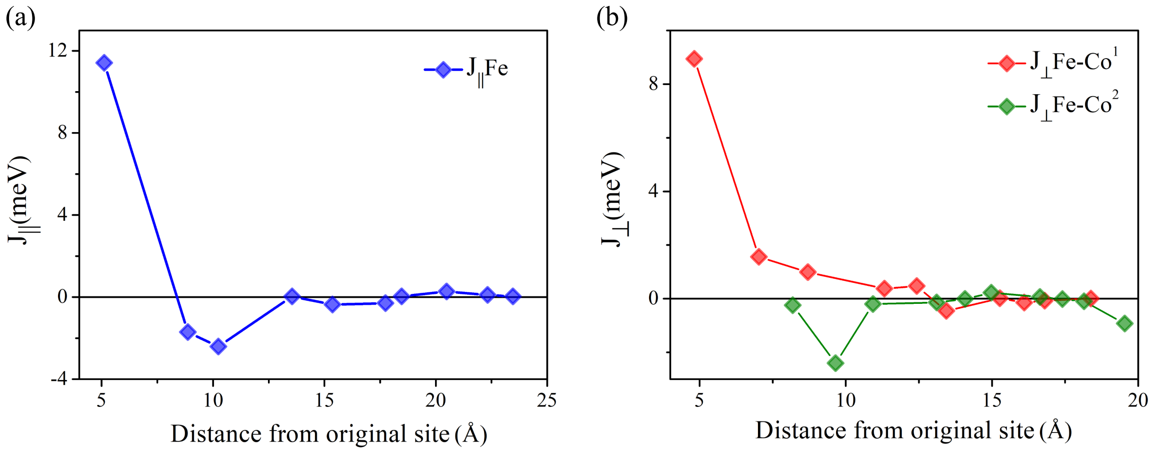

Figure 5.9: (a) Intralayer exchange coupling strength as a function of the distance from the original site. Values for up to 10 nearest neighbors are provided. (b) Interlayer exchange coupling strength between the interface Fe and Co overlayers as function of the distance from the original site. Values for up to 10 nearest neighbors are provided. All values for the low exchange coupling constants are given in meV.

be greater. This would affect the magnetic moment of the Fe atoms and reduce them when compared to the surface value [72, 112]. In that case, one would expect low magnon energies in the experiment when compared to the theoretical calculations. No deviation of the $n = 0$ magnon mode stemming from the Fe interface layer was observed. The observed LEED pattern showed very sharp diffraction spots, suggesting good pseudomorphic growth of interface Fe layer (see section 3.4.2 Fig. 3.20).

In order to see how much each atomic layer contributes to each magnon mode, the layer resolved transverse magnetic susceptibility has been calculated which gives the spatial distribution of each magnon mode over the Brillouin zone. This contains the magnon dispersion and allows one to compare the contribution of each atomic layer to each magnon mode because a spectral weight is assigned at every point in the dispersion. This spectral weight is called the Bloch spectral function. The results for such a calculation in the free standing film of 2ML Co/1ML Fe/Ir(111) is given in Fig. 5.10. Indeed, the results indicate that the $n = 0$ magnon mode is localized in the interface Fe layer (Fig. 5.10(b)). The $n = 2$ magnon mode can be viewed as being partially localized in the middle Co layer (Fig. 5.10(c)) while the $n = 1$ mode having a contribution from the surface Co layer, while the same layer having the contribution to the $n = 2$ mode (Fig. 5.10(d)).

To complement the earlier investigated 2ML Co/1ML Fe/Ir(111), results obtained on 1ML Co/1ML Fe/Ir(111) are presented in Fig. 5.11. As a starting point for the calculated fits in Fig. 5.11, exchange coupling constants were taken from *ab initio* calculations for 2ML Co/1ML Fe/Ir(111) shown later in Fig. 5.6. Since there is no data available for the $n = 1$ mode, we only discuss the exchange coupling constants in the interface Fe. The calculated $n = 1$ mode may be very different and no comment can be made about the exchange coupling patter for this magnon band. The exchange coupling constants in the

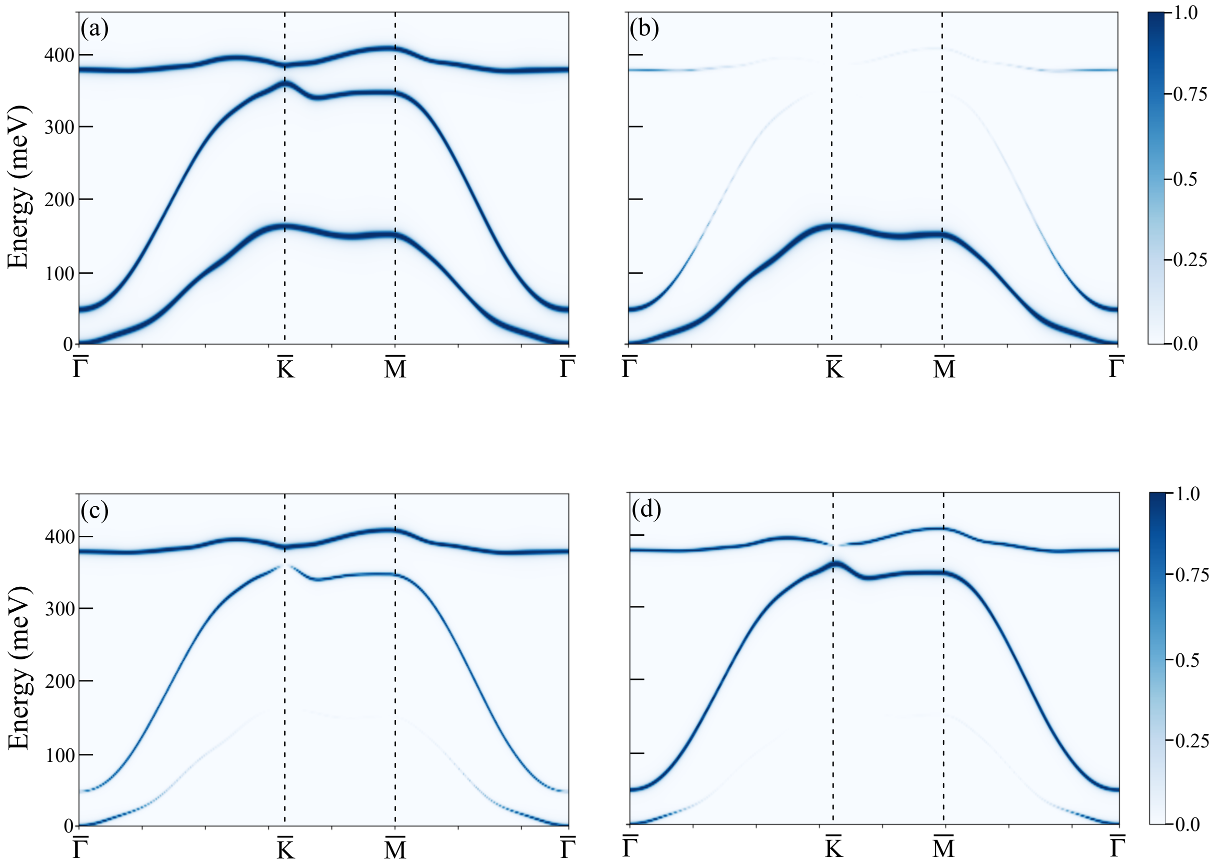

Figure 5.10: (a) The total susceptibility Bloch spectral function projected into all layers. (b) The susceptibility Bloch spectral function projected into the interface Fe layer. (c) The susceptibility Bloch spectral function projected into the middle Co layer. (d) The susceptibility Bloch spectral function projected into the surface Co layer. The calculations were performed by Khalil Zakeri with the code obtained from Arthur Ernst.

interface all slightly increase when compared to the 2ML Co/1ML Fe/Ir(111) system. For $J_{N\parallel}$ the increase is by a factor of 1.3. The ratio of exchange coupling constants for $J_{N\parallel}$ and $J_{N\perp}$ were kept the same in this system compared to the 2ML Co/1ML Fe/Ir(111) Fe-Co^2. When compared to the 2ML Co/1ML Fe/Ir(111) the interlayer exchange coupling constant $J_{N\perp}$ increased by a factor of 1.5. Only the nearest neighbor terms are discussed here since they are by far the leading terms in the dispersion. The values of $J_{N\parallel}$ and $J_{N\perp}$ may be different once experimental data for the $n = 1$ is obtained. However, the general finding is that the interlayer coupling between the Fe and Co is weaker than the intralayer coupling of the Fe atoms in the Fe-Ir(111) interface. This points to the general trend that adding a third layer of Co on top will affect the spin density in the middle Co layer and weaken the interlayer coupling between the interface Fe layer and the Co overlayer.

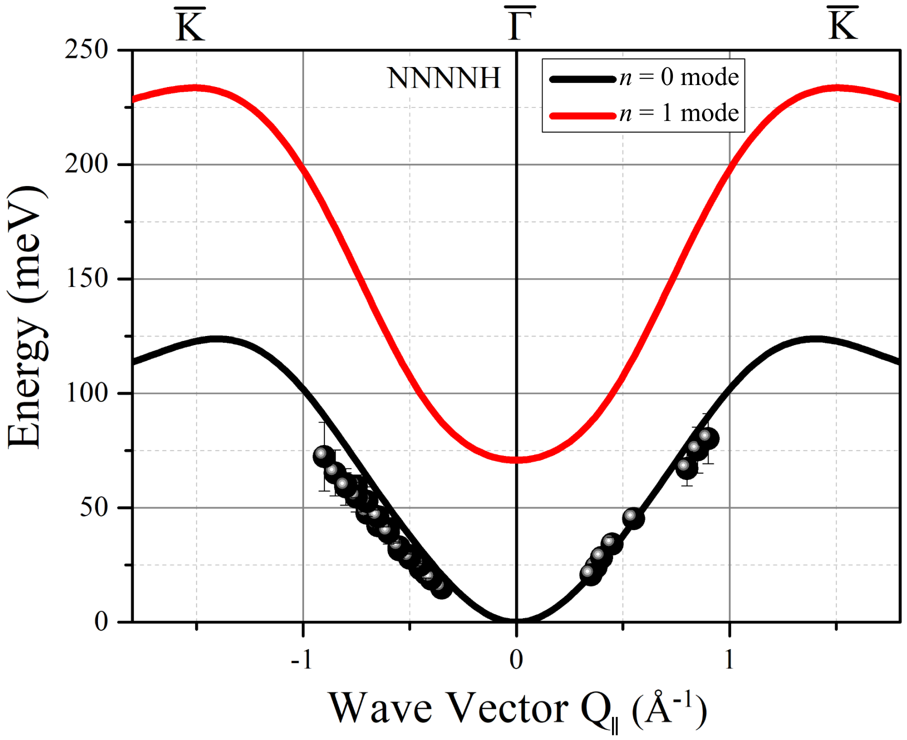

Figure 5.11: The $n = 0$ magnon mode dispersion on 1ML Co/1ML Fe/Ir(111). Experimental data is represented by the black spheres. The calculated magnon dispersion is numerically done in the NNNNH model (black curve $n = 0$ mode, red curve $n = 1$ mode). The exchange coupling constants used in the dispersion calculations for the interface Fe layer are $J_{N\|} = 5.7$ meV, $J_{NN\|} =$ -0.7 meV and $J_{NNN\|} =$ -0.9 meV. The exchange coupling constants used in the dispersion calculations for the surface Co layer are $J_{N\|} = 11.2$ meV, $J_{NN\|} = 1$ meV and $J_{NNN\|} =$ -0.2 meV. The interlayer exchange coupling constants used in the dispersion calculations are $J_{N\perp} =$ 4.9 meV, $J_{NN\perp} = 0.6$ meV and $J_{NNN\perp} = 0.2$ meV.

5.2 Antisymmetric exchange (Dzyaloshinskii-Moriya interaction)

In section 2.2 the antisymmetric DMI was introduced. It was said that in the presence of broken inversion symmetry and a large SOC in the system, this antisymmetric exchange interaction arises. Later, in the experimental results section 4.2 it was seen that the DMI has a large effect on the magnon dispersion in the 1ML Co/1ML Fe/W(110) system. Specifically, it was found that due to the orientation and magnitude of the DMI vectors in the different species of materials deposited, the asymmetry in the magnon dispersion was giant, i.e. by far the largest observed up to that point in time. Another promising candidate for showing the DMI effect on the magnon dispersion was investigated in this work, namely the 1MLCo/1ML Fe/Ir(111) and the 2ML Co/1ML Fe/Ir(111) system.

5.2.1 1ML Co/1ML Fe/Ir(111)

As a first step in investigating the 1ML Co/1ML Fe/Ir(111) system, the direction of the DM vectors are derived using the Levy Fert model for surfaces in the so called three site interaction introduced in Eq. 2.34 in section 2.2.1. In Fig. 5.12 the longitudinal components of the Fe intralayer DM vectors and interlayer Fe-Co are presented up to the second nearest neighbor. For simplicity and clarity of the Figure the first two layers are shown but this can be easily extended up to 3 or more layers in same fashion. Experimental investigation of this is challenging because of the complex magnetic state of this system. A monolayer of Fe grown on Ir(111) is not ferromagnetic at room temperature. The sign of ferromagnetism only appears after 3 ML [12]. A monolayer of Co deposited on the Ir(111) substrate is not ferromagnetic at room temperature either, exhibiting a large contribution of both in and out of plane magnetization up to and above 4 ML [40]. When a bilayer structure of 1ML Co/1ML Fe was deposited on Ir(111), using longitudinal MOKE there appeared a weak but very well defined ferromagnetic signal. An example comparing the weak ferromagnetic signal of 1ML Co/1ML Fe/Ir(111) to that of a thicker 2ML Co/1ML Fe/Ir(111) is presented in Fig. 5.13. One can notice that the ferromagnetic signal is well defined in the bilayer example. The indication is that the quality of the film is very good, this is seen in both the extremely narrow coercivity for both films in Fig. 5.13. This also indicates that the film is not a multidomain structure since it takes a very little magnetic field to flip the magnetization of the film. Also, the MOKE setup used is also sensitive to other components of of magnetization not just the parallel to the plane of the film one and so it is possible that what is being measured is the inplane and possible out of plane component of the film. This is plausible as Co films on Ir(111) have an out of plane magnetization [11, 40]. Therefore this would point to the fact that either the magnetic state of the sample is not a simply magnetically in plane or that there may be a component of magnetization that is not sensitive to longitudinal MOKE. This makes

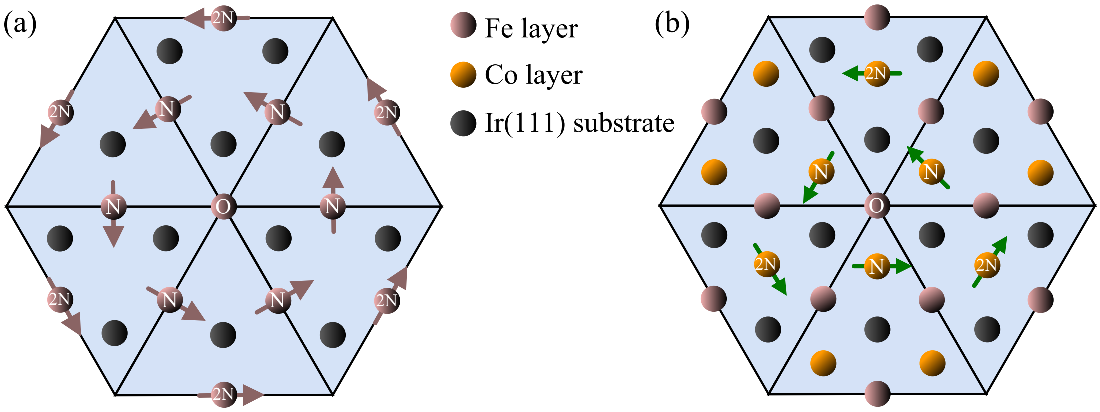

Figure 5.12: (a) Longitudinal component of the DM vectors for nearest (N) and next nearest (2N) neighbors in the Fe interface layer. (b) Longitudinal component of the interlayer DM vectors for the nearest (N) and next nearest (2N) between the interface Fe layer and the first Co layer.

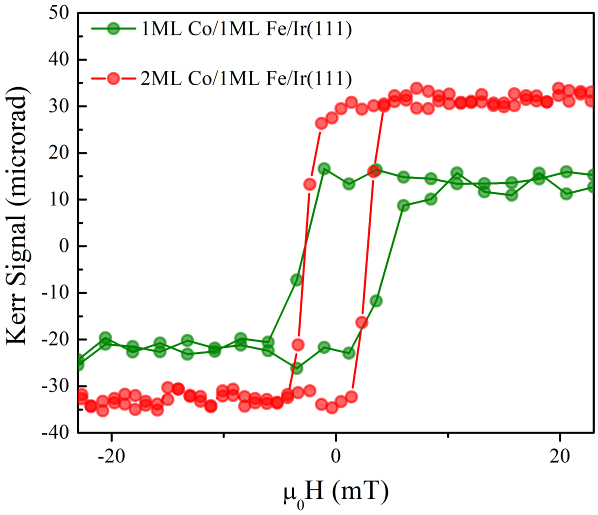

Figure 5.13: Kerr ellipticity for 1ML Co/1ML Fe/Ir(111) (green) and 2ML Co/1ML Fe/Ir(111) (red). Measurements performed in longitudinal MOKE geometry.

SPEELS measurements more difficult if one wants to investigate spin resolved excitations. This is because when a magnon is created during a scattering process, the difference in the scattered electron beam intensity represents the magnon and gives all the necessary information about it. If the film magnetization is not mostly parallel or antiparallel to the incoming polarized electron beam, then the polarized electron beam will excite a magnon in both spin channels and the peak in the difference spectra of the scattered electron beam will be reduced. An example of non spin resolved magnon excitations was shown in in the work of Hjelt in our group [40].

Therefore due to very low magnon peak intensities it was not possible to perform a detailed analysis on the DMI energy splitting.

5.2.2 2ML Co/1ML Fe/Ir(111)

Another system where the DMI was investigated was the 2ML Co/1ML Fe/Ir(111). In order to experimentally investigate the DM vectors which are included in the strength of the DMI energy splitting (Eq. 2.35), a series of time inversion experiments have been performed. This is where the inplane magnetization of the film is reversed thus reversing the propagation direction of magnons without changing the scattering geometry. As mentioned before, if the DMI is significant then there should be a pronounced energy asymmetry in the magnon spectrum, i.e. $\Delta E = E_{\mathbf{M}}(Q) \neq E_{\text{-}\mathbf{M}}(Q)$. In this context a series of SPEELS difference spectra is presented in Fig. 5.14. We notice that in general for this system the intensity of the scattered electron beam for the magnon signal is low when compared to other systems (see chapter 4.). This makes the range of wavevectors that can be investigated for the DMI splitting very limited. There are however cases where the magnon energy is clearly represented such as in Fig. 5.14(b) for $\mathbf{M}[11\bar{2}]$ (red

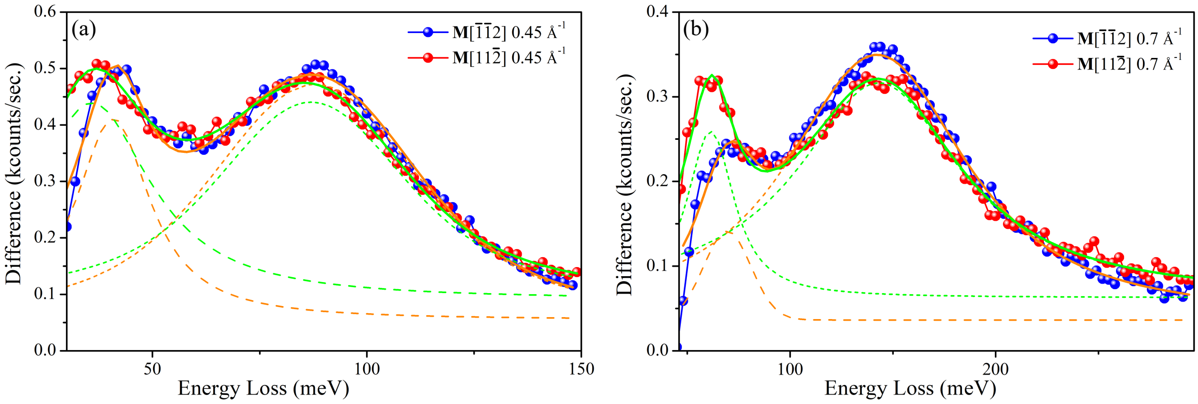

Figure 5.14: (a) Series of SPEELS difference spectra recorded for different wave vectors Q: (a) 0.45, (b) 0.7 Å^{-1}. The spectra are recorded for two cases; **M**[$\bar{1}\bar{1}2$] (blue spheres) and **M**[$11\bar{2}$] (red spheres). The solid lines are the total fit to the experimental data. The total fits are comprised of two Voigt function fits, where the $n = 0$ mode is represented by a dashed line and the $n = 1$ mode is represented by a short dashed line.

spheres). Another reason why ΔE is difficult to obtain is because, here we are effectively dealing with a 3ML system. SPEELS is a surface sensitive technique, and while one may still probe the interface mode in such a 3ML system, at such a low incident energy being fully sensitive to the interface Fe layer may prove difficult. The true penetration depth of the electron will also depend on the type of material that it is being scattered from. Therefore since the DMI energy splitting is possibly on the order of up to 10 meV and it is an interface effect as seen in chapter 4 and in Ref. [104], ultimate data quality is important. Analysis of various available wave vectors still give a value for the DMI energy splitting which is done below. From previous studies on the interfacial DMI, the most significant contribution to the strength of DM vectors comes from atomic layers closest to the substrate. This makes sense if one looks at the Levy-Fert model (Eq. 2.34) where the three site interaction implies that the strongest atomistic D_{ij}'s are the ones closest to the substrate. Also, it was observed that in a number of studies on ultrathin atomic layers a large contribution of the DM vectors come from the first few layers and for the most part significantly decreases with increasing neighbor distance [42, 86, 93, 97]. Therefore one can start with the assumption that the magnitude of the DM vectors will be most significant in the first or first two layers of the present 2ML Co/1ML Fe/Ir(111) system being studied. Following Eq. 2.35, the magnon dispersion asymmetry for a 2ML fcc(111) slab of film is given by

$$\Delta \mathrm{E} = 8\mathcal{D}^{x}_{1\parallel}\sin(\frac{1}{2}\mathrm{Q}_{\parallel}a) + 4\mathcal{D}^{x}_{1\parallel}\sin(\mathrm{Q}_{\parallel}a) + 4\mathcal{D}_{1\perp}\sin(\frac{1}{2}\mathrm{Q}_{\parallel}a) + 8\mathcal{D}^{x}_{2\parallel}\sin(\frac{3}{2}\mathrm{Q}_{\parallel}a) + 4\mathcal{D}_{2\perp}\sin(\mathrm{Q}_{\parallel}a) \tag{5.2}$$

where the subscript 1 stands for nearest neighbor, a is the nearest neighboring atomic distance,x signifies the intralayer component of the DM vectors and

$\mathcal{D}^x_{1\|} = \frac{1}{2}\left(D^x_{1\|}\lfloor layer\,1 + D^x_{1\|}\lfloor layer\,2\right)$, $\mathcal{D}^x_{2\|} = \frac{1}{2}\left(D^x_{2\|}\lfloor layer\,1 + D^x_{2\|}\lfloor layer\,2\right)$, the $\|$ symbol indicates a longitudinal DM component to the magnon propagation direction. Similar formalism is used for $\mathcal{D}_{1\perp}$ and $\mathcal{D}_{2\perp}$. The factor $\frac{1}{2}$ comes from the fact that we only count the DMI contributions from the first two layers and therefore have to average over the individual $\mathcal{D}^x$ components. In the case where there are two layers considered separately and each layer contributions are summed over the crystal unit cell in Eq.(5.2), the new terms are $\mathcal{D}^x_{\|} = \left(D^x_{\|}\lfloor layer\,1 + D^x_{\|}\lfloor layer\,2\right)$. The factor $\frac{1}{2}$ is now not there since the DMI contribution of each layer is taken into account separately and each $\mathcal{D}^x$ prefactor in Eq.(5.2) is multiplied by 2. The quantities that are measured in the SPEELS experiment are the longitudinal component of the $\mathcal{D}$, each individual contribution to these has to be extracted.

Before interpreting the DM vector values used in Eq.(5.2) and their physical meaning we will discuss the growth of the film. The structure of the film is essential to understand the magnitude and orientation of the DM vectors. The Fe monolayer has been reported to grow pseudomorphically on the Ir(111) substrate in the fcc packing and in certain cases in the hcp stacking [22, 34, 44]. It was also reported that when a monolayer of Fe is deposited on Ir(111) and annealed between 750 - 800 K, a surface with a c(2×4) is observed. However at higher temperatures, above 800 K, the pseudomorphic p(1×1) structure is retained [52]. For the samples investigated in this work, the interface Fe layer was annealed with a very low power of about 2 Watts, as a results no such surface reconstruction was observed. In section 3.4.1, LEED images obtained on 2ML Co/1ML Fe/Ir(111) were presented in Fig. 3.22. If the c(2×4) structure was present it should have shown up at least as some weak features in the LEED images. However since no such features were observed, we assume an fcc stacking here and pseudomorphic growth of the Fe interface layer. Furthermore, it was reported that the Fe monolayer will have a 9% strain on the Ir(111) substarte [3].

In Ref. [86] in a bilayer sample of 1ML Pd/1ML Fe/Ir(111) the interface Fe layer DM vector $D^x_{1\|\lfloor \mathrm{Fe}}$ was derived to be 0.8 meV, $D^x_{2\|\lfloor \mathrm{Fe}} = 0.4$ meV, $D_{1\perp} = 0.41$ meV and $D^x_{1,2\|\lfloor \mathrm{Fe}} \gg D_{1,2\perp}$. In Ref. [22] it was reported that in a 2ML Fe/Ir(111) system, under an fcc ABCBA type stacking condition, the next nearest neighbor DM vector in the interface Fe on Ir(111) can be negative and the third next nearest neighbor can be at least twice larger in value than the second nearest neighbor. However, this configuration was the thermodynamical ground state. In another study on 1ML Co/Ir$_n$/Pt(111) the magnitude of the DM vectors in the Co layer was derived by varying the thickness of the Ir spacer layers [97]. For a thick enough Ir spacer layer, as far as SPEELS is concerned the sample would be 1ML Co/Ir(111). For the largest thickness of the Ir spacer of 6ML of Ir on Pt(111), the 1ML Co exhibited a surprising calculated DM vector strength $D^x_{1\|\lfloor \mathrm{Co}} = 0$ meV and $D^x_{2\|\lfloor \mathrm{Co}} =$ 0.6 meV. This assumed fcc stacking which has been reported for ultrathin Co films grown on Ir(111) [11, 57]. Since the Co film in [97] was next to the Ir spacing layers and in this work it is relatively far away (second and third layer $\approx$ 2 and 4 Å spacing), it is reasonable to assume that the DM vectors would be much smaller in our case. Therefore we may also assume that the DM vectors have their value largely from the Fe-Ir(111) interface. Also,

the small Co DM vector values were taken here as reported in [97]. In that work only the next nearest neighbor DM vector values had a significant value however this was for a Co layer next to the Ir(111) substrate and in our case the Co layer is not the interface layer and is further away from the Ir(111) substrate. Therefore, one would suspect that the DM vectors are small. Equation 5.2 can easily be extended to more nearest neighbors, below the third nearest neighbor approximation is used for some of the analysis.
It is emphasized that in Fig. 5.15(a)-(b), the experimental results represent the total values of DM vectors, i.e. $\mathcal{D}^x_{1\|}$, $\mathcal{D}^x_{2\|}$, etc. The individual component of the DM vectors coming from different layers is not uniquely determined but has to be extracted. In this framework, various approaches have been taken to analyze the data and are given below.

Approach 1: In Fig. 5.15(a) we fit the experimental results taking into account only the total DM vectors $\mathcal{D}^x_{1\|}$, $\mathcal{D}^x_{2\|}$ and $\mathcal{D}_{1\perp}$, no comment is made on the components of the DM vectors from different layers. The $\mathcal{D}_{2\perp}$ is assumed to be negligible, which is reasonable to assume with what is already known from literature. The fitting values used in Fig. 5.15(a) are $\mathcal{D}^x_{1\|} = \frac{1}{2}\left(D^x_{1\|\lfloor \mathrm{Fe}} + D^x_{1\|\lfloor \mathrm{Co}}\right)$ =0.8 meV, $\mathcal{D}^x_{2\|} = \frac{1}{2}\left(D^x_{2\|\lfloor \mathrm{Fe}} + D^x_{2\|\lfloor \mathrm{Co}}\right)$ = -0.64 meV, $\mathcal{D}_{1\perp} = 0.2$ meV. The standout feature here is that the next nearest DM vector $\mathcal{D}^x_{2\|}$ is large in magnitude relative to $\mathcal{D}^x_{1\|}$ and negative in sign. This is completely opposite to what is implied in the literature mentioned above for elemental Fe and Co films. However, one has to take care when using the values reported since they are usually given as a magnitude and no sign is implied from them. This aproach implies that the effective contribution of each layer leads to a large negative next neighbor contribution to the DM vectors. The experimental results in Fig. 5.15(a) were plotted and compared to the derived DMI dispersion ΔE by taking the total contribution of the DM vector values mentioned above.

Approach 2: In Fig. 5.15(b) we fit the experimental results assuming no perpendicular DM component $\mathcal{D}_{\perp}$ to reduce the number of free parameters that can be adjusted. Under that assumption the derived energy splitting ΔE had an even better fit than in the previous case. This is shown in Fig. 5.15(b). The fitting parameters used in this case are $\mathcal{D}^x_{1\|} = 0.82$ meV and $\mathcal{D}^x_{2\|} =$ -0.54 meV. The value of $\mathcal{D}^x_{1\|}$ agrees well with the one reported in [86] assuming that the total DM vector $\mathcal{D}^x_{1\|}$ magnitude is that of the Fe interface layer. Note, in our analysis the value of $\mathcal{D}^x_{2\|}$ is still comparable to $D^x_{1\|\lfloor \mathrm{Fe}}$. This approach to data analysis would indicate that the DMI has a negligible component of $\mathcal{D}^x_{\perp}$ DM vectors with a large $\mathcal{D}^x_{2\|}$ component.

Both of the above approaches have validity to them, and both seem to indicate that the DMI has a large contribution for next nearest neighbors. Even if one assumes a special fcc stacking reported above, the magnitude of the value implied by the experiment is far too large. It was reported that after a second Fe layer is deposited on the 1ML Fe/Ir(111), there is a film reconstruction with patches of bcc like growth [22], however as already mentioned the LEED images indicated that this was not the case in this work.

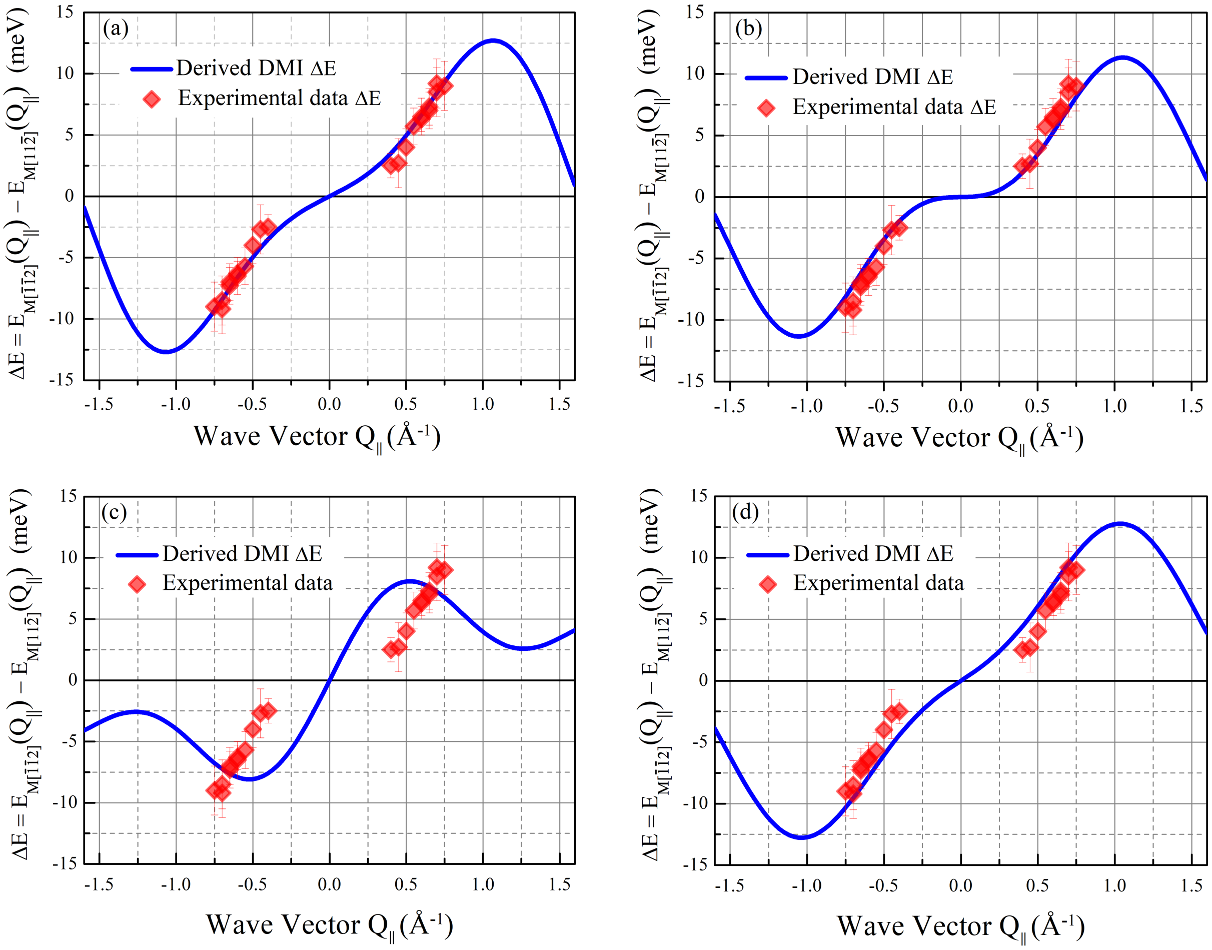

Figure 5.15: The energy asymmetry ΔE of the $n = 0$ magnon mode measured in 2ML Co/1ML Fe/Ir(111). ΔE is measured by recording the spectra at a fixed Q and by reversing the direction of $\mathbf{M}$. (a) The energy asymmetry ΔE with the fitting parameters $\mathcal{D}^x_{1\parallel} = \frac{1}{2}\left(D^x_{1\parallel\lfloor\mathrm{Fe}} + D^x_{1\parallel\lfloor\mathrm{Co}}\right) = 0.8$ meV, $\mathcal{D}^x_{2\parallel} = \frac{1}{2}\left(D^x_{2\parallel\lfloor\mathrm{Fe}} + D^x_{2\parallel\lfloor\mathrm{Co}}\right) =$ -0.64 meV, $\mathcal{D}_{1\perp} = 0.2$ meV. (b) $\mathcal{D}^x_{1\parallel} = \frac{1}{2}\left(D^x_{1\parallel\lfloor\mathrm{Fe}} + D^x_{1\parallel\lfloor\mathrm{Co}}\right) =$ 0.82 meV, $\mathcal{D}^x_{2\parallel} = \frac{1}{2}\left(D^x_{2\parallel\lfloor\mathrm{Fe}} + D^x_{2\parallel\lfloor\mathrm{Co}}\right) =$ -0.54 meV. (c) $\mathcal{D}^x_{1\parallel} = \frac{1}{2}\left(D^x_{1\parallel\lfloor\mathrm{Fe}} + D^x_{1\parallel\lfloor\mathrm{Co}}\right) = \frac{1}{2}(1.6 - 0.4) = 0.6$ meV, $\mathcal{D}^x_{2\parallel} = \frac{1}{2}\left(D^x_{2\parallel\lfloor\mathrm{Fe}} + D^x_{2\parallel\lfloor\mathrm{Co}}\right) = \frac{1}{2}(1.58 - 0.8) = 0.39$ meV, $\mathcal{D}_{1\perp} = 0.28$ meV and $\mathcal{D}_{2\perp} =$ -0.2 meV (d) $\mathcal{D}^x_{1\parallel} = \frac{1}{2}\left(D^x_{1\parallel\lfloor\mathrm{Fe}} + D^x_{1\parallel\lfloor\mathrm{Co}}\right) = \frac{1}{2}(1.6 + 0.4) = 1.0$ meV, $\mathcal{D}^x_{2\parallel} = \frac{1}{2}\left(D^x_{2\parallel\lfloor\mathrm{Fe}} + D^x_{2\parallel\lfloor\mathrm{Co}}\right) = \frac{1}{2}(-1.58 + 0.8) =$ -0.39 meV, $\mathcal{D}_{1\perp} = 0.28$ meV and $\mathcal{D}_{2\perp} =$ -0.2.

In the trilayer films of 2ML Co/1ML Fe/Ir(111) we may suspect that the film also does not grow pseudomorphically for the Co overlayers. In LEED images from section 3.4.2 Fig. 3.22(c),(d), the diffraction spots are not sharp and show satellite features indicating that the Co film growth is not fully pseudomorphic which would imply strain relief of the film. This structural effect may be the cause of the modification of the DM values in the Fe interface. However, a more detailed theoretical study would need to be performed.

Approach 3: In order to check the sign of the atomistic DM vectors we can start with the sign of DM vectors that are unknown from literature being negative, namely $D^{x}_{2\|\lfloor\mathrm{Fe}}$. Correspondingly we also set the sign of $D^{x}_{2\|\lfloor\mathrm{Co}}$ to minus. The results is plotted in Fig. 5.15(c). The agreement of the derived curve to the experimental data is poor. This further suggests that not only is $D^{x}_{2\|\lfloor\mathrm{Fe}}$ significant in value but also that it is negative in sign which has so far been unknown in a layered structure of 2ML Co/1ML Fe grown on Ir(111). Another possibility in our analysis is to have the $D^{x}_{2\|\lfloor\mathrm{Co}}$ have a large magnitude value e.g. ~ 0.8 meV, and $D^{x}_{2\|\lfloor\mathrm{Fe}}$ have a very small magnitude e.g. ~ 0.1 mev. In the case of $D^{x}_{2\|\lfloor\mathrm{Fe}}$ this may be plausible as reported in [22], however in the case of $D^{x}_{2\|\lfloor\mathrm{Co}}$ this is a completely unrealistic value especially given the fact that the Co layer is relatively far away from the Ir(111) substrate.

Approach 4: We may take an approach where we try to assign a DM vector contribution to each layer. We take similar values, already mentioned in literature and assume the next nearest DM vector contribution $D^{x}_{2\|\lfloor\mathrm{Co}} = 0.8$ meV, given that the nearest neighbor DM vector in Co/Ir(111) are smaller compared to next nearest neighbor ones and fcc stacking as reported in [97]. Taking the value from literature mentioned above for the interface Fe layer and the Co overlayer, we plot the results in Fig. 5.15(d). Here the agreement with the data is very good. The major assumptions were that the atomistic DM vectors $D^{x}_{1\|\lfloor\mathrm{Fe}} = 1.6$, $D^{x}_{2\|\lfloor\mathrm{Fe}} = -1.58$, $D^{x}_{1\|\lfloor\mathrm{Co}} = 0.4$ and $D^{x}_{2\|\lfloor\mathrm{Co}} = 0.8$. However, nothing has been found in literature that would justify the next nearest neighbor $D^{x}_{2\|\lfloor\mathrm{Fe}}$ having a large negative sign in the Fe interface layer. Note, the value for $D^{x}_{1\|\lfloor\mathrm{Fe}}$ reported in [22] is 1.3 meV which is somewhat different to the one here of 1.6 meV that was used a fitting parameter. This difference can be from the fact that the interfacial DMI values in [22] were derived based on the 2ML Fe/Ir(111) system while we have a 2ML Co/1ML Fe/Ir(111). For some systems such as 1ML Co/1ML Fe/W(110), by depositing a 1ML of Co on top of a ML of Fe, the DMI was strongly enhanced [93]. The same effect is not observed here. One has to be careful in the definition of the DM vector values. Depending on how the starting Hamiltonian is defined, i.e. if there is a prefactor of 1/2, the value can differ by a factor of two. This has been taken into consideration in this analysis. For the fitting values in Fig. 5.15(c),(d) up to 10% relaxed film was assumed. This is a reasonable assumption since the films were gently annealed as already mentioned.

All of the above mentioned variations of the DM vector analysis is given in Tab. 5.2(for

$\mathcal{D}^x_{1,2\|}$,$\mathcal{D}^x_{1,2\perp}$) and Tab.5.1(for $D^x_{1,2\|}$,$D^x_{1,2\perp}$) with the largest contributing terms presented.

Other variations of the analysis are possible but the implication is the same. The experimental data strongly suggests that the next nearest neighbor DM vectors in the interface Fe layer $D^x_{2\|\lfloor\mathrm{Fe}}$ is large and comparable to the nearest neighbor $D^x_{1\|\lfloor\mathrm{Fe}}$, i.e. ∼ 0.54 - 1.58 meV and has a negative sign. This is a possible scenario, as it is emphasized again that it was already observed that the the Co overlayers on top of Fe can modify the DM vectors in some systems, e.g. enhances them for the case of 1ML Co/1ML Fe/ W(110) [93]. Moreover, the DM vectors originating within the Co layers should be smaller from the ones reported in literature since in our case it is not the interface layer but comprises the second and third layers.

Table 5.1: Total DM vector components for different analysis assuming non-zero DM vector values in (a) Fe intralayer and Fe-Co interlayer (b) Fe intralayer. All values are given in meV.

Graph	$\mathcal{D}^x_{1\|}$	$\mathcal{D}^x_{2\|}$	$\mathcal{D}_{1\perp}$	$\mathcal{D}^x_{2\perp}$
(a)	0.8	-0.64	0.2	0
(b)	0.82	-0.54	0	0

Table 5.2: Atomistic DM vector components for different analysis assuming non-zero DM vector values in (c) Fe and Co itralayer, Fe-Co interlayer and (d) Fe and Co itralayer opposite in sign to those in (c), Fe-Co interlayer. All values are given in meV.

Graph	$D^x_{1\|\lfloor\mathrm{Fe}}$	$D^x_{2\|\lfloor\mathrm{Fe}}$	$D_{1\perp\lfloor\mathrm{Fe-Co}}$	$D_{2\perp\lfloor\mathrm{Fe-Co}}$	$D^x_{1\|\lfloor\mathrm{Co}}$	$D^x_{2\|\lfloor\mathrm{Co}}$
(c)	1.6	1.58	0.28	-0.2	-0.4	-0.8
(d)	1.6	-1.58	0.28	-0.2	0.4	0.8

5.3 Summary

In summary, for the 2ML, 3ML Fe/Ir(111) the *ab initio* calculations performed on the 2ML, 3ML Fe/Ir(111) had to be normalized by the Fe magnetic moment of the Fe-Ir(111) interface in order to achieve agreement with results. In the case of 3ML Fe/Ir(111), a very soft $n = 1$ magnon band was observed and correspondingly very low group velocity when compared to the 2ML Fe/W(110). In the 2ML Fe/Ir(111) system, the $n = 0$ magnon band was found to be stiffer when compared to the 3ML Fe case on the same substrate. The finding of the corresponding weaker exchange coupling constants in the 3ML Fe case was attributed to the spin density redistribution to the third extra surface layer. In the case of 2ML Co/1ML Fe/Ir(111), the *ab intio* calculations were performed assuming a decreased exchange splitting of 0.8 meV between the majority and minority electron bands.

Performing time reversal experiments on 2ML Co/1ML Fe/Ir(111) revealed that the experimental data strongly suggests that the itralayer next nearest DM vector in the Fe interface layer has a comparable magnitude to the nearest neighbor but the opposite sign. In the 1ML Co/1ML Fe/Ir(111) system the interlayer ($J_{N\perp} = 4.9$ meV) coupling between the interface Fe layer and the surface Co layer was found to be weaker than the intralayer Fe exchange coupling ($J_{N\parallel} = 5.7$ meV). This re-enforced the earlier finding on the Co/Fe/W(110) system that showed a general trend of weak Fe-Co interlayer exchange coupling.

Ab initio calculations revealed a complex pattern of exchange constants for all of the systems investigated.

6. Conclusion and Outlook

In this work using spin polarized high resolution electron energy loss spectroscopy, high wavevector magnons were studied in 1ML Co/1ML Fe bilayer and 2ML Co/1ML Fe along with 1ML Co/2ML Fe trilayer structures on W(110). In the case of the 1ML Co/1ML Fe bilayer, besides the $n = 0$ magnon mode, the $n = 1$ magnon mode was observed associated with the confined modes in the film. The measured magnon dispersion relation was described within the next nearest neighbor Heisenberg model. A comparison with the previously studied 1ML Fe and 2ML Fe on the same substrate reveals that the intralayer exchange coupling $J_{\parallel}^{\mathrm{Fe}}$ is reduced by 27% relative to the 2ML Fe/W(110) but increased by a factor of 1.8 relative to the 1ML Fe/W(110). Surprisingly the interlayer exchange coupling constants $J_{\perp}^{\mathrm{Fe-Co}} = 4.5$ meV, were found to be much lower than the ones in the 2ML Fe system. This effect is associated with the Co layer meditated intralayer exchange constant.

In the trilayer system 1ML Co/2ML Fe, analysis of experimental data revealed an enhancement of the Fe intralayer exchange constants by nearly a factor of 2 compared to the 2ML Fe/W(110). The coupling of the middle Fe layer was found to be weakly coupled to the top Co layer with the value of $J_{\perp}^{\mathrm{Fe-Co}} = 4.5$ meV, just as in the case of 1ML Co/1ML Fe/W(110). This showed a general trend that the Co layer couples only weakly to the Fe layers but enhances the Fe intralayer exchange.

The antisymmetric Dzyaloshinskii-Moriya interaction was observed in the bilayer films of 1ML Co/1ML Fe/W(110). The effect was termed a giant effect since up to that point it was the largest recorded. Compared to the 2ML Fe/W(110) the nearest and next nearest values of the DM vectors were increased by a factor of 1.8 and 1.5, respectively. This is due to the small magntitude of the DM vectors in the Co layer and an enhancement of the Fe DM vectors at the interface. This showed that the DMI in this system is mainly an interfacial effect.

Elemental films of Fe on Ir(111) were investigated along with 1ML Co/1ML Fe bilayers and 2ML Co/1ML trilayers on Ir(111). In 2ML Fe/Ir(111), experiments were performed at T = 13 K. Only a very soft $n = 0$ magnon mode was observed with the energy not exceeding above 85 meV. *Ab intiio* calculations were not able to describe the experimental data. A strong normalization of the exchange constants was needed to get a good agreement with the experimental data.

Measurements on 3ML Fe/Ir(111) showed that the $n = 0$ magnon branch was relatively soft compared to other systems [110], indicating a very complex pattern of exchange constant with intra- and interlayer antiferromagnetic coupling present.

Fe films up to 17 ML were investigated. The experimental energy dispersion was compared with the calculated surface magnon mode within the semi-infinite crystal approximation. The results showed a softer magnon dispersion then in the bulk Fe. This suggests a re-

duction of the exchange constants in the thick Fe films compared to the bulk Fe values. The results also confirmed that the observed magnon mode in 2ML Fe/Ir(111) and 3ML Fe(111) was the interface mode.
Measurements performed on 1ML Co/1ML Fe/Ir(111) showed signs of enhancement of the intralayer(interlayer) exchange coupling constants $J_{N\|}(J_{N\perp})$ and weaker interlayer exchange coupling constant $J_{N\perp} = 4.9$ meV when compared to the trilayer 2ML Co/1ML Fe/Ir(111) system. However in the bilayer case, the $n = 1$ magnon mode could not be observed, whereas in the trilayer case the $n = 0$ mode and the $n = 1$ mode were clearly observed. The magnon dispersion of 2ML Co/1ML Fe/Ir(111) was described by *ab initio* calculations well, with the majority and minority spin bands splitting being renormalized.
Studies on 2ML Co/1ML Fe/Ir(111) were carried out to investigate the DMI in this system. Results showed that the experimental data can be described well by considering the Fe interface next nearest DM vectors $D_{2\|\lfloor\mathrm{Fe}}$ to be negative and with a value of approximately -1.58 meV. The analysis indicated that the DMI is mainly an interfacial effect.

It is worth noting that all measurements performed on 2ML-3ML/Ir(111) and 1ML Co/1ML Fe/Ir(111) showed a small magnon signal due to a weak ferromagnetic signal. SPEELS measurements were still sensitive to this and were able to resolve the magnon excitations well with excellent experimental resolution of 11-20 meV.

As an outlook for this study in layered films of Co and Fe on W(110), another system that should be investigated is the 2ML Co/1ML Fe/W(110). Weak interlayer exchange coupling between Fe and Co is expected similar to what was observed in this work. Following this trail, the other systems worth exploring would be various combinations of Fe and Co: 1ML Fe/1ML Co/W(110), 1ML Fe/1ML Co/1ML Fe/W(110). This would allow one to quantify a detailed picture of the exchange coupling constants in all of these systems when compared to each other.
For the elemental and multilayer films on Ir(111) system it would be worthy to investigate the magnon dispersion to the end of the SBZ which would require using higher incident electron energies. This would give greater details into the exchange couplings in the system. Studies to determine the strength of the DM vectors on various systems would be of great interest, e.g. 1ML Co/1ML Fe/Ir(111) and various other combinations on heavy metal substrates. Putting a non-magnetic spacer film between the substrate and the films would be of value to explore layer distance and structural effects on the exchange coupling constants. Time reversal investigations on these systems would provide information about the DMI.

7. Appendix

This chapter contains more specific information regarding calculations in different sections. In chapter 2, section 2.1.1, when calculating the dispersion relation for the bcc(110) and fc(111) surface, the equations are only valid assuming the intraplane coupling constants $J_{N,NN..\parallel}$ are the same in every layer and that the interplance coupling constants $J_{N,NN..\perp}$ are also the same between the layers. Furthermore, $J_{N,NN..\parallel}$ should be equal to $J_{N,NN..\perp}$. In summary, one cannot distinguish the exchange coupling constants between different layers. Therefore, all of the results modeled with a simple Heisenberg model, i.e. chapter 4 Fig. 4.2, 4.3, 4.4,4.6 and chapter 5 Fig. 5.4(a), 5.11 were done numerically.

7.1 A: Mathematical derivation of the surface mode of Fe slabs with an fcc(111) surface orientation

In chapter 5, section 5.1.1, the surface mode of a semi infinite fcc(111) crystal is calculated and plotted in Fig. 5.5 to compare to the experimental data. In the surface film of an fcc(111) structure, there are 6 intralyer nearest, next nearest and third next nearest neighbors. For the atomic layer underneath the surface layer there are 3 interlayer nearest, next nearest and third next nearest neighbors. Introducing the layer index n, where n = 1 stands for the surface layer, the spin wave amplitude in the first layer in the NNNNH model is given by Eq. 7.1,

$$\begin{aligned} n = 1 : \hbar A_1 = {} & 4J_{N\parallel}SA_1[3 - 2\cos(\frac{1}{2}\mathrm{Q}a) - \cos(\mathrm{Q}a)] + 8J_{NN\parallel}SA_1[1 - \cos(\frac{3}{2}\mathrm{Q}a)] + \\ & J_{NNN\parallel}SA_1[3 - 2\cos(\mathrm{Q}a) - \cos(2\mathrm{Q}a)] + 6J_{N\perp}SA_2 - 4J_{N\perp}S\cos(\frac{1}{2}\mathrm{Q}a)A_2 \\ & - 2J_{N\perp}SA_1 + 6J_{NN\perp}SA_1 - 2J_{NN\perp}SA_2 - 4J_{NN\perp}S\cos(\mathrm{Q}a)A_2 + \\ & 12J_{NNN\perp}SA_1 - 4J_{NNN\perp}S\cos(\frac{1}{2}\mathrm{Q}a)A_2 - \\ & 4J_{NNN\perp}S\cos(\mathrm{Q}a)A_2 - 4J_{NNN\perp}\cos(\frac{3}{2}\mathrm{Q}a)A_2 \end{aligned} \tag{7.1}$$

where a is the interatomic distance. Similarly we can also define

$$\begin{aligned}
n > 1 : \hbar A_n = {} & 4J_{N\|}SA_n[3 - 2\cos(\frac{1}{2}\mathrm{Q}a) - \cos(\mathrm{Q}a)] + 8J_{NN\|}SA_n[1 - \cos(\frac{3}{2}\mathrm{Q}a)] + \\
& 4J_{NNN\|}SA_n[3 - 2\cos(\mathrm{Q}a) - \cos(2Qa)] + 12J_{N\perp}SA_n - \\
& - 2J_{N\perp}SA_{n-1} - 4J_{N\perp}S\cos(\frac{1}{2}\mathrm{Q}a)A_{n-1} + 12J_{NN\perp}SA_n - 2J_{NN\perp}SA_{n-1} - \\
& 4J_{NN\perp}S\cos(\mathrm{Q}a)A_{n-1} + 24J_{NNN\perp}SA_n - 4J_{NNN\perp}S\cos(\frac{1}{2}\mathrm{Q}a)A_{n-1} - \\
& 4J_{NNN\perp}\cos(\mathrm{Q}a)A_{n-1} - 4J_{NNN\perp}S\cos(\frac{3}{2}\mathrm{Q}a)A_{n-1} - \\
& 2J_{N\perp}SA_{n+1} - 4J_{N\perp}S\cos(\frac{1}{2}\mathrm{Q}a)A_{n+1} - 2J_{NN\perp}SA_{n+1} - \\
& 4J_{NN\perp}S\cos(\mathrm{Q}a)A_{n+1} - 4J_{NNN\perp}S\cos(\frac{1}{2}\mathrm{Q}a)A_{n+1} - \\
& - 4J_{NNN\perp}\cos(\mathrm{Q}a)A_{n+1} - 4J_{NNN\perp}S\cos(\frac{3}{2}\mathrm{Q}a)A_{n+1}
\end{aligned} \tag{7.2}$$

These equations can be summarized in matrix form as

$$\begin{pmatrix} a & b & & & & 0 \\ b & c & b & & & \\ & b & c & b & & \\ & & b & c & . & \\ & & & . & . & . \\ 0 & & & & . & . \end{pmatrix} = \begin{pmatrix} A_1 \\ A_2 \\ A_3 \\ A_4 \\ . \\ . \end{pmatrix} \tag{7.3}$$

where c $= -\hbar\omega + 4J_{N\|}S[3 - 2\cos(\frac{1}{2}\mathrm{Q}a) - \cos(\mathrm{Q}a)] + 8J_{NN\|}S[1 - \cos(\frac{3}{2}\mathrm{Q}a)]\ 4J_{NNN\|}S[3 - 2\cos(\mathrm{Q}a) - \cos(2\mathrm{Q}a)] + 12J_{N\perp}S + 12J_{NN\perp}S + 24J_{NNN\perp}S$, b $= -4J_{N\perp}S\cos(\frac{1}{2}\mathrm{Q}a) - 4J_{NN\perp}S\cos(\mathrm{Q}a) - 4J_{NNN\perp}S\cos(\frac{1}{2}\mathrm{Q}a) - 4J_{NNN\perp}\cos(\mathrm{Q}a) - 4J_{NNN\perp}S\cos(\frac{3}{2}\mathrm{Q}a)$ and a $=$ c$\lfloor A_{n\perp}/2$. The system of equations has an infinite set of solutions, one of them being a surface magnon mode and the others being bulk magnon modes. The surface magnon mode decays into the bulk exponentially where $A_{n+1} = A_n\mathrm{e}^{-\alpha\frac{a}{2}}$, with the bulk magnon modes having $A_{n+1} = A_n\mathrm{e}^{\mathrm{i}\mathrm{Q}_\perp\frac{a}{2}}$ and $\mathrm{Q}_\perp$ being the wave vector perpendicular to the surface. Taking the surface magnon mode and the bulk magnon mode one obtains the solutions $\mathrm{e}^{-\alpha\frac{a}{2}} = \cos(\mathrm{Q}_\|a), \cos(\frac{1}{2}\mathrm{Q}_\|a)$ and $\cos(\frac{3}{2}\mathrm{Q}_\|a)$. This implies that the surface magnon mode is localized most at the Brillouin zone boundary since the above solutions depend on $\mathrm{Q}_\|$. The surface magnon mode solution can then be easily derived by solving the two equation system, Eq. 7.1 and Eq. 7.2. The result is then given by,

$$\begin{aligned}\hbar\omega = {} & 4J_{N\|}S[3-2\cos(\frac{1}{2}\mathrm{Q}a)-\cos(\mathrm{Q}a)]+8J_{NN\|}S[1-cos(\frac{3}{2}\mathrm{Q}a)]+\\ & 4J_{NNN\|}S[3-2\cos(\mathrm{Q}a)-cos(2\mathrm{Q}a)]+6J_NS-4J_{N\|}S\cos(\frac{1}{2}\mathrm{Q}a)\cos(\frac{1}{2}\mathrm{Q}a)-\\ & 2J_NS+6J_{NN\|}S-4J_{NN\|}S\cos(\mathrm{Q}a)\cos(\mathrm{Q}a)-2J_{NN\|}S+12J_{NNN\|}S-\\ & 4J_{NNN\|}S\cos(\frac{1}{2})\cos(\frac{1}{2})-4J_{NNN\|}S\cos(\mathrm{Q}a)\cos(Qa)-4J_{NNN\|}S\cos(\frac{3}{2}\mathrm{Q}a)\cos(\frac{3}{2}\mathrm{Q}a).\end{aligned} \tag{7.4}$$

The wave vector Q is assumed to be parallel to the magnon propagation direction.

Bibliography

[1] S. Andrieu et al. “Magnetic properties of body-centered tetragona iron/iridium superlattices”. In: *Journal of Magnetism and Magnetic Materials* 126.1-3 (Sept. 1993), pp. 349–351.

[2] R. L. Bell. *Negative electron affinity devices [by] R. L. Bell.* English. Clarendon Press Oxford, 1973, ix, 148 p.

[3] Kirsten von Bergmann et al. “Complex magnetism of the Fe monolayer on Ir(111)”. In: *New Journal of Physics* 9.10 (Oct. 2007), pp. 396–396.

[4] Lars Bergqvist et al. “Atomistic spin dynamics of low-dimensional magnets”. In: *Phys. Rev. B* 87 (14 Apr. 2013), p. 144401.

[5] Andreas Bettac et al. “Structure and magnetism of hcp(0001) and fcc(001) thin cobalt films on a clean and carbon-reconstructed W(110) surface”. In: *Surface Science* 454-456 (May 2000), pp. 936–941.

[6] S. Blundell. *Magnetism in Condensed Matter.* Oxford Master Series in Condensed Matter Physics 4. OUP Oxford, 2001. ISBN: 9780198505921.

[7] M. Bode et al. “Chiral magnetic order at surfaces driven by inversion asymmetry”. In: *Nature* 447.7141 (2007), pp. 190–193. ISSN: 1476-4687.

[8] Paweł Buczek, Arthur Ernst, and Leonid M. Sandratskii. “Different dimensionality trends in the Landau damping of magnons in iron, cobalt, and nickel: Time-dependent density functional study”. In: *Phys. Rev. B* 84 (17 Nov. 2011), p. 174418.

[9] Paweł Buczek, Arthur Ernst, and Leonid M. Sandratskii. “Interface Electronic Complexes and Landau Damping of Magnons in Ultrathin Magnets”. In: *Phys. Rev. Lett.* 106 (15 Apr. 2011), p. 157204.

[10] I. Carlomagno et al. “Co-Ir interface alloying induced by thermal annealing”. In: *Journal of Applied Physics* 120.19 (2016), p. 195302.

[11] Wen-Yuan Chan et al. “Enhancement of the polar coercive force for annealed Co/Ir(111) ultrathin films”. In: *Journal of the Korean Physical Society* 62.12 (June 2013), pp. 1945–1949.

[12] W. Chen et al. “Structure Related Magnetic Dead Layer for Ultrathin Fe/Ir(111) Films”. In: *IEEE Transactions on Magnetics* 50.1 (2014), pp. 1–4.

[13] Y.-J. Chen et al. "Group Velocity Engineering of Confined Ultrafast Magnons". In: *Phys. Rev. Lett.* 119 (26 Dec. 2017), p. 267201.

[14] T.-H. Chuang et al. "Impact of Atomic Structure on the Magnon Dispersion Relation: A Comparison Between Fe(111)/Au/W(110) and Fe(110)/W(110)". In: *Phys. Rev. Lett.* 109 (20 Nov. 2012), p. 207201.

[15] Tzu-Hung Chuang. "High wave-vector magnon excitations in ultrathin Fe(111) films grown on Au/W(110) and Fe(001) films grown on Ir(001)." PhD thesis. Martin-Luther-University Halle-Wittenberg, 2013.

[16] Larry A. Coldren, Scott W. Corzine, and Milan L. Mašanović. *Diode Lasers and Photonic Integrated Circuits*. John Wiley & Sons, Inc., Mar. 2012.

[17] A. T. Costa, R. B. Muniz, and D. L. Mills. "Theory of large-wave-vector spin waves in ultrathin ferromagnetic films: Sensitivity to electronic structure". In: *Phys. Rev. B* 70 (5 Aug. 2004), p. 054406.

[18] A. T. Costa, R. B. Muniz, and D. L. Mills. "Theory of spin excitations in Fe(110) multilayers". In: *Phys. Rev. B* 68 (22 Dec. 2003), p. 224435.

[19] M.G. Cottam. *Linear And Nonlinear Spin Waves In Magnetic Films And Superlattices*. Chapter 1, World Scientific Publishing Company, 1994. ISBN: 9789814505482.

[20] A. Crépieux and C. Lacroix. "Dzyaloshinsky–Moriya interactions induced by symmetry breaking at a surface". In: *Journal of Magnetism and Magnetic Materials* 182.3 (1998), pp. 341–349. ISSN: 0304-8853.

[21] P. Drescher et al. "Photoemission of spinpolarized electrons from strained GaAsP". In: *Applied Physics A* 63.2 (Aug. 1996), pp. 203–206. ISSN: 1432-0630.

[22] Melanie Dupé et al. "Stability and magnetic properties of Fe double layers on Ir (111)". In: *Phys. Rev. B* 98 (22 2018), p. 224415.

[23] I. E. Dzyalosinskij. "Thermodynamic theory of "weak" ferromagnetism in antiferromagnetic substances." English. In: *Sov. Phys., JETP* 5 (1957), pp. 1259–1272. ISSN: 0038-5646.

[24] D. M. Edwards and Nevill Francis Mott. "Spin waves in ferromagnetic metals". In: *Proceedings of the Royal Society of London. Series A. Mathematical and Physical Sciences* 269.1338 (1962), pp. 338–351.

[25] H. J. Elmers et al. "Magnetic Frustration in Ultrathin Fe Films". In: *Phys. Rev. Lett.* 75 (10 Sept. 1995), pp. 2031–2034.

[26] Hans-Joachim Elmers. "Ferromagnetic Monolayers". In: *International Journal of Modern Physics B* 09.24 (1995), pp. 3115–3180.

[27] M. Etzkorn et al. "High-wave-vector spin waves in ultrathin Co films on W(110)". In: *Phys. Rev. B* 72 (18 Nov. 2005), p. 184420.

[28] Markus Etzkorn. “Spin Waves With High Energy And Momentum In Ultrathin Co-films Studied By Spin-polarized Electron Energy Loss Spectroscopy”. PhD thesis. Martin-Luther-Universität Halle-Wittenberg, 2005.

[29] P. Ferriani et al. “Atomic-Scale Spin Spiral with a Unique Rotational Sense: Mn Monolayer on W(001)”. In: *Phys. Rev. Lett.* 101 (2 July 2008), p. 027201.

[30] A. Fert and Peter M. Levy. “Role of Anisotropic Exchange Interactions in Determining the Properties of Spin-Glasses”. In: *Phys. Rev. Lett.* 44 (23 June 1980), pp. 1538–1541.

[31] Albert Fert, Nicolas Reyren, and Vincent Cros. “Magnetic skyrmions: advances in physics and potential applications”. In: *Nature Reviews Materials* 2.7 (2017), p. 17031. ISSN: 2058-8437.

[32] H. Fritzsche, J. Kohlhepp, and U. Gradmann. “Epitaxial strain and magnetic anisotropy in ultrathin Co films on W(110)”. In: *Phys. Rev. B* 51 (22 June 1995), pp. 15933–15941.

[33] Vladimir A. Gubanov, Alexandr I. Liechtenstein, and Andrei V. Postnikov. “Exchange Interactions in Metals”. In: *Magnetism and the Electronic Structure of Crystals.* Berlin, Heidelberg: Springer Berlin Heidelberg, 1992, pp. 41–54. ISBN: 978-3-642-84411-9.

[34] Nadine Hauptmann et al. “Revealing the correlation between real-space structure and chiral magnetic order at the atomic scale”. In: *Phys. Rev. B* 97 (10 Mar. 2018), p. 100401.

[35] Stefan Heinze et al. “Spontaneous atomic-scale magnetic skyrmion lattice in two dimensions”. In: *Nature Physics* 7.9 (2011), pp. 713–718. ISSN: 1745-2481.

[36] Frank Herman et al. “Relativistic Corrections to the Band Structure of Tetrahedrally Bonded Semiconductors”. In: *Phys. Rev. Lett.* 11 (12 Dec. 1963), pp. 541–545.

[37] Conyers Herring. “Direct exchange between well-separated atoms”. In: *Magnetism* 2 (1966), pp. 2–189.

[38] Conyers Herring and Charles Kittel. “On the Theory of Spin Waves in Ferromagnetic Media”. In: *Phys. Rev.* 81 (5 Mar. 1951), pp. 869–880.

[39] Marie Hervé et al. “Stabilizing spin spirals and isolated skyrmions at low magnetic field exploiting vanishing magnetic anisotropy”. In: *Nature Communications* 9.1 (2018), p. 1015. ISSN: 2041-1723.

[40] Andrea Hjelt. “Magnons dispersion relation in ultrathin Co films grown on Ir(111)”. PhD thesis. Karlsruhe Institute of Technology, 2019.

[41] Huei-Ying Ho, Jyh-Shen Tsay, and Yu-Shan Chen. “Oxygen Adsorption and Magnetic Properties of Ultrathin Co/Ir(111) Films”. In: *Japanese Journal of Applied Physics* 49.7 (July 2010), p. 075802.

[42] Markus Hoffmann et al. "Antiskyrmions stabilized at interfaces by anisotropic Dzyaloshinskii-Moriya interactions". In: *Nature Communications* 8.1 (2017), p. 308. ISSN: 2041-1723.

[43] H. Hopster, R. Raue, and R. Clauberg. "Spin-Flip Stoner Excitations in a Ferromagnet Observed by Inelastic Spin-Polarized Electron Scattering". In: *Phys. Rev. Lett.* 53 (7 Aug. 1984), pp. 695–697.

[44] Pin-Jui Hsu et al. "Guiding Spin Spirals by Local Uniaxial Strain Relief". In: *Phys. Rev. Lett.* 116 (1 Jan. 2016), p. 017201.

[45] F. Hund. "Symmetriecharaktere von Termen bei Systemen mit gleichen Partikeln in der Quantenmechanik". In: *Zeitschrift für Physik* 43.11 (1927), pp. 788–804. ISSN: 0044-3328.

[46] H. Ibach. *Electron Energy Loss Spectroscopy and Surface Vibrations*. Academic Press Inc., April 1, 1982.

[47] H. Ibach. *Physics of Surfaces and Interfaces*. Springer Berlin Heidelberg New York, 2006.

[48] H. Ibach et al. "A novel spectrometer for spin-polarized electron energy-loss spectroscopy". In: *Review of Scientific Instruments* 74.9 (2003), pp. 4089–4095.

[49] K. Ishikawa and Y. Tobita. "Finite-size corrections to Fermi's golden rule: I. Decay rates". In: *Progress of Theoretical and Experimental Physics* 2013.7 (July 2013), 73B02–0.

[50] S. N. Jasperson and S. E. Schnatterly. "An Improved Method for High Reflectivity Ellipsometry Based on a New Polarization Modulation Technique". In: *Review of Scientific Instruments* 40.6 (1969), pp. 761–767.

[51] C. Jensen, K. Reshöft, and U. Köhler. "Direct observation of strain relaxation in iron layers on W(110) by time-resolved STM". In: *Applied Physics A* 62.3 (1996), pp. 217–221. ISSN: 1432-0630.

[52] Pei-Cheng Jiang et al. "Layered structure and related magnetic properties for annealed Fe/Ir(111) ultrathin films". In: *Journal of Applied Physics* 117.17 (May 2015), 17B742.

[53] J. Kessler. "Electron Spin Polarization by Low-Energy Scattering from Unpolarized Targets". In: *Rev. Mod. Phys.* 41 (1 Jan. 1969), pp. 3–25.

[54] J. Kirschner. "Direct and Exchange Contributions in Inelastic Scattering of Spin-Polarized Electrons from Iron". In: *Phys. Rev. Lett.* 55 (9 Aug. 1985), pp. 973–976.

[55] J. Kirschner. *Polarized Electrons at Surfaces*. Springer-Verlag Berlin Heidelberg, 1985.

[56] J. Kirschner, D. Rebenstorff, and H. Ibach. “High-Resolution Spin-Polarized Electron-Energy-Loss Spectroscopy and the Stoner Excitation Spectrum in Nickel”. In: *Phys. Rev. Lett.* 53 (7 Aug. 1984), pp. 698–701.

[57] Fabian Kloodt-Twesten et al. “Measuring the Dzyaloshinskii-Moriya interaction of the epitaxial Co/Ir(111) interface”. In: *Phys. Rev. B* 100 (10 2019), p. 100402.

[58] A.A. Lucas and M. Šunjić. “Fast-electron spectroscopy of collective excitations in solids”. In: *Progress in Surface Science* 2 (1972), pp. 75–137. ISSN: 0079-6816.

[59] H. L. Meyerheim et al. “Surface structure and stress in Fe monolayers on W(110)”. In: *Phys. Rev. B* 64 (4 July 2001), p. 045414.

[60] H. A. Mook and R. M. Nicklow. “Neutron Scattering Investigation of the Magnetic Excitations in Iron”. In: *Phys. Rev. B* 7 (1 Jan. 1973), pp. 336–342.

[61] T Moriya and Y Takahashi. “Itinerant Electron Magnetism”. In: *Annual Review of Materials Science* 14.1 (1984), pp. 1–25.

[62] Tôru Moriya. “Anisotropic Superexchange Interaction and Weak Ferromagnetism”. In: *Phys. Rev.* 120 (1 Oct. 1960), pp. 91–98.

[63] K. Oura et al. *Surface Science*. Springer-Verlag Berlin Heidelberg, 2003.

[64] W. L. O’Brien and B. P. Tonner. “Magnetic and structural properties of ultrathin Mn and Fe films on Ir(111)”. In: *Journal of Vacuum Science & Technology A* 13.3 (1995), pp. 1544–1548.

[65] M. Pajda et al. “Ab initio calculations of exchange interactions, spin-wave stiffness constants, and Curie temperatures of Fe, Co, and Ni”. In: *Phys. Rev. B* 64 (17 Oct. 2001), p. 174402.

[66] Daniel T. Pierce and Felix Meier. “Photoemission of spin-polarized electrons from GaAs”. In: *Phys. Rev. B* 13 (12 June 1976), pp. 5484–5500.

[67] M. Plihal, D. L. Mills, and J. Kirschner. “Spin Wave Signature in the Spin Polarized Electron Energy Loss Spectrum of Ultrathin Fe Films: Theory and Experiment”. In: *Phys. Rev. Lett.* 82 (12 Mar. 1999), pp. 2579–2582.

[68] M. Plihal et al. “Spin-polarized-electron scattering studies of the Fe bilayer on W(100): Theory and experiment”. In: *Phys. Rev. B* 51 (13 Apr. 1995), pp. 8193–8203.

[69] M. Pratzer, H. J. Elmers, and M. Getzlaff. “Heteroepitaxial growth of Co on W(110) investigated by scanning tunneling microscopy”. In: *Phys. Rev. B* 67 (15 Apr. 2003), p. 153405.

[70] J. Prokop et al. “Magnons in a Ferromagnetic Monolayer”. In: *Phys. Rev. Lett.* 102 (17 Apr. 2009), p. 177206.

[71] M. Przybylski and U. Gradmann. “Ferromagnetic order in a Fe(110) monolayer on W(110) by Mössbauer spectroscopy”. In: *Phys. Rev. Lett.* 59 (10 Sept. 1987), pp. 1152–1155.

[72] X. Qian and W. Hübner. “First-principles calculation of structural and magnetic properties for Fe monolayers and bilayers on W(110)”. In: *Physical Review B* 60.23 (Dec. 1999), pp. 16192–16197.

[73] H. J. Qin et al. “Experimental Realization of Atomic-Scale Magnonic Crystals”. In: *Phys. Rev. Lett.* 123 (25 Dec. 2019), p. 257202.

[74] H. J. Qin et al. “Temperature Dependence of Magnetic Excitations: Terahertz Magnons above the Curie Temperature”. In: *Phys. Rev. Lett.* 118 (12 Mar. 2017), p. 127203.

[75] R.Feder, ed. *Polarized Electrons in Surface Physics*. World Scientific, 1985.

[76] J. Kirschner R.Feder. “Spin-Polarized Low-Energy Electron Diffraction: Theory, Experiment and Analysis of Results from W(001)(1x1)”. In: *Surface Science* (1981).

[77] Olga Yu. Ridzel, Vytautas Astašauskas, and Wolfgang S.M. Werner. “Low energy (1–100 eV) electron inelastic mean free path (IMFP) values determined from analysis of secondary electron yields (SEY) in the incident energy range of 0.1–10 keV”. In: *Journal of Electron Spectroscopy and Related Phenomena* 241 (2020). Sources, Interaction with Matter, Detection and Analysis of Low Energy Electrons (SIMDALEE2), p. 146824. ISSN: 0368-2048.

[78] C. C. Robinson. “Longitudinal Kerr Magneto-Optic Effect in Thin Films of Iron, Nickel, and Permalloy”. In: *J. Opt. Soc. Am.* 53.6 (June 1963), pp. 681–689.

[79] D Sander. “The magnetic anisotropy and spin reorientation of nanostructures and nanoscale films”. In: *Journal of Physics: Condensed Matter* 16.20 (May 2004), R603–R636.

[80] D Sander, A Enders, and J Kirschner. “Anisotropic surface stress on W(110)”. In: *Europhysics Letters (EPL)* 45.2 (Jan. 1999), pp. 208–214.

[81] D. Sander et al. “Film Stress and Domain Wall Pinning in Sesquilayer Iron Films on W(110)”. In: *Phys. Rev. Lett.* 77 (12 Sept. 1996), pp. 2566–2569.

[82] Katsuaki Sato. “Measurement of Magneto-Optical Kerr Effect Using Piezo-Birefringent Modulator”. In: *Japanese Journal of Applied Physics* 20.12 (Dec. 1981), pp. 2403–2409.

[83] R. E. Schlier. “Adsorption of Oxygen and Carbon Monoxide on Tungsten”. In: *Journal of Applied Physics* 29.8 (1958), pp. 1162–1167.

[84] J. Schoenes. *Materials Science and Technology, Vol. 3A: Electronic and Magnetic Properties of Metals and Ceramics*. Ed. by K. H. J. Buschow. Wiley-VCH, 1992.

[85] A. Schreyer et al. “Neutron scattering on magnetic thin films: Pushing the limits (invited)”. In: *Journal of Applied Physics* 87.9 (2000), pp. 5443–5448.

[86] E. Simon et al. “Formation of magnetic skyrmions with tunable properties in PdFe bilayer deposited on Ir(111)”. In: *Phys. Rev. B* 90 (9 2014), p. 094410.

[87] J. C. Slater. “The Theory of Ferromagnetism: Lowest Energy Levels”. In: *Phys. Rev.* 52 (3 Aug. 1937), pp. 198–214.

[88] Edmund Clifton Stoner. “Collective electron ferronmagnetism”. In: *Proceedings of the Royal Society of London. Series A. Mathematical and Physical Sciences* 165.922 (1938), pp. 372–414.

[89] Edmund Clifton Stoner and Richard Whiddington. “Collective electron specific heat and spin paramagnetism in metals”. In: *Proceedings of the Royal Society of London. Series A - Mathematical and Physical Sciences* 154.883 (1936), pp. 656–678.

[90] J. C. Suits. “Magneto-Optical Rotation and Ellipticity Measurements with a Spinning Analyzer”. In: *Review of Scientific Instruments* 42.1 (1971), pp. 19–22.

[91] John T. Yates, Theodore E. Madey, and Nils E. Erickson. “ESCA study of carbon monoxide and oxygen adsorption on tungsten”. In: *Surface Science* 43.1 (1974), pp. 257–274. ISSN: 0039-6028.

[92] W. X. Tang et al. “Large Wave Vector Spin Waves and Dispersion in Two Monolayer Fe on $W(110)$”. In: *Phys. Rev. Lett.* 99 (8 Aug. 2007), p. 087202.

[93] S. Tsurkan and Kh. Zakeri. “Giant Dzyaloshinskii-Moriya interaction in epitaxial Co/Fe bilayers with C_{2v} symmetry”. In: *Phys. Rev. B* 102 (6 Aug. 2020), p. 060406.

[94] L. Udvardi and L. Szunyogh. “Chiral Asymmetry of the Spin-Wave Spectra in Ultrathin Magnetic Films”. In: *Phys. Rev. Lett.* 102 (20 May 2009), p. 207204.

[95] D. Venus, S. Cool, and M. Plihal. “Quantitative structural determination using spin-polarized low-energy electron diffraction rotation curves: W(110)”. In: *Surface Science* 446.3 (2000), pp. 199–210. ISSN: 0039-6028.

[96] D. Venus and J. Kirschner. “Momentum dependence of the Stoner excitation spectrum of iron using spin-polarized electron-energy-loss spectroscopy”. In: *Phys. Rev. B* 37 (4 Feb. 1988), pp. 2199–2211.

[97] Gy. J. Vida et al. “Domain-wall profiles in $\mathrm{Co/Ir}_n/\mathrm{Pt}(111)$ ultrathin films: Influence of the Dzyaloshinskii-Moriya interaction”. In: *Phys. Rev. B* 94 (21 2016), p. 214422.

[98] K. Wagner et al. “Magnetization of free Fe(110) surfaces from thin film magnetometry”. In: *Journal of Magnetism and Magnetic Materials* 167.1 (1997), pp. 21–26. ISSN: 0304-8853.

[99] Lynn White. "Clerks and Craftsmen in China and the West. Lectures and Addresses on the History of Science and Technology. Joseph Needham. Based largely on collaborative work with Wang Ling, Lu Gwei-Djen, and Ho Ping-Yü. Cambridge University Press, New York, 1970." In: *Science* 168.3932 (1970), pp. 728–728. ISSN: 0036-8075.

[100] W. Wulfhekel et al. "Growth and magnetism of Fe nanostructures on W(001)". In: *Physical Review B* 68.14 (2003), pp. 1444161–9. ISSN: 1098-0121.

[101] W. Wulfhekel et al. "Relation between structure, stress, and magnetism in Co/W(001)". In: *Physical Review B - Condensed Matter and Materials Physics* 64.14 (2001), Art.Nr. 144422. ISSN: 1098-0121.

[102] W. Wulfhekel et al. "The relation between Structure, Stress and Magnetism in Co/W(001)". In: *Physical Review B* 64.14 (2001), pp. 1444221–8. ISSN: 0163-1829.

[103] A. Yamasaki et al. "Spin-polarized scanning tunneling spectroscopy study of Fe nanomagnets on W(001)". In: *Journal of Applied Physics* 95.11 (2004), pp. 7025–7027. ISSN: 0021-8979.

[104] Kh. Zakeri et al. "Asymmetric Spin-Wave Dispersion on Fe(110): Direct Evidence of the Dzyaloshinskii-Moriya Interaction". In: *Phys. Rev. Lett.* 104 (13 Mar. 2010), p. 137203.

[105] Kh. Zakeri et al. "Direct probing of the exchange interaction at buried interfaces". In: *Nature Nanotechnology* 8.11 (Sept. 2013), pp. 853–858.

[106] Kh Zakeri et al. "Magnon excitations in ultrathin Fe layers: The influence of the Dzyaloshinskii-Moriya interaction". In: *Journal of Physics: Conference Series* 303 (July 2011), p. 012004.

[107] Kh. Zakeri et al. "Magnon Lifetimes on the Fe(110) Surface: The Role of Spin-Orbit Coupling". In: *Phys. Rev. Lett.* 108 (19 May 2012), p. 197205.

[108] Kh. Zakeri et al. "On the preparation of clean tungsten single crystals". In: *Surface Science* 604.2 (2010), pp. L1 –L3. ISSN: 0039-6028.

[109] Khalil Zakeri. "Elementary spin excitations in ultrathin itinerant magnets". In: *Physics Reports* 545.2 (2014). Elementary spin excitations in ultrathin itinerant magnets, pp. 47–93. ISSN: 0370-1573.

[110] Khalil Zakeri. "Probing of the interfacial Heisenberg and Dzyaloshinskii–Moriya exchange interaction by magnon spectroscopy". In: *Journal of Physics: Condensed Matter* 29.1 (Nov. 2016), p. 013001.

[111] Y. Zhang et al. "Nonmonotonic thickness dependence of spin wave energy in ultrathin Fe films: Experiment and theory". In: *Phys. Rev. B* 81 (9 2010), p. 094438.

[112] Yu Zhang. "High wave vector spin waves in ultrathin Fe films on W(110) studied by spin-polarized electron energy loss spectroscopy". PhD thesis. Martin-Luther-Universität Halle-Wittenberg, 2008.

8. Acknowledgments

I would like to thank all of the people who have helped my throughout this Ph.D. and without whom this would not have been possible.

I thank my doctorate supervisor PD. Dr. Khalil Zakeri for giving me an opportunity to work in his Heisenberg spin dynamics group and to be a part of this incredible research. The amount of new things I have learned even besides SPEELS and how much I've grown as a scientist under his supervision is incredible. His constants guidance and patience is greatly appreciated. His care as a person and not only a supervisor went along way during this doctoral study.

I thank Prof. Dr. Wulfhekel for being the second reviewer of this thesis. He always showed interest in my work and provided a great environment in his group that I could also engage in.

I thank Prof. Dr. Arthur Ernst at Linz University, who graciously provided the code for alot of the calculations in this thesis. This was indispensible for data analysis and interpretation.

I would like to thank the current and former members of the SPEELS group that made my journey here an incredible experience. Dominik Rau helped me around the SPEELS lab when I just got here. Tobias Schreckenberger provided many good conversations and I had a great time performing measurements with him. Through Janek's Wettsteins project , I got the chance to be exposed to thin film superconductor SPEELS measurements. The good atmosphere in the lab that we had went along way. Time in the lab with Andrea Hjelt was by far the most musical one, there was never a day when we didn't sing. I learned so much from Sakineh Abdizadeh, we had many great discussions about the theory of magnetism. It was alot of fun and a great honor to work with all of my colleagues. I have made life long friends.

I want to thank the member of Prof. Dr. Wulfhekels group for providing a great environment and friendship at the Physikalisches Institut. Timo Fraunhammer and Thomas Gozlinski were a constant source of sports knowledge and I could always talk to them about this. Loïc Mougel is a great friend and I could always rely on that. To the other many members of the group, a sincere thank you for your friendship.

I would like to thank the employees at the electronic and mechanical workshop. In particular a big thanks to Roland Jehle, Jannis Ret, Michael Meyer for the many issues that they helped me fix and that made this dissertation go as smooth as possible.

I want to thank my family both in the Unites States and here in Germany for supporting me constantly throughout this journey. They had always believed in me and I appreciate that immensely.

I want to thank my friends in the United States Den, AK, Pashak, Stan whos contact with me reminded me always of their brotherhood and kept me updated with the current events there.

I would like to thank the Deutsche Forschungsgemeinschaft (DFG) that supported this work through the Heisenberg Programme No. ZA 902/3-1 and No. ZA 902/6-1 and the DFG Grant No. ZA 902/4-1. A big thanks goes out to the Physikalisches Institut for hosting the SPEELS laboratory and the group along with providing the necessary infrastructure.

I want to thank my wife Kate for being the unshakable pillar during this Ph.D. and always encouraging me to keep going. She was patient when the days were long and always understood the sacrifice needed. Her love and a bright unique spirit always kept my head up. Thank you. I want to also thank my daughter Grace who is too young to read this but she has been an incredible source of happiness during the difficult times.